Investigation of the SAGD Steam Trap with a Simple Modelling Approach

by

Spencer Taubner

A thesis submitted in partial fulfillment of the requirements for the degree of

Master of Science

Department of Mechanical Engineering
University of Alberta

Abstract

Steam-assisted gravity drainage (SAGD) has become the most popular in situ method for recovering bitumen in Alberta, but it remains an operationally challenging process. A particular challenge is the maintenance of a liquid pool, or steam trap, around the production well to prevent the influx of live steam, which reduces energy efficiency and increases the risk of eroding production equipment. In this thesis, an analytical model called a gravity inflow performance relationship (GIPR) is formulated to describe the flow through the steam trap. The model enables efficient prediction of the liquid level above the production well, providing a valuable tool for optimizing SAGD well designs and control strategies. The GIPR is verified against simulations using a higher-order numerical model. Then, the GIPR is coupled to a wellbore hydraulics model to study the uniformity and stability of the liquid-vapour interface along the length of a SAGD well pair. Three case studies are conducted with the coupled model, each investigating a different operational challenge, and each providing fundamental insight into the mechanics of steam trap control.

Acknowledgments

First and foremost, I would like to thank my partner, Kelin Flanagan, for her unwavering support and (nearly) limitless patience, and for providing much needed distractions from this project. I would also like to thank my parents, Barb and Ric, for supporting me through my undergraduate degree, and for continuing to encourage me through graduate school.

I would like to thank Dr. Michael Lipsett, my supervisor, for sharing his knowledge of many engineering subjects, and for always offering a fresh perspective. I am also indebted to Dr. Trent Kaiser for his innumerable contributions to this project, and for his mentorship over the past five years.

I would like to acknowledge John Graham, Alan Keller, and Chris Bailey of the Firebag Resource Team at Suncor Energy Inc. for lending their immense and invaluable field experience to this project. I would additionally like to acknowledge Computer Modelling Group Ltd. for providing the STARS reservoir simulator. Finally, I would like to acknowledge Noetic Engineering 2008 Inc. for enabling me to pursue my graduate degree.

Contents

List of Tables

List of Figures

List of Symbols

English Letters

A	Flow Area [m^2]
c	Specific Heat Capacity [J/(kg·°C)]
C	Correction Factor
f_w	Water Cut
g	Acceleration Due to Gravity [m/s^2]
h	Liquid Level [m]
H	Steam Chamber Height [m]
I'	Well Index [m^3]
j	Leverett j-Function
k	Permeability [m^2]
k_r	Relative Permeability
l	Grid Block Thickness [m]
L	Flow Length [m]
P	Pressure [Pa]
q	Specific Volumetric Flow Rate [$m^3/s/m$]
Q	Volumetric Flow Rate [m^3/s]
q'''	Heat Generation per Unit Volume [W/m^3]
r	Radial Coordinate [m]

r^*	Transformed Radial Coordinate [m]
R	Radius [m]
Re	Reynolds Number
s	Skin Factor
S	Saturation
t	Time [s]
T	Temperature [°C]
u	Flow Velocity [m/s]
x	Horizontal Coordinate [m]
x^*	Transformed Horizontal Coordinate [m]
z	Vertical Coordinate [m]
z^*	Transformed Vertical Coordinate [m]

Greek Letters

α	Thermal Diffusivity [m^2/s]
γ	Interfacial Tension [N/m]
θ	Angular Coordinate [rad]
κ	Thermal Conductivity [W/(m·°C)]
λ_r	Relative Mobility [$(Pa{\cdot}s)^{-1}$]
μ	Dynamic Viscosity [Pa·s]
ν	Kinematic Viscosity [m^2/s]
ρ	Density [kg/m^3]
ϕ	Porosity
Φ	Fluid Potential [J/kg]
Ω	Flow Resistance [$Pa/(m^3/s)$]

Subscripts

a	Apparent
c	Capillary
e	Effective
f	Fluid
g	Gas
m	Mixture
o	Oil
p	Production Well
r	Reservoir
s	Sand
sc	Steam Chamber
v	Vertical
w	Water
wf	Wellbore Flowing
h	Horizontal

Chapter 1

Introduction

The Alberta Energy Regulator (AER) estimates that there are 1.8 trillion barrels of bitumen beneath the province of Alberta, Canada, of which about 170 billion barrels are recoverable (AER 2015). Some of the bitumen is close enough to the surface to be mined. Most of the bitumen is too deep for mining, however, and must be recovered *in situ* by drilling wells.

Bitumen is extremely viscous at ambient temperatures, which renders in situ recovery challenging. Numerous recovery methods have been trialed, most involving heating the bitumen to reduce its viscosity, but steam-assisted gravity drainage (SAGD) has emerged as the most successful. In 2014, SAGD accounted for 58% of Alberta's bitumen production by in situ methods and 32% of the province's total bitumen production (AER 2015).

This thesis is concerned with the mathematical modelling of SAGD. The SAGD process is reviewed in Section 1.1, and the objective of the present work is described in Section 1.2. Section 1.3 presents an outline of the chapters that follow.

1.1 Background

1.1.1 Steam-Assisted Gravity Drainage

The SAGD process is illustrated in Figure 1.1. Using a long, horizontal well, steam is injected into a bitumen reservoir, where it tends to rise due to buoyancy. When the steam comes into contact with the cool bitumen in the reservoir, it condenses and transfers much of its latent energy (the energy released when the steam changes from a vapour to a liquid) to the bitumen. The resulting rise in the temperature of the bitumen reduces its viscosity and permits it to drain, by gravity, to a second horizontal well. The heated bitumen then flows through the second well to the surface.

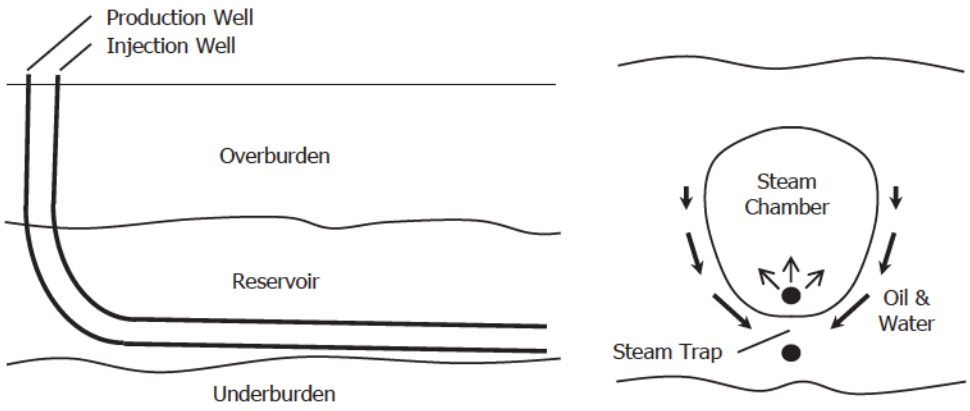

Figure 1.1: SAGD well configuration (left) and process (right)

SAGD was conceived by Roger Butler and his colleagues at Esso Resources Canada Limited (Butler et al. 1981) as an economical method to recover Alberta's exceptionally viscous bitumen. Conventional steam flooding processes, which rely on steam to push oil towards production wells, can be ineffective in such applications because the steam tends to travel as narrow fingers, leaving much of the oil behind. SAGD circumvents this phenomenon by positioning both the injection and production wells at the bottom of the reservoir and relying on the natural tendencies for steam

to rise and for liquids to fall. As its name suggests, SAGD is driven by gravity; oil is not "pushed" to the production well as in conventional steam flooding processes.

1.1.2 Steam Trap Control

As bitumen is gradually removed from the reservoir, a *steam chamber* develops in its place. If the growing steam chamber is permitted to engulf the production well, then steam has the tendency to flow directly from the injection well to the production well, bypassing much of the reservoir. This "short circuit" is called *steam breakthrough* and decreases the efficiency of SAGD, since a portion of the steam injected simply flows back to the surface. Steam breakthrough may also lead to the erosion of production equipment by sand entrained in high-velocity steam (Das 2005).

To prevent steam breakthrough, SAGD operators employ a control strategy called *steam trap control*, whereby the flow rate from the production well is regulated so that the liquid draining down the steam chamber walls pools around the production well, providing a barrier to the flow of steam (Shen 2013, 431-432). This control strategy is also called *subcool control* (Yuan and Nugent 2013) because the production well is maintained at subcooled conditions (i.e., at a temperature below the boiling temperature of water). Butler (1997) explains the original inspiration for steam trap control:

> It was thought that if [oil and condensate] were not removed too quickly, then the tendency of the steam to flow directly to the production well – and thus to bypass the reservoir – could be reduced or possibly even eliminated. This is analogous to the ability of a steam trap to allow the flow of condensate from the bottom of a steam-heated radiator without allowing significant bypassing of the steam. (286)

Although steam trap control is conceptually simple, the liquid level in the steam trap cannot be measured directly. Operators must rely on temperature and pressure

measurements to infer the position of the liquid-vapour interface. Further, if too much liquid is permitted to accumulate around the production well, then the size of the steam chamber is reduced and production suffers.

1.2 Objective

The objective of the present work is to formulate, verify, and apply an analytical model of the flow through the SAGD steam trap. The primary purpose of the model is to enable efficient prediction of the liquid level above the production well, thereby permitting SAGD operators to optimize well designs and operational strategies to facilitate steam trap control. The analytical model will hereafter be referred to as a *gravity inflow performance relationship* (gravity IPR or GIPR) for its mathematical similarity to IPRs for conventional oil and gas wells.

This work builds upon the analysis methodology described by Kaiser and Taubner (2013). An early, numerical model of the steam trap has proven valuable for analyzing SAGD well pairs (see Smith et al. 2014); however, it is inefficient and has not been verified against a higher-order model, giving rise to the current work.

1.3 Overview

1.3.1 Literature Review

Chapter 2 describes existing analytical models of SAGD and reviews the literature relevant to steam trap control. The limitations of the previous research are identified, providing motivation for the current work.

1.3.2 Model Formulation

Chapter 3 formulates an analytical GIPR for SAGD production wells. The model is first formulated for reservoirs with isotropic permeability; then, the model is extended to anisotropic reservoirs.

1.3.3 Model Verification Against Simulations Using Higher-Order Numerical Model

Chapter 4 verifies the GIPR against simulations using a higher-order numerical model. A correction factor is introduced in the GIPR to improve agreement with the higher-order model.

1.3.4 Case Studies

Chapter 5 presents the findings of case studies conducted by coupling the GIPR to a wellbore hydraulics model. The case studies examine three challenges to steam trap control: (1) variable pay thickness, (2) non-uniform reservoir permeability, and (3) an inclined production well.

1.3.5 Conclusions and Recommendations

Chapter 6 summarizes the conclusions of the current work and provides recommendations for future work.

Chapter 2

Literature Review

This chapter describes existing analytical models of SAGD and reviews the literature relevant to steam trap control. The analytical models are divided into two categories: models describing gravity drainage ahead of the steam chamber, and models describing the flow through the steam trap. Various aspects of steam trap control are discussed, including the optimum subcool for the production well, the relationship between the subcool and the liquid level, wellbore hydraulics, and plugging and scaling. Recent research on flow control devices (FCDs) is also reviewed.

2.1 Analytical Models of SAGD

2.1.1 Gravity Drainage

The first analytical model of the SAGD process was developed by Butler et al. (1981). By considering the heat transfer ahead of the steam chamber by conduction, the temperature dependence of the oil viscosity, and Darcy's law for gravity drainage,

they derived the following equation for the drainage rate of oil:

$$q_o = 2\sqrt{\frac{2kg\alpha\phi\Delta S_o H}{m\nu_{sc}}} \tag{2.1}$$

where k is the reservoir permeability, g is the acceleration due to gravity, α is the reservoir thermal diffusivity, ϕ is the reservoir porosity, ΔS_o is the difference between the initial and residual oil saturations, H is the steam chamber height, ν_{sc} is the kinematic oil viscosity at the steam chamber temperature, and m is a parameter that describes the change in the oil viscosity with temperature.

The original model has proven to be remarkably accurate given its various simplifications. However, it predicts that the walls of the steam chamber retreat from the production well as drainage progresses – a nonphysical prediction, since there would be no potential difference to drive liquid horizontally to the production well. Therefore, Butler and Stephens (1981) refined the model by assuming that the steam chamber walls are anchored at the production well. The constant under the square root sign in the resulting drainage rate equation is 1.5 instead of 2, and so the refined drainage rate is 87% of the original.

Numerous other models of the SAGD process have been developed over the past few decades, most of which are variations on the original model or its early refinements. Reis (1992) introduced an empirical constant in the drainage rate equation to improve agreement with the experimental data of Chung and Butler (1988). More recently, Azad and Chalaturnyk (2012) devised a model based on a circular steam chamber geometry, which describes both the vertical steam chamber growth early in the life of a well pair and the subsequent lateral growth. Other models have been developed to capture such complexities as

- varying steaming rates, pressures, and durations (Ferguson and Butler 1988);

- the asphaltene content dependence of the oil viscosity (Akin 2005);
- relative permeability effects (Sharma and Gates 2010); and
- geomechanics (Azad and Chalaturnyk 2010; Cokar et al. 2013).

Analytical models are capable of demonstrating good agreement with field data (Azad and Chalaturnyk 2013) and, despite continuous advancements in numerical simulation technology, remain efficient and valuable engineering tools. A common feature of the above-listed models, however, is that they describe only the gravity drainage of liquid ahead of the steam chamber; they do not describe the flow through the steam trap.

2.1.2 Steam Trap

Only two analytical models of the flow through the steam trap have been found in the literature. The earlier of the two models was developed by Ong and Butler (1990), who recognized that the fluid interface is not anchored to the production well, as is assumed in most drainage models, but lies a short distance above the well. They model the flow from the fluid interface to the production well using the equation for steady flow from a line source:

$$q_o = \frac{4\pi k}{\mu_o \ln\left(2h/R_p\right)}(P_{sc} + \rho g h - P_p) \tag{2.2}$$

where q_o is the specific inflow rate of oil, h is the liquid level, R_p is the radius of the production well, P_{sc} is the steam chamber pressure, P_p is the production well pressure, and ρ is the fluid density.

Ong and Butler (1990) argue that modelling the fluid interface as a straight, horizontal line introduces little error because most of the potential loss occurs in the

near-wellbore region. The oil viscosity, μ_o, is assumed to be constant and evaluated at a mixing temperature, which is function of the steam chamber temperature and the far-field reservoir temperature.

The second analytical model of the flow through the steam trap was developed by Yuan and Nugent (2013). They model the flow from the fluid interface to the production well using the equation for steady, radial flow through a porous "wedge" of angle Θ. They assume that the emulsion viscosity, μ, increases linearly from the fluid interface to the production well, yielding the following relationship:

$$\Delta P + \rho g h = \frac{q}{\Theta k}\left[\frac{\mu(T_p)h - \mu(T_{sc})R_p}{h - R_p}\ln\frac{h}{R_p} + \mu(T_{sc}) - \mu(T_p)\right] \tag{2.3}$$

where ΔP is the pressure difference between the steam chamber and the production well, q is the specific inflow rate of emulsion, T_{sc} is the steam chamber temperature, and T_p is the inflow temperature.

The model uses "power-law mixing according to saturations to estimate the emulsion viscosity" (363) but few details of this calculation are provided. Yuan and Nugent (2013) calibrated Equation 2.3 against numerical reservoir simulations to obtain an average value for Θ of 0.4306. The authors argue that "because the fluids flow into the production well mostly by gravity... it is likely that the value of Θ will be approximately or less than 0.5" (363). It is unclear, however, if Θ is intended to represent the angle (in radians) of the porous wedge, as suggested by Equation 2.3, or if Θ is intended to represent the fraction of the well circumference through which there is inflow, as suggested by the accompanying discussion. A value for Θ of 0.5 radians gives a porous wedge of just 29° – not 180°, as might be expected if the flow is primarily through the top half of the production well.

Few other analytical studies of the steam trap have been found in the literature.

Gotawala and Gates (2012) developed a control equation for SAGD well pairs based on material and energy balances in the steam trap. Some researchers have based inflow models for SAGD production wells on those for conventional horizontal wells (Gonzalez et al. 2012) or a productivity index (Duncan et al. 2014, 2015), but few details of these approaches are provided.

2.2 Steam Trap Control

2.2.1 Optimum Subcool for Production Well

It is widely accepted that the production well should be maintained at subcooled conditions. Compared to an operating policy that permits significant steam production, steam trap control is thought to reduce the risk of erosion of production equipment, improve energy efficiency, and prevent bottlenecks from high vapour flow rates (Das 2005).

Numerical reservoir simulations in two dimensions indicate that the *production well subcool*, the margin by which the temperature in the production well is lower than the local steam saturation temperature, has an optimum value based on cumulative oil production and steam-to-oil ratio (SOR). The optimum subcool likely varies between reservoirs, but has been found to range from 20 °C to 40 °C (Ito and Suzuki 1999; Edmunds 2000; Tan et al. 2002). Slugging, whereby the production rate rises and falls in a repeating fashion, has been observed in numerical simulations at higher-than-optimum subcools (Edmunds 2000; Das 2005).

There is some evidence to suggest that moderate steam production may be tolerable or even favourable in certain circumstances. Singhal et al. (1998) advise relaxing steam trap constraints in the early life of a well pair to accelerate production.

Numerical simulations conducted by Kisman (2003) indicate that performance is maximized by operating at very low subcools; however, this result is inconsistent with the findings of Ito and Suzuki (1999) and Edmunds (2000).

2.2.2 Relationship Between Subcool and Liquid Level

There is a rule of thumb (a rough estimate based on industry experience rather than analysis) that the subcool in the production well increases by about 10 °C for every metre of liquid above the well (Yuan and Nugent 2013), but the origin of this estimate is unclear. Numerical reservoir simulations indicate a positive correlation between the subcool and the liquid level (i.e., the liquid level rises as the subcool is increased), but the slope of the correlation is not always consistent with the rule of thumb (Edmunds 2000; Das 2005; Gates and Leskiw 2010).

Numerical simulations also suggest that steam may be drawn near or into the production well even when the well is at subcooled conditions. Ito and Suzuki (1999) have observed this behaviour when the specified subcool in the production well is lower than the average subcool of the liquid draining down the steam chamber walls, such that the draining liquid must be heated by steam flow. Gates and Leskiw (2010) have observed steam coning into the production well when the subcool drops below a critical value (about 20 °C). Steam coning occurs because the viscous forces in the steam trap overwhelm buoyancy effects, destabilizing the liquid-vapour interface.

2.2.3 Steam Trap Control in Three Dimensions

Three-dimensional reservoir simulations have revealed that steam trap control is considerably more complex than two-dimensional simulations would suggest. Variations in the conditions along the length of a well pair, such as the temperature

during steam circulation (start-up) or the reservoir properties, may give rise to large variations in the local subcool and liquid level (Edmunds 2000; Gates and Leskiw 2010).

2.2.4 Wellbore Hydraulics

The friction loss (the loss of fluid potential due to friction) along SAGD wells can be significant because of the length of the wells and the flow rates afforded by high-permeability reservoirs. Many believe that there is little steam flow through the reservoir in the direction parallel to the well axes, and thus that the pressure in the steam chamber reflects the pressure gradient along the injection well (Edmunds and Gittins 1993; Edmunds 2000). This belief has given rise to the rule of thumb that the pressure variation along the injection well should be no more than about 50 kPa[1] to limit the liquid level variation to 5 m, the typical spacing between the injection and production wells (Edmunds and Gittins 1993; McCormack 2002).

The effect of pressure variation along the injection well has been investigated in three-dimensional reservoir simulations incorporating wellbore hydraulics models (Edmunds and Gittins 1993; Vander Valk and Yang 2007). Excessive pressure variation may result in the accumulation of liquid and poor steam chamber development along some parts of the well pair, and low liquid levels along others. The pressure variation along the production well has also been shown to affect the fluid interface position (Ong and Butler 1990; Vander Valk and Yang 2007), but the pressure gradient is typically thought to be higher along the injection well because of the low density of steam and high flow velocity. Parappilly and Zhao (2009) have demonstrated that friction loss along the injection and production wells can be an

[1]The pressure differences of greatest interest (e.g., between the steam chamber and the production well) are typically tens or hundreds of kilopascals, and so pressure is expressed in kilopascals throughout this thesis.

obstacle to extending the length of SAGD well pairs.

Thorne and Zhao (2009) conducted numerical simulations of SAGD in a MacKay River reservoir. In cases with pressure variation along the injection well, they observed that steam was injected non-uniformly into the reservoir, but saw little penalty to the cumulative oil production or steam-to-oil ratio. They conclude that "after the steam chamber is established, steam can flow easily in the lateral direction reducing the impact of non-uniform steam distribution" (44-45). This conclusion is contrary to the statements of Edmunds and Gittins (1993), who maintain that "it is not possible for a pressure gradient caused by friction in the injection liner to be significantly reduced by compensating horizontal flow in the steam chamber" (52).

2.2.5 Plugging and Scaling

Pressure differences in excess of 1000 kPa have been observed between the injection and production wells in some SAGD field applications. High interwell pressure differences have been attributed to plugging or scaling of the production liner or near-wellbore reservoir (Bennion et al. 2009; Brand 2010; Cheung and Scheck 2013). Numerical reservoir simulations have shown that a high interwell pressure difference may cause liquid to accumulate excessively around the production well, reducing the size of the steam chamber and impeding production (Zhao et al. 2007; Thorne and Zhao 2009).

2.2.6 Flow Control Devices

Currently, the most active research area related to steam trap control is the testing and development of flow control devices (FCDs) for SAGD wells. FCDs are installed in either the injection or production well to direct the flow of steam or production

fluid in a manner that improves steam trap conformance. Some FCDs are passive and require no operator input, relying on their geometry – an orifice, a helix, or a more elaborate geometry with carefully designed, flow-dependent characteristics – to control flow (Banerjee et al. 2013). Others are valves that may be opened or closed from the surface (Bedry and Shaw 2012; Stahl et al. 2014).

Physical test programs have been conducted to study the flow of steam and liquids through FCDs (Least et al. 2014; Vachon et al. 2015). FCDs have also been modelled in numerical reservoir simulations to quantify their benefit to the SAGD process. The simulations conducted to date have almost universally shown that FCDs can improve performance relative to conventional completion designs, based on steam trap conformance, steam chamber development, oil production, and/or steam-to-oil ratio (Becerra et al. 2014; Ghesmat and Zhao 2014; Kyanpour and Chen 2014; Noroozi et al. 2014; Riel et al. 2014; Shad and Yazdi 2014; Somiari et al. 2014). The performance improvement depends on the properties of the reservoir, along with the FCD type and location (injector or producer).

Field trials of FCDs are underway, but empirical data is currently sparse. Bedry and Shaw (2012) report that the recompletion of an injection well at the Orion project with FCDs has yielded a 45% improvement in SOR and 70% increase in production. Stalder (2013) reports that the performance of a Surmont well pair with FCDs in the injection and production liners has exceeded that of neighbouring well pairs with conventional completion designs. More recently, Becerra et al. (2014) and Stahl et al. (2014) have described field trials that are in their early stages.

2.3 Summary of Previous Work

Numerous analytical models have been developed to describe the gravity drainage of oil ahead of the SAGD steam chamber. By contrast, only two analytical models of the flow through the steam trap have been found in the literature (Ong and Butler 1990; Yuan and Nugent 2013), and only one of these has been verified against a higher-order model (Yuan and Nugent 2013). It is thus believed that there remains great potential to study the steam trap with analytical tools.

Steam trap control has been investigated extensively through numerical simulation, and, with the advent of flow control devices, it remains an active research area. The work conducted to date has revealed that reservoir heterogeneity, wellbore hydraulics, and plugging/scaling render steam trap control extremely challenging. The continued development of analytical models capturing these and other complexities will provide efficient and valuable proxies for computationally intensive numerical simulators.

Chapter 3

Model Formulation

This chapter presents the formulation of a gravity inflow performance relationship (GIPR) for SAGD production wells. The assumptions of the model are identified and discussed. A GIPR is formulated for homogeneous isotropic reservoirs, in which the horizontal and vertical permeabilities are equal. The formulation is extended to homogeneous anisotropic reservoirs, in which the horizontal and vertical permeabilities differ. Intricacies of the model, including the determination of relative permeabilities, are discussed.

3.1 Assumptions

3.1.1 Well-Defined Fluid Interface

It is difficult to obtain high-resolution pressure and temperature measurements in the reservoir around a SAGD well pair. As a result, the exact nature of the interface between the steam chamber and the steam trap is uncertain. Instead of a sharp transition between the vapour and liquid phases, there may exist a zone over which the gas saturation, the volume fraction of the pore space occupied by vapour, decreases

to zero. This zone is probably host to a variety of dynamic processes, such as boiling, condensation, and the cocurrent and countercurrent flow of emulsion and gases (Yuan and Nugent 2013).

The GIPR is based on the simplifying assumption that the zone between the steam chamber and the steam trap can be represented by a well-defined interface, as shown in Figure 3.1. Below the interface, the vapour saturation, S_g, is assumed to be zero and the flow is assumed to be two-phase (oil and liquid water). Only homogeneous reservoirs are considered, and so the fluid interface is taken to be symmetric about a vertical line centred at the production well.

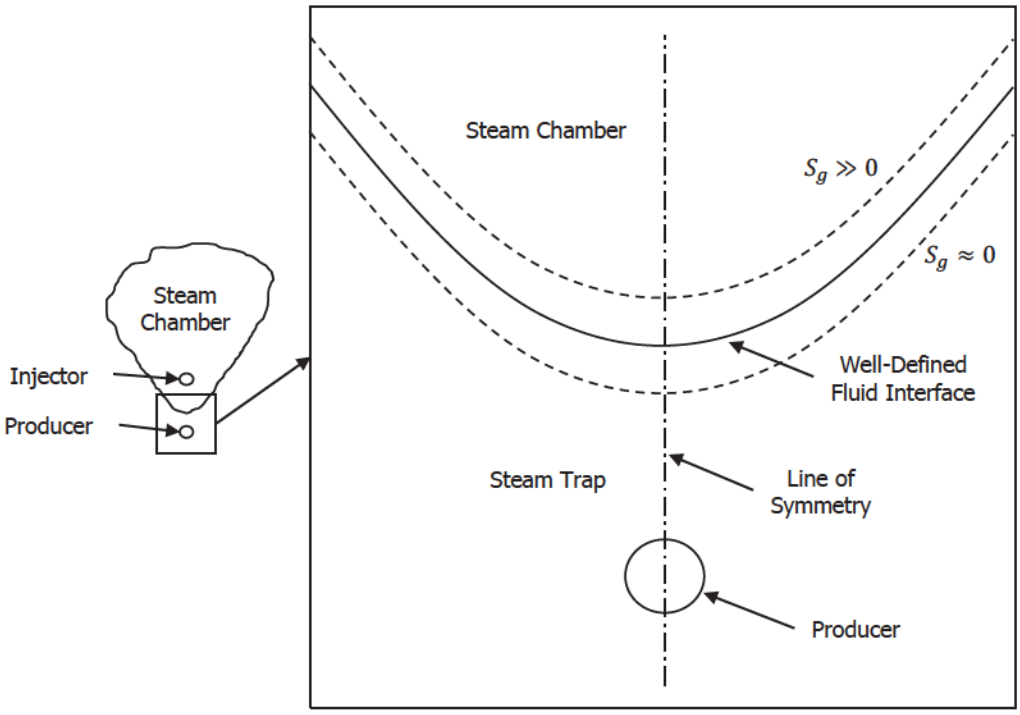

Figure 3.1: Well-defined fluid interface

3.1.2 Two-Dimensional Flow

The horizontal length of a SAGD well pair is many times greater than the thickness of the reservoir. It is common to neglect end effects and analyze SAGD well pairs as if they were infinitely long, which reduces the analysis from three dimensions to two. Butler and his colleagues took this approach when they derived the first equation for the drainage rate from the steam chamber (Butler et al. 1981).

The GIPR assumes that the flow in the steam trap is likewise two-dimensional. Only a cross-section of a SAGD well pair (perpendicular to the well axes) is considered. For isotropic reservoirs, in which the horizontal and vertical permeabilities are equal, the flow to the production well is assumed to be radial, as shown in Figure 3.2. The corresponding equipotentials (lines of constant potential) are circular. For anisotropic reservoirs, in which the horizontal and vertical permeabilities differ, the equipotentials in the steam trap are assumed to be elliptical. In both cases, the model boundary is defined by the liquid level.

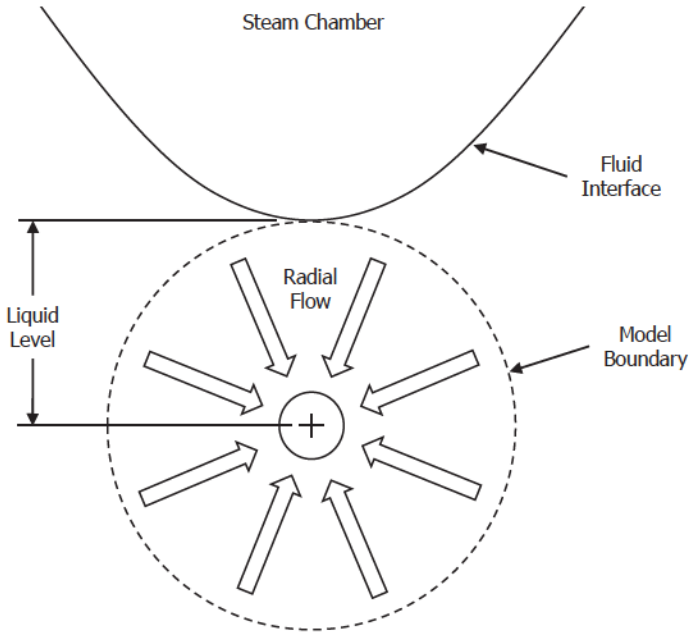

Figure 3.2: Radial flow in an isotropic reservoir

The assumption of radial flow (or flow with elliptical equipotentials) is based on the conditions in the near-wellbore reservoir, where the flow area is smallest, the flow velocity is highest, and the potential loss is largest. Although the assumption is invalid far from the production well, the potential gradient is thought to diminish rapidly with increasing distance from the well, such that the accurate characterization of the velocity field becomes less and less important.

3.1.3 Steady Flow

The growth of the SAGD steam chamber is a long-timescale process. Initially, the steam chamber grows upwards and laterally outwards from the injection well. Once the steam chamber reaches the caprock, the relatively impermeable rock overlying the reservoir, its growth continues in the lateral direction. Eventually, the steam chamber above one well pair may coalesce with the steam chambers above neighbouring well pairs. Through numerical simulation, Zhao et al. (2003) have shown the economical life of a prototypical well pair to be four to five years, after which they recommend the injection (or co-injection) of a non-condensable gas (NCG) to initiate a wind-down process which may itself last years. The Dover SAGD Pilot demonstrated the timescale of the SAGD process – steam injection into the Phase B wells began in 1993 and was followed by NCG co-injection in 1998, which persisted until 2002 (Aherne and Maini 2008).

By contrast, the processes in the steam trap are believed to occur on a much shorter timescale. If the steam trap is thought of as a liquid pool that is continuously drained from below and refilled from above, then a volume calculation suggests that the liquid pool is "replaced" every few days under typical operating conditions. For example, if the shape of the steam chamber is assumed to be a sector of a circle with a

central angle of 64° (Butler 1997) and 3 m of liquid is assumed to have pooled at the bottom of the steam chamber, then with a reservoir porosity of 0.33 and a production rate of 1 m^3/day of liquids per metre of well length, the liquid pool is replaced every 1.9 days. During stable SAGD processes, the fluid interface is therefore expected to move rapidly to an equilibrium position where the rates at which the liquid pool is drained and refilled are equal. The GIPR assumes that the fluid interface has reached such an equilibrium position and that the flow in the steam trap has reached a steady state.

3.1.4 Spatially Uniform Fluid Viscosities

The temperature in the steam trap is non-uniform. At the fluid interface, the temperature is equal to the steam chamber temperature, which often exceeds 200 °C. Far from the fluid interface, the temperature approaches the initial reservoir temperature, which is typically about 10 °C in the Athabasca oil sands (Devon 2013; Nexen 2014; Suncor 2014; Cenovus 2014a,b). Consequently, there are large temperature gradients in the steam trap that lead to large gradients in the fluid viscosities. Figure 3.3 shows the variation in the dynamic viscosities of bitumen and water with temperature. The dynamic viscosity of bitumen was calculated using the following equations from Butler (1997) for the kinematic viscosity, ν, and density, ρ, of heavy oils:

$$\log_{10}\left[\log_{10}(\nu + 0.7)\right] = m \log_{10}(T + 273) + b \tag{3.1}$$

$$\rho = \rho_{15}\left[1 - 0.06285\left(\frac{T-15}{100}\right) + 0.001426\left(\frac{T-15}{100}\right)^2\right] \tag{3.2}$$

where T is the temperature in degrees Celsius, ρ_{15} is the density at 15 °C, b is an oil-specific constant, and $m = 0.3249 - 0.4106b$. Figure 3.3 was generated assuming $\rho_{15} = 1013$ kg/m^3, corresponding to an API gravity of 8.1°, and assuming $b = 9$, a median value for the heavy oils on which Equation 3.1 is based. Note that the vertical scale for the bitumen viscosity is logarithmic.

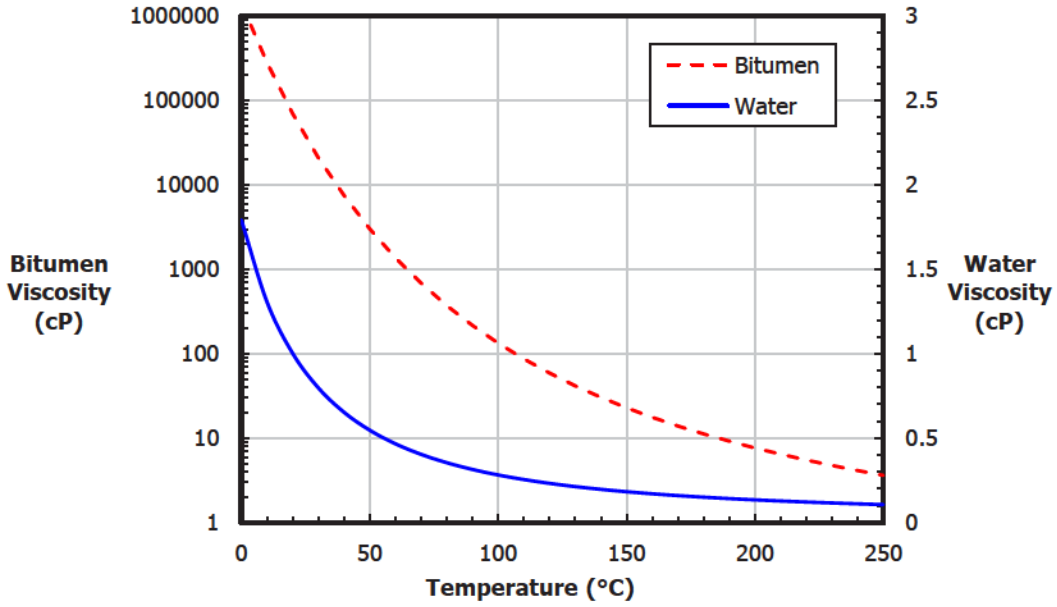

Figure 3.3: Variation of fluid viscosities with temperature

Spatial variation of the fluid viscosities adds considerable complexity to the derivation of a GIPR. It is expected, however, that most of the potential loss occurs very near to the wellbore, where the flow area is smallest and the flow velocity is highest - perhaps within a few diameters of the wellbore at moderate liquid levels. It is thus expected that the potential loss is governed by the fluid viscosities in the near-wellbore region. On this basis, spatial variation of the fluid viscosities is neglected in the formulation of the GIPR, and the fluid viscosities are instead evaluated at the *inflow temperature* – the temperature of the fluids when they enter the production well. Given the large temperature gradients in the steam trap, there

is likely some temperature variation around the circumference of the wellbore, and so the inflow temperature is more precisely defined as the *average* temperature of the fluids entering the production well.

The relationship between the inflow temperature and the other model parameters is left to be investigated through numerical simulation in Chapter 4. A linear relationship between the inflow temperature and the liquid level is suggested by the rule of thumb that the subcool in the production well increases by 10 °C for every metre of liquid above the well; however, it will be shown in Section 4.3.5 that the relationship is case specific and highly dependent on the inflow rate.

3.1.5 Negligible Capillary Pressure

In oil-water systems, interfacial tension gives rise to a pressure difference between the oil and water phases called the *capillary pressure*. Leverett (1941, 1942) has proposed that the capillary pressure in a reservoir scales with the inverse square root of the permeability, k, according to

$$P_c = \gamma j(S_w)\sqrt{\frac{\phi}{k}} \tag{3.3}$$

where γ is the interfacial tension between oil and water, ϕ is the reservoir porosity, and $j(S_w)$ is a dimensionless function of the water saturation commonly called the *Leverett j-function*.[1]

The literature suggests that the capillary pressure is often neglected in analytical and numerical studies of the SAGD process because of the high permeability of the oil sands in which SAGD is applied. Mukherjee et al. (1995) attribute success in SAGD

[1] An upper-case J is often used to denote the Leverett j-function. Here, the lower-case j is favoured for consistency with Leverett et al. (1942).

modelling to the dominant role of gravity and the consistency of gravity relative to other displacement processes. Walls et al. (2003) conclude that "capillary effects are neglected in the literature as being insignificant compared to gravity drainage during modelling of field applications of SAGD" (43).

On the basis that the capillary forces are small relative to the gravity and viscous forces in most SAGD applications, the GIPR neglects capillarity and assumes equal pressures in the oil and water phases.

3.1.6 Negligible Density Contrast

At virgin reservoir conditions, the density of bitumen is higher than that of water (earning it the byname of *extra heavy oil*). The densities of both bitumen and water are functions of temperature, however, and so the density contrast between bitumen and water may grow or diminish with increasing temperature. Figure 3.4 compares the densities of bitumen and water between 0 °C and 250 °C. The density of bitumen was calculated using Equation 3.2 assuming $\rho_{15} = 1013$ kg/m^3 (corresponding to an API gravity of 8.1°).

To facilitate an analytical solution, the GIPR neglects the density contrast between bitumen and water. An average fluid density is calculated based on the *water cut*, the volume fraction of water in the production fluid. The error arising from this simplification is expected to be acceptable because the density contrast between bitumen and water is small (less than 10% in Figure 3.4). Calculation of the fluid density is discussed further in Section 3.2.4.

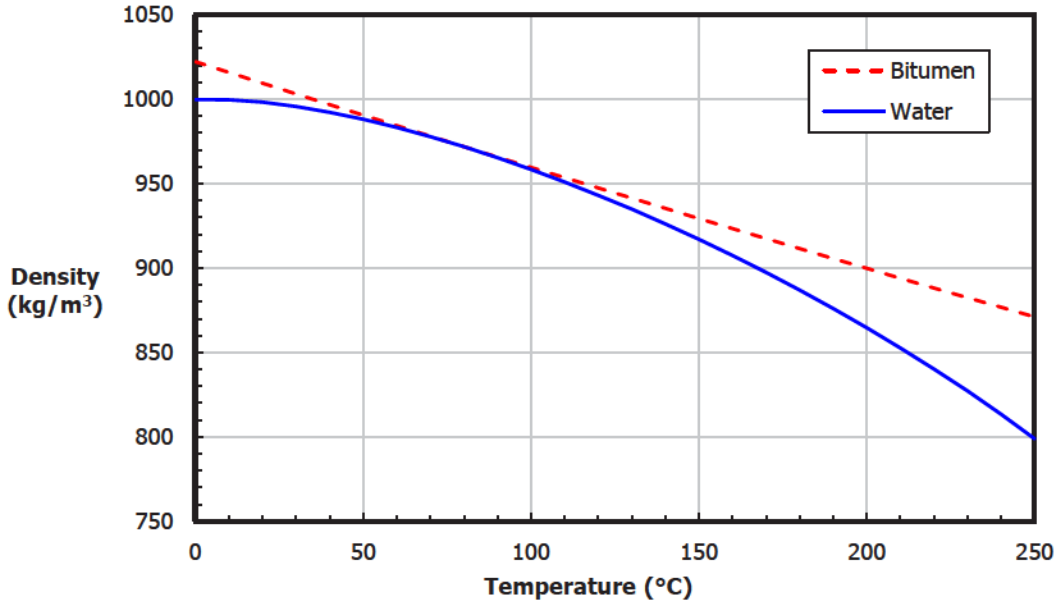

Figure 3.4: Comparison of the densities of water and bitumen

3.2 Formulation

3.2.1 Isotropic Permeability

Given the assumptions of Section 3.1, the flow through the steam trap of a reservoir with isotropic permeability is described by Darcy's law for steady, radial flow:

$$u_i = \frac{k_i \rho_i}{\mu_i} \frac{d\Phi_i}{dr} \tag{3.4}$$

where u_i is the superficial flow velocity, k_i is the permeability of the reservoir, ρ_i is the density of the fluid, μ_i is the dynamic viscosity of the fluid, and Φ_i is the fluid potential. The subscript i denotes the fluid phase (o for oil or w for water). Positive values for the flow velocity correspond to production (rather than injection). For an

incompressible fluid, the fluid potential is given by

$$\Phi_i = \frac{P_i}{\rho_i} + gz \tag{3.5}$$

where P_i is the pressure of the fluid, g is the acceleration due to gravity, and z is the elevation. If the fluid density is assumed to be spatially uniform, then substituting Equation 3.5 into Equation 3.4 yields

$$u_i = \frac{k_i}{\mu_i}\left(\frac{\partial P_i}{\partial r} + \rho_i g \sin\theta\right) \tag{3.6}$$

where θ is defined relative to horizontal. The flow velocity is simply the volumetric flow rate divided by the flow area, and so Equation 3.6 may be rewritten as

$$\frac{q_i}{2\pi r} = \frac{k_i}{\mu_i}\left(\frac{\partial P_i}{\partial r} + \rho_i g \sin\theta\right) \tag{3.7}$$

Isolating the specific inflow rate, q_i, on the left-hand side of the equation yields

$$q_i = \frac{2\pi k_i r}{\mu_i}\left(\frac{\partial P_i}{\partial r} + \rho_i g \sin\theta\right) \tag{3.8}$$

It is assumed that only oil and liquid water flow through the steam trap (i.e., any exsolution of gas is neglected). The total volumetric flow rate may therefore be expressed as the sum of the oil and water flow rates:

$$q = q_o + q_w \tag{3.9}$$

Substituting Equation 3.8 into Equation 3.9 for oil and water yields

$$q = \frac{2\pi k_o r}{\mu_o}\left(\frac{\partial P_o}{\partial r} + \rho_o g \sin\theta\right) + \frac{2\pi k_w r}{\mu_w}\left(\frac{\partial P_w}{\partial r} + \rho_w g \sin\theta\right) \tag{3.10}$$

The permeability of the reservoir to oil generally differs from the permeability to water. It is convenient to express the permeability to each fluid as the product of a reference permeability, k, and a fluid-specific modifier:

$$k_o = k k_{ro} \tag{3.11}$$

$$k_w = k k_{rw} \tag{3.12}$$

The modifiers k_{ro} and k_{rw} are called the *relative permeability to oil* and the *relative permeability to water*, respectively. Calculation of the relative permeabilities is discussed in Section 3.2.3. Substituting Equations 3.11 and 3.12 into Equation 3.10 yields

$$q = \frac{2\pi k k_{ro} r}{\mu_o}\left(\frac{\partial P_o}{\partial r} + \rho_o g \sin\theta\right) + \frac{2\pi k k_{rw} r}{\mu_w}\left(\frac{\partial P_w}{\partial r} + \rho_w g \sin\theta\right) \tag{3.13}$$

The capillary pressure and the density contrast between oil and water are assumed to be negligible:

$$P_c = P_o - P_w = 0 \tag{3.14}$$

$$\Delta\rho = \rho_o - \rho_w = 0 \tag{3.15}$$

Equation 3.13 reduces to

$$q = \frac{2\pi k r}{\mu_a}\left(\frac{\partial P}{\partial r} + \rho g \sin\theta\right) \tag{3.16}$$

where μ_a is called the *apparent fluid viscosity*[2] and given by

$$\mu_a = \left(\frac{k_{ro}}{\mu_o} + \frac{k_{rw}}{\mu_w} \right)^{-1} \tag{3.17}$$

The pressure distribution in the steam trap is obtained by integrating Equation 3.16 with respect to r to yield

$$P(r, \theta) = \frac{\mu_a q}{2\pi k} \ln r - \rho g r \sin\theta + A \tag{3.18}$$

where A is a constant of integration to be determined from the boundary condition at the production well. For the flow to be radial, the fluid potential must be uniform around the circumference of the production well (recall that the equipotentials for radial flow are circular). This requirement is satisfied by the following boundary condition:

$$P(R_p, \theta) = P_p - \rho g R_p \sin\theta \tag{3.19}$$

where R_p is the radius of the production well and P_p is the average pressure at the production well. Substituting Equation 3.19 into Equation 3.18 yields

$$P(r, \theta) = P_p + \frac{\mu_a q}{2\pi k} \ln \left(\frac{r}{R_p} \right) - \rho g r \sin\theta \tag{3.20}$$

Note that Equation 3.20 gives the hydrostatic pressure distribution when the flow rate is zero, as expected.

The flow through the steam trap is assumed to be bounded by a circular

[2]The apparent fluid viscosity is the inverse of the *total relative mobility*, a concept that appears in the literature on enhanced oil recovery. Here, the notion of an apparent viscosity is favoured for its compatibility with single-phase flow theory.

equipotential defined by the liquid level, h, and the steam chamber pressure, P_{sc}:

$$P(h,\theta) = P_{sc} + \rho g h(1 - \sin\theta) \tag{3.21}$$

By substituting Equation 3.21 into Equation 3.20, the GIPR is obtained:

$$P_{sc} - P_p + \rho(T_p)gh = \frac{\mu_a(T_p)q}{2\pi k} \ln\left(\frac{h}{R_p}\right) \tag{3.22}$$

Note that the fluid density, ρ, and the apparent fluid viscosity, μ_a, are evaluated at the inflow temperature, T_p. Equation 3.22 differs from similar models in several ways:

1. Radial flow is assumed instead of flow from a line source (Ong and Butler 1990) or flow through a wedge (Yuan and Nugent 2013).

2. The potential loss is based on the apparent fluid viscosity, μ_a, which accounts for relative permeability effects, instead of the oil viscosity (Ong and Butler 1990) or an emulsion viscosity (Yuan and Nugent 2013).

3. The fluid properties are evaluated at the inflow temperature, T_p, which may be assumed constant or coupled to other variables, such as the liquid level.

It is common to include a calibration factor called a *skin factor* in Darcy's law to account for reductions in the near-wellbore permeability associated with phenomena such as plugging. A skin factor, s, may be included in the GIPR to yield

$$P_{sc} - P_p + \rho(T_p)gh = \frac{\mu_a(T_p)q}{2\pi k} \left[\ln\left(\frac{h}{R_p}\right) + s\right] \tag{3.23}$$

3.2.2 Anisotropic Permeability

In the preceding section, a GIPR was derived for a reservoir with isotropic permeability. In general, however, the reservoir permeability can be represented by a second-order tensor:

$$\overline{\overline{k}} = \begin{bmatrix} k_{xx} & k_{xy} & k_{xz} \\ k_{yx} & k_{yy} & k_{yz} \\ k_{zx} & k_{zy} & k_{zz} \end{bmatrix} \tag{3.24}$$

where, for example, the permeability k_{xy} relates the flow velocity in the x-direction to the potential gradient in the y-direction.

To extend the GIPR to reservoirs with anisotropic permeability, it is again assumed that the flow is two-dimensional. In addition, it is assumed that the principal directions of the permeability tensor are aligned with the coordinate axes so that the off-diagonal elements are zero. Then, for single-phase flow, Darcy's law may be written for the horizontal (x) and vertical (z) directions as

$$u_x = -\frac{k_x \rho}{\mu} \frac{\partial \Phi}{\partial x} \tag{3.25}$$

$$u_z = -\frac{k_z \rho}{\mu} \frac{\partial \Phi}{\partial z} \tag{3.26}$$

where $k_x = k_{xx}$ and $k_z = k_{zz}$. Mass conservation for steady, incompressible flow requires that

$$\frac{\partial u_x}{\partial x} + \frac{\partial u_z}{\partial z} = 0 \tag{3.27}$$

Substituting Equations 3.25 and 3.26 into Equation 3.27 gives the governing equation

for steady flow in an anisotropic reservoir:

$$k_x \frac{\partial^2 \Phi}{\partial x^2} + k_z \frac{\partial^2 \Phi}{\partial z^2} = 0 \tag{3.28}$$

Following the method devised by Muskat (1937) and developed by Peaceman (1983), the following coordinate transformations are introduced:

$$x^* = \left(\frac{k_z}{k_x}\right)^{\frac{1}{4}} x \tag{3.29}$$

$$z^* = \left(\frac{k_x}{k_z}\right)^{\frac{1}{4}} z \tag{3.30}$$

Substituting Equations 3.29 and 3.30 into Equation 3.28 yields

$$\sqrt{k_x k_z} \frac{\partial^2 \Phi}{\partial x^{*2}} + \sqrt{k_x k_z} \frac{\partial^2 \Phi}{\partial z^{*2}} = 0 \tag{3.31}$$

Thus, flow in the $x - z$ plane with anisotropic permeabilities k_x and k_z is equivalent to flow in the transformed $x^* - z^*$ plane with an isotropic permeability of $\sqrt{k_x k_z}$.

When the permeability of a reservoir is anisotropic, the horizontal permeability is generally greater than the vertical permeability. In such cases, the equipotentials in the steam trap are expected to be elongated horizontally and compressed vertically. Therefore, whereas the flow is bounded by a circular equipotential in an isotropic reservoir, the flow is assumed to be bounded by an elliptical equipotential in an anisotropic reservoir:

$$\Phi = \Phi_{sc} \quad at \quad \frac{x^2}{\left[\left(\frac{k_x}{k_z}\right)^{\frac{1}{2}} h\right]^2} + \frac{z^2}{h^2} = 1 \tag{3.32}$$

Equation 3.32 is an ellipse with the minor axis defined by the liquid level. The ellipse

transforms into a circle in the $x^* - z^*$ plane:

$$\Phi = \Phi_{sc} \quad at \quad r^* = \sqrt{x^{*2} + z^{*2}} = \left(\frac{k_x}{k_z}\right)^{\frac{1}{4}} h \tag{3.33}$$

The physical boundary condition at the production well is a circular equipotential in the $x - z$ plane at $r = R_p$, which transforms into an ellipse in the $x^* - z^*$ plane. An elliptical boundary in the $x^* - z^*$ plane renders the solution of Equation 3.31 challenging, and so it is instead assumed that the flow converges to an elliptical equipotential near the production well defined by

$$\Phi = \Phi_p \quad at \quad \frac{x^2}{\left[\left(\frac{k_x}{k_z}\right)^{\frac{1}{4}} R_p\right]^2} + \frac{z^2}{\left[\left(\frac{k_z}{k_x}\right)^{\frac{1}{4}} R_p\right]^2} = 1 \tag{3.34}$$

Equation 3.34 transforms into a circle in the $x^* - z^*$ plane with radius R_p:

$$\Phi = \Phi_p \quad at \quad r^* = \sqrt{x^{*2} + z^{*2}} = R_p \tag{3.35}$$

Figure 3.5 shows the model boundaries in the $x-z$ plane (left) and in the transformed $x^* - z^*$ plane (right). The error resulting from simplifying the boundary condition at the production well is expected to be acceptable provided $\frac{k_z}{k_x}$ does not deviate too drastically from unity. A review of performance presentations by SAGD operators to the AER indicates that a typical value for $\frac{k_z}{k_x}$ is 0.5 in the Athabasca oil sands (Cenovus 2014a,b; Devon 2013; Nexen 2014; Suncor 2014) – considerably closer to unity than in many conventional reservoirs. In addition, it is speculated that the sand disturbance associated with the borehole collapsing around the production liner reduces anisotropy in the near-wellbore region.

Thus, the problem is reduced to radial flow in the $x^* - z^*$ plane, for which the

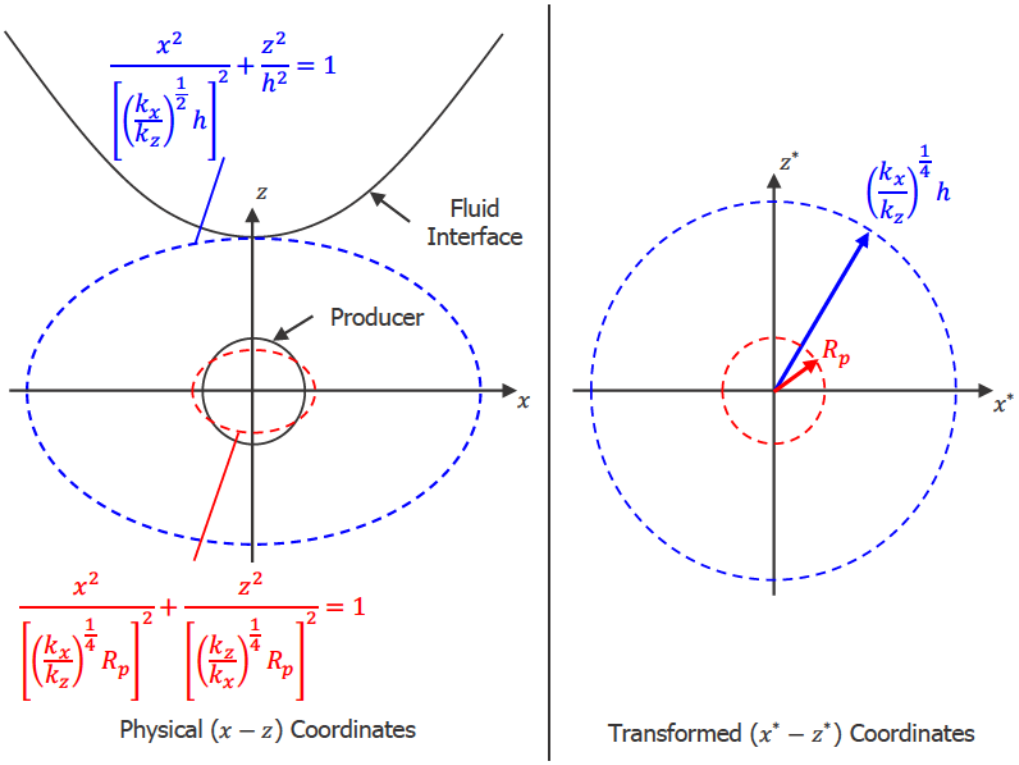

Figure 3.5: Model boundaries for reservoir with anisotropic permeability

solution is

$$\Phi_{sc}-\Phi_p=\frac{\mu q}{2\pi\rho\sqrt{k_xk_z}}\ln\left[\frac{\left(\frac{k_x}{k_z}\right)^{\frac{1}{4}}h}{R_p}\right] \tag{3.36}$$

To model the flow of oil and water, the single-phase fluid viscosity, μ, is replaced by the apparent fluid viscosity, μ_a. After expressing the fluid potentials in terms of pressure, the GIPR for an anisotropic reservoir is obtained:

$$P_{sc}-P_p+\rho(T_p)gh=\frac{\mu_a(T_p)q}{2\pi\sqrt{k_hk_v}}\left\{\ln\left[\frac{\left(\frac{k_h}{k_v}\right)^{\frac{1}{4}}h}{R_p}\right]+s\right\} \tag{3.37}$$

The subscripts x and z have been replaced by the more general subscripts h and v,

and a skin factor, s, has been included to account for reductions in the near-wellbore permeability. Note that Equation 3.37 reduces to the isotropic form when $k_h = k_v$.

3.2.3 Relative Permeability

When oil and water flow simultaneously through a porous medium, the permeability of the medium to oil generally differs from the permeability to water. This effect is typically captured by expressing the permeability to each fluid as the product of a reference permeability, k, and a fluid-specific relative permeability, k_{ri}:

$$k_i = k k_{ri} \tag{3.38}$$

The relative permeability to each fluid generally depends on the amounts of oil and water present. Oil-water relative permeability data is typically obtained in laboratory tests (Lake 1989) and presented as a function of the water saturation. Figure 3.6 shows oil-water relative permeability curves based on the work of Good et al. (1997) that are representative of the Athabasca oil sands.

Equation 3.37 is not immediately useful since it includes the apparent fluid viscosity, μ_a, which depends on the unknown relative permeabilities, k_{ro} and k_{rw}. Even when oil-water relative permeability curves are available, determining k_{ro} and k_{rw} requires knowledge of the water saturation in the near-wellbore region. Fortunately, the relative permeabilities are related to a parameter that is readily measured – the water cut. Dividing Equation 3.8 for oil by the same equation for water yields

$$\frac{q_o}{q_w} = \frac{k_{ro}\mu_w}{k_{rw}\mu_o} \tag{3.39}$$

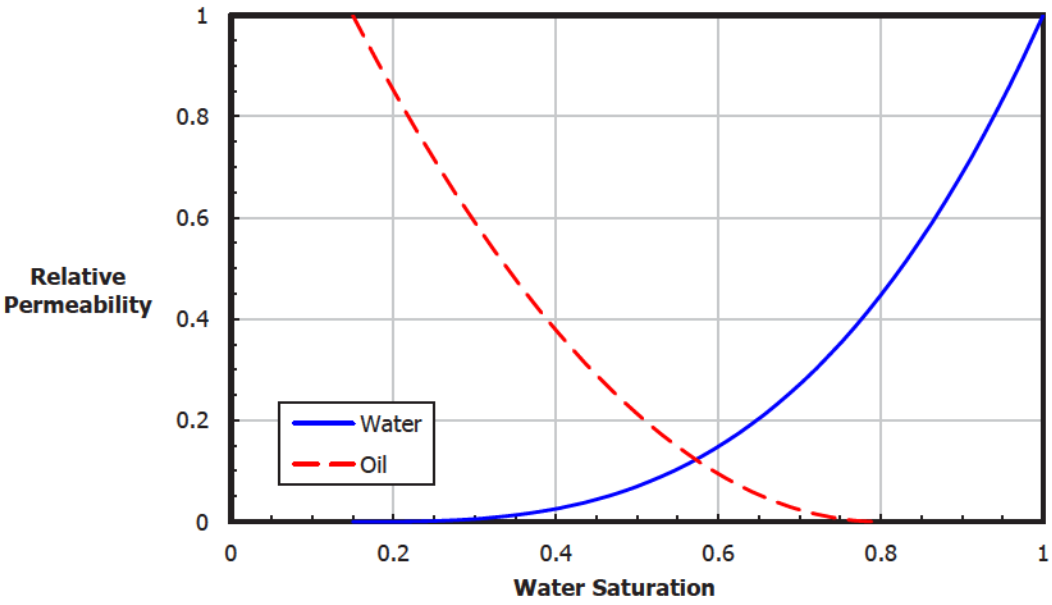

Figure 3.6: Sample oil-water relative permeability curves

By introducing the water cut, f_w, Equation 3.39 may be rewritten as

$$\frac{q(1-f_w)}{qf_w} = \frac{k_{ro}\mu_w}{k_{rw}\mu_o} \tag{3.40}$$

or

$$\frac{k_{ro}}{k_{rw}} = \frac{\mu_o}{\mu_w}\left(\frac{1}{f_w} - 1\right) \tag{3.41}$$

Equation 3.41 is the *fractional flow equation* presented by Buckley and Leverett (1942). Typically, k_{ro} is strictly decreasing with water saturation, while k_{rw} is strictly increasing. In such cases, the ratio of relative permeabilities, $\frac{k_{ro}}{k_{rw}}$, is strictly decreasing with water saturation; each value for $\frac{k_{ro}}{k_{rw}}$ corresponds to unique values for k_{ro} and k_{rw}. Thus, Equation 3.41 may be used to calculate $\frac{k_{ro}}{k_{rw}}$ from the oil viscosity, water viscosity, and water cut. Then, the corresponding values for k_{ro} and k_{rw} may be obtained from a table of relative permeability data using a lookup routine.

3.2.4 Fluid Density

The derivations of Sections 3.2.1 and 3.2.2 neglect the density contrast between oil and water. Instead, a mixture density is calculated based on the water cut and the oil and water densities:

$$\rho = f_w \rho_w + (1 - f_w)\rho_o \tag{3.42}$$

As discussed in the preceding sections, the fluid viscosities are evaluated at the inflow temperature on the basis that the potential loss is highest in the near-wellbore region. For consistency, the mixture density is also evaluated at the inflow temperature.

3.3 Summary

The GIPR relates the liquid level, which cannot be measured directly, to parameters that are more readily measured – the inflow rate, steam chamber and production well pressures, reservoir permeability, and fluid properties. The GIPR is based on the following simplifying assumptions:

- The interface between the steam chamber and the steam trap is well-defined, and the flow in the steam trap is two-phase (oil and liquid water).
- The flow in the steam trap is two-dimensional. For isotropic reservoirs, the flow is radial and the equipotentials are circular; for anisotropic reservoirs, the equipotentials are elliptical.
- The flow in the steam trap is steady and the fluid interface is static.
- The fluid viscosities and densities are spatially uniform.

- The capillary pressure and density contrast between oil and water are negligible.

The GIPR is given by

$$P_{sc} - P_p + \rho(T_p)gh = \frac{\mu_a(T_p)q}{2\pi\sqrt{k_h k_v}} \left\{ \ln \left[\frac{\left(\frac{k_h}{k_v}\right)^{\frac{1}{4}} h}{R_p} \right] + s \right\}$$

where

$$\mu_a(T_p) = \left[\left(\frac{k_{ro}}{\mu_o} + \frac{k_{rw}}{\mu_w} \right)^{-1} \right]_{T_p}$$

and

$$\rho(T_p) = [f_w \rho_w + (1 - f_w)\rho_o]_{T_p}$$

The relative permeabilities, k_{ro} and k_{rw}, are determined from their unique ratio:

$$\frac{k_{ro}}{k_{rw}} = \frac{\mu_o}{\mu_w} \left(\frac{1}{f_w} - 1 \right)$$

For a reservoir with isotropic permeability, $k_h = k_v = k$.

Chapter 4

Model Verification Against Simulations Using Higher-Order Numerical Model

This chapter presents the results of reservoir simulations conducted to validate the GIPR. The validation approach is discussed, including the capabilities and limitations of reservoir simulation. The simulation procedure and the basis for selecting the experimental variables are described. The simulation results are compared against the predictions of the GIPR for isotropic and anisotropic reservoirs. A correction to the GIPR is proposed to improve agreement with the simulation results.

4.1 Approach

SAGD is a partially observable process. Operators can measure pressures, temperatures, and flow rates at the wellheads of the injector and producer. With recent advances in instrumentation, operators can also install distributed temperature sensing (DTS)

systems in the producer to obtain high-resolution temperature data using fibre-optic technology. Operators cannot, however, observe steam exiting the injection well, condensing at the edge of the steam chamber, and draining alongside bitumen to the production well. Similarly, operators cannot observe the position of the fluid interface but must instead rely on pressure and temperature measurements to infer the liquid level.

Because most field measurements are made at the wellhead, it is difficult to validate models of reservoir processes using field data. Some description of the flow in the wellbore – and, for thermal processes like SAGD, the heat transfer – is required to relate the model parameters, which are defined at reservoir conditions, to the field measurements, which are taken at surface. The outputs of coupled reservoir-wellbore models may be compared to field data, but little insight is gleaned into the validity of specific model assumptions.

Given the scarcity of downhole field data, this project employed an alternate validation approach, whereby the predictions of the GIPR were compared against those of a commercial reservoir simulator. STARS by Computer Modelling Group Ltd. (see Computer Modelling Group Ltd. 2015) was selected from the available simulators for its pedigree in the SAGD industry. Researchers have validated STARS models against laboratory and field data in studies focused on the vertical and lateral growth of the SAGD steam chamber (Chow and Butler 1996), the counter-current flow of rising steam and draining liquids (Nasr et al. 2000), the impacts of the initial gas-to-oil ratio on SAGD (Yuan et al. 2003), and the economic optimization of commercial SAGD operations (Yang et al. 2009), to list but a few examples.

Whereas the GIPR makes several simplifying assumptions to permit an analytical solution, STARS discretizes the reservoir into numerous grid blocks and seeks a numerical solution. There is no intrinsic assumption of the flow direction, and

the discretization error may be managed by reducing the size of the grid blocks (albeit with a stiff penalty to the solution time). STARS simulates the flow of up to three fluid phases – oil, water, and gas – and so it is capable of modelling both the steam chamber and the steam trap. While there remains uncertainty about the accuracy with which commercial simulators describe certain physics of the SAGD process, reservoir simulation enables the error resulting from the GIPR's simplifying assumptions to be quantified.

A suite of reservoir simulation cases was designed to benchmark the GIPR under a range of conditions. The objectives of the simulations were twofold:

1. To quantify the error resulting from the GIPR's simplifying assumptions: The GIPR makes several simplifying assumptions to permit an analytical solution – namely, of a well-defined fluid interface, steady radial flow (or flow with elliptical equipotentials for anisotropic reservoirs), and uniform fluid properties. The liquid levels predicted by STARS were compared against those predicted by the GIPR for the same conditions to quantify the error resulting from these assumptions.

2. To characterize the temperature distribution in the steam trap: The temperature distribution in the steam trap governs the viscosity of the production fluids, and so its accurate characterization is essential to the development of an accurate GIPR. The relationships between the inflow temperature and other parameters, such as the liquid level, are of particular interest.

The reservoir simulations were based on Suncor Energy's Firebag project, one of the largest SAGD projects in the Athabasca oil sands (see JuneWarren-Nickle's Energy Group 2015). The baseline inputs for the simulations were established through consultation with the Firebag Resource Team at Suncor and are intended to

represent a typical Firebag well pair. Parameters were manipulated if they satisfied two criteria: (1) the parameter was expected to vary significantly between SAGD projects in the Athabasca oil sands, and (2) the parameter was expected to influence the agreement between the GIPR and STARS. The resulting case matrix approached a two-level, full-factorial simulation design. The variable selection process and case matrix are discussed further in Sections 4.2.2 and 4.2.3, respectively.

4.2 Reservoir Simulation Design

4.2.1 Model Creation

Figure 4.1 shows a schematic of the STARS model created to verify the GIPR. The model is two-dimensional and includes a single SAGD well pair. The size of the model is reduced by half by specifying symmetry constraints on a vertical line passing through the injection and production wells. In practice, SAGD well pairs are drilled side by side from a single pad at surface, and so symmetry constraints are also enforced at the opposing boundary so that the model represents an interior well pair with neighbouring well pairs on either side. No-flow boundary conditions (BC) are enforced at the upper and lower boundaries of the model to represent an impermeable overburden and an impermeable underburden. Heat losses to the overburden and underburden are calculated using an analytical model, which is described in Section 4.2.5.

At virgin conditions, bitumen is too viscous to flow; the reservoir must be preheated before SAGD is feasible. In practice, this is usually achieved by circulating steam in the injection and production wells. Steam is injected down tubing that terminates near the end of the well, and it returns to the surface through the annulus between

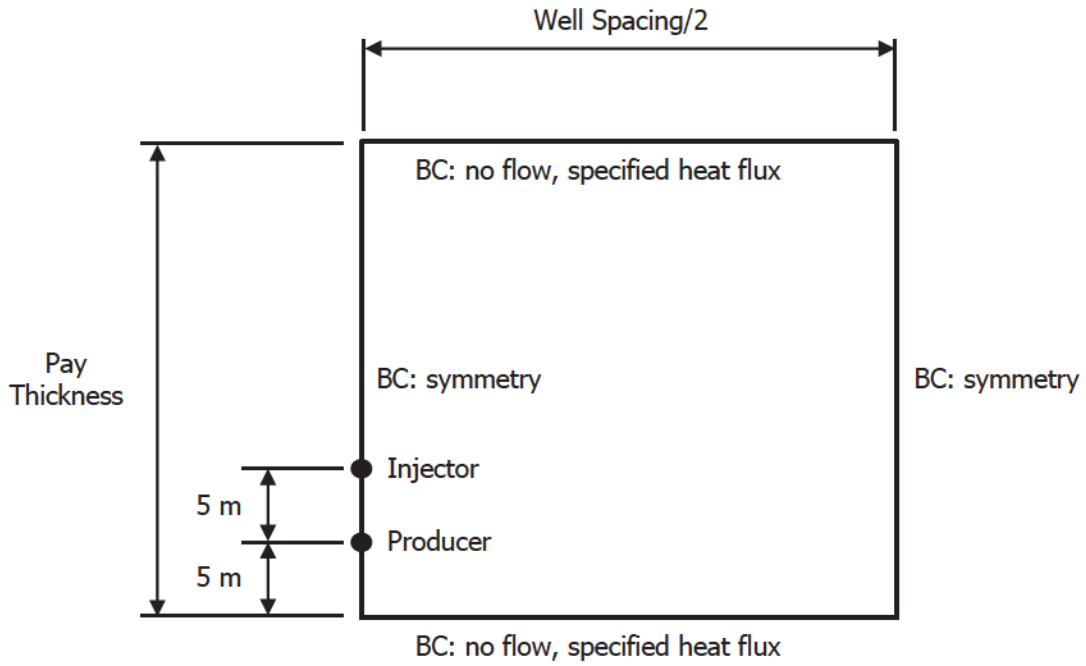

Figure 4.1: Schematic of STARS model

the tubing and the slotted liner, heating the reservoir by conduction. To replicate steam circulation in the STARS simulations, temperature boundary conditions were specified at the injection and production wells for three months, during which the conductive heating of the reservoir was modelled. After three months, the well pair was converted to SAGD by specifying the steam pressure and steam quality at the injection well, along with the pressure at the production well. The start-up procedure is detailed in Section 4.2.4.

Figure 4.2 shows a screenshot of the STARS model illustrating the discretization of the reservoir into grid blocks. A grid block size of 25 cm horizontally by 12.5 cm vertically was used in the near-wellbore region to resolve the fluid interface. Coarser grid blocks were used in the far field to manage the total grid block count. The grid design process, including grid sensitivity analysis, is described in Appendix C. Note that the grid blocks falling along the line of symmetry at the well pair do not display

correctly in screenshots. These grid blocks appear to have the same volume as the interior grid blocks, but their volume is reduced by half in the model equations (along with the appropriate flow areas) to account for symmetry.

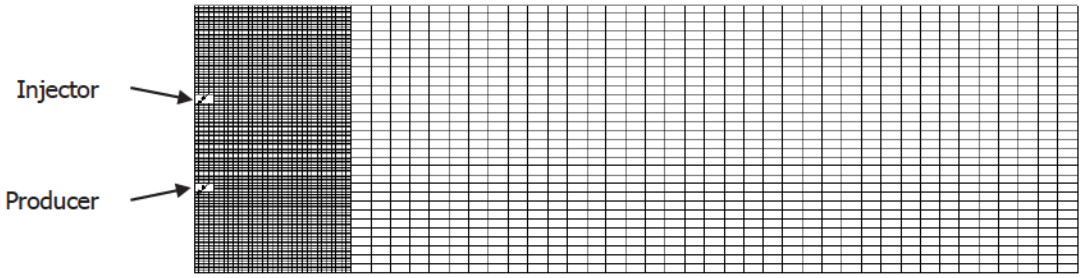

Figure 4.2: Screenshot of STARS model

4.2.2 Variable Selection

The primary objective of the GIPR is to predict the liquid level above the production well. The liquid level was therefore selected to be the primary responding (dependent) variable of the STARS simulations. The validity of the GIPR was assessed based on the consistency with which it and STARS predict the liquid level under a range of conditions.

The manipulated (independent) variables of the STARS simulations were selected from among the parameters that appear in the GIPR – namely, the steam chamber and production well pressures, the inflow rate, the fluid viscosities and densities, the reservoir permeability, and the production well radius. Each parameter was assessed based on the extent to which it was expected to vary between SAGD projects and the extent to which it was expected to affect the agreement between the GIPR and STARS. Parameters that were expected to have both significant variability and significant influence were manipulated in the STARS simulations. All other

parameters were controlled (i.e., held constant).

Temperature effects are captured indirectly in the GIPR by evaluating the fluid viscosities and densities at the inflow temperature. To characterize the inflow temperature, additional manipulated variables were selected by considering the equation governing the temperature distribution in the steam trap. Assuming the solid and fluid phases are in thermal equilibrium, the equation may be expressed as (Nield and Bejan 2013)

$$(\rho c)_m \frac{\partial T}{\partial t} + (\rho c)_f \overline{u} \cdot \nabla T = \nabla \cdot (\kappa_m \nabla T) + q'''_m \tag{4.1}$$

where ρc is volumetric heat capacity, κ is thermal conductivity, and q''' is heat generation per unit volume. The subscript m denotes properties of the mixed solid-fluid system; f denotes fluid properties.

The quasi-steady-state temperature distribution in the steam trap is of primary interest, and there is no heat generation. Equation 4.1 reduces to:

$$(\rho c)_f \overline{u} \cdot \nabla T = \nabla \cdot (\kappa_m \nabla T) \tag{4.2}$$

Equation 4.2 shows that the quasi-steady-state temperature distribution depends on the thermal conductivity of the solid-fluid system, which governs heat transfer by conduction, and the flow velocity and fluid volumetric heat capacity, which govern heat transfer by convection. The temperature distribution also depends on the boundary conditions on Equation 4.2 – namely, the steam chamber temperature and the initial (far-field) reservoir temperature.

Steam Chamber and Production Well Pressures

The GIPR indicates that the liquid level is a strong function of the pressure difference between the steam chamber and the production well. In practice, SAGD operators control the steam chamber pressure by adjusting the pressure in the injection well. The pressure in the production well may be controlled by adjusting the pump settings, when mechanical lift is employed, or the lift gas settings, when production fluids are lifted to the surface by injecting gas near the heel of the well.

In the reservoir simulations, the pressure difference between the steam chamber and the production well was manipulated to study its effect on the liquid level. In STARS, both the injection well pressure and the production well pressure may be specified. Because the focus of this project is the influence of the production well on the steam trap, the production well pressure was chosen as the manipulated variable, and the injection well pressure was controlled. Note that, because the fluid in the injection well is at saturated conditions, fixing the injection well pressure also fixes the injection well temperature and, in turn, the temperature in the steam chamber.

Inflow Rate

The GIPR suggests that the liquid level is also a strong function of the inflow rate. In addition, the inflow rate is expected to influence whether the heat transfer in the steam trap is conduction or convection dominated. In practice and in simulation, the inflow rate is not typically manipulated or controlled. Instead, it is governed by the reservoir properties, the fluid properties, and the size and shape of the steam chamber.

The rate at which oil drains from the steam chamber to the steam trap – which, under stable conditions, is equal to the inflow rate of oil – may be estimated using

the TANDRAIN equation developed by Butler and Stephens (1981):

$$q_o = 2\sqrt{\frac{1.5kg\alpha\phi\Delta S_o H}{m\nu_{sc}}} \tag{4.3}$$

where α is the reservoir thermal diffusivity, ΔS_o is the difference between the initial and residual oil saturations, H is the steam chamber height, ν_{sc} is the oil kinematic viscosity at the steam chamber temperature, and m is a parameter that describes the change in the oil viscosity with temperature. Among the parameters in Equation 4.3 with the greatest expected variability are the oil viscosity, the reservoir permeability, and the reservoir thermal diffusivity, each of which is addressed in a subsequent section. The steam chamber height is governed by the thickness of the reservoir, or *pay thickness*, and so it also varies significantly between SAGD projects.

In the reservoir simulations, the pay thickness was manipulated to vary the inflow rate, permitting its effect on the liquid level to be studied. This approach was favoured because pay thickness variations were expected to have fewer side effects on the flow and heat transfer in the steam trap than variations to other parameters.

Note that the liquid level itself also affects the drainage rate, since a reduction in the liquid level exposes more bitumen to the steam chamber. This interaction renders control of the drainage rate in reservoir simulations somewhat more challenging.

Oil Viscosity

The oil viscosity affects the loss of fluid potential in the near-wellbore region. It also influences the rate at which liquids drain from the steam chamber to the steam trap, as revealed by Equation 4.3. Butler (1997) has found that the viscosities of heavy oils from Canada, the United States, and South America are described reasonably well

by

$$\log_{10}\left[\log_{10}(\nu + 0.7)\right] = m \log_{10}(T + 273) + b \tag{4.4}$$

where ν is the kinematic viscosity in centistokes and T is the temperature in degrees Celsius. The coefficient m is given by

$$m = 0.3249 - 0.4106b \tag{4.5}$$

where b is an oil-specific constant.

For most of the reservoir simulations, the oil viscosity was calculated using Equations 4.4 and 4.5 with $b = 9$ (a median value for the heavy oils on which Equation 4.4 is based). To study the effect of the oil viscosity, several simulations were also run with oil viscosity data provided by the Firebag Resource Team at Suncor.

Reservoir Permeability

Like the oil viscosity, the reservoir permeability affects both the potential loss in the near-wellbore region and the rate at which liquid drains from the steam chamber. In addition, variations in the vertical-to-horizontal permeability ratio, $\frac{k_v}{k_h}$, are expected to alter the shape of the equipotentials in the steam trap.

The agreement between the GIPR and STARS was expected to be the most sensitive to variations in the $\frac{k_v}{k_h}$ ratio. Therefore, an initial suite of simulations was conducted assuming an isotropic reservoir, and then the simulations were rerun with $\frac{k_v}{k_h} = 0.5$ to confirm agreement between the models. This $\frac{k_v}{k_h}$ ratio was selected as representative of the Athabasca oil sands based on a high-level review of AER

performance presentations.

Thermal Conductivity of Solid-Fluid System

As shown by Equation 4.2, the thermal conductivity of the solid-fluid system influences whether heat transfer in the steam trap is conduction or convection dominated. In addition, the thermal conductivity affects the rate at which bitumen is mobilized in the steam chamber. The thermal conductivity of the solid-fluid system depends on the thermal conductivities of the sand and fluid phases, as well as the reservoir porosity and fluid saturations:

$$\kappa_m = \kappa_m(\kappa_s, \kappa_o, \kappa_w, \phi, S_w) \tag{4.6}$$

AER performance presentations for the Athabasca oil sands indicate that the reservoir porosity only varies between about 0.30 and 0.35. It was therefore controlled in the reservoir simulations. The fluid saturations in the steam trap, meanwhile, are complex functions of the reservoir properties, the fluid properties, and time, and are not readily manipulated or controlled. (In fact, Equation 3.41 reveals that the saturations depend on the oil-water relative permeability curves, fluid viscosities, and water cut.)

Of the phase conductivities, the greatest variability is expected in the sand conductivity. The thermal conductivity of sand is governed by its quartz content, as quartz has a higher conductivity than most other minerals (Butler 1997). The thermal conductivity of sand can be estimated using an equation adapted from Somerton et al. (1974):

$$\kappa_s = 2.86 + 4.85G \tag{4.7}$$

where κ_s is the thermal conductivity in W/(m·°C) and G is the volume fraction of quartz in the sand. The sand conductivity was manipulated in the reservoir simulations to study its effect on the steam trap temperature distribution.

Variables Summary

Table 4.1 summarizes the parameters considered during the design of the reservoir simulation case matrix. The table indicates whether each parameter was expected to vary significantly between SAGD projects, and whether each parameter was expected to have a significant effect on the agreement between the GIPR and STARS. Parameters that were expected to have both significant variability and significant influence were manipulated.

Table 4.1: Variables summary

Parameter	Significant Variability Expected	Significant Effect Expected	Variable Type
Steam Chamber-Production Well Pressure Difference	Y	Y	Manipulated
Pay Thickness	Y	Y	Manipulated
Oil Viscosity	Y	Y	Manipulated
Reservoir Permeability	Y	Y	Manipulated
Sand Thermal Conductivity	Y	Y	Manipulated
Sand Heat Capacity	N		Controlled
Steam Chamber Temperature		N	Controlled
Initial Reservoir Temperature	N		Controlled
Reservoir Porosity	N		Controlled
Initial Oil Saturation	N		Controlled
Oil Density	N		Controlled
Oil Thermal Conductivity	N		Controlled
Oil Heat Capacity	N		Controlled
Production Well Radius		N	Controlled

4.2.3 Case Matrix

Table 4.2 presents the case matrix for the reservoir simulations. Cases 1 to 4 and 11 to 14 represent a two-level, full factorial investigation of four of the five manipulated variables: the production well pressure, the pay thickness, the $\frac{k_v}{k_h}$ ratio, and the sand thermal conductivity. The pay thicknesses were selected based on a review of AER performance presentations. The sand thermal conductivities were calculated using Equation 4.7 for quartz volume fractions of 0 and 1. The effect of oil viscosity was investigated in a step-out simulation based on Case 3.

Table 4.2: Reservoir simulation case matrix

Case ID	Production Well Pressure	Sand Thermal Conductivity [W/(m·°C)]	Pay Thickness [m]	$\frac{k_v}{k_h}$	Oil Viscosity Source
1	Multiple	2.86	15	1	Butler (1997)
2	Multiple	7.71	15	1	Butler (1997)
3	Multiple	2.86	45	1	Butler (1997)
4	Multiple	7.71	45	1	Butler (1997)
11	Multiple	2.86	15	0.5	Butler (1997)
12	Multiple	7.71	15	0.5	Butler (1997)
13	Multiple	2.86	45	0.5	Butler (1997)
14	Multiple	7.71	45	0.5	Butler (1997)
23	Multiple	2.86	45	1	Firebag Resource Team

Note that the reservoir simulation cases were organized using a non-sequential numbering scheme. A case ID in the tens (e.g., 13) denotes permeability anisotropy; a case ID in the twenties (e.g., 23) indicates that the oil viscosity data was provided by the Firebag Resource Team. Thus, the pay thickness and sand thermal conductivity are consistent between cases with the same digit in the ones position (e.g., 3, 13, and 23). Note also that each case ID corresponds to multiple values for the production

well pressure because it was manipulated mid-simulation using the restart feature in STARS, as described in the next section.

4.2.4 Procedure

Each reservoir simulation case involved a baseline run, which included the start-up (circulation) and SAGD phases, plus multiple restart runs, in which the production well pressure was manipulated. The step-by-step simulation procedure was as follows:

1. Steam circulation was simulated for three months using the *heater well* feature in STARS. A temperature boundary condition of 228 °C was specified at the injection and production wells. Heating of the reservoir was assumed to occur by conduction only.

2. After three months, the well pair was converted from steam circulation to SAGD. A pressure of 2409 kPa (corresponding to a steam temperature of 222 °C) and steam quality of 95% were specified for the injection well. For the baseline simulation, a pressure of 2409 kPa was also specified for the production well, which was found to prevent both steam breakthrough and the excessive accumulation of liquid around the production well.

3. The results of the baseline simulation were reviewed to identify a period of stable production, which generally occurred after the steam chamber reached the overburden but before it coalesced with the steam chambers of the neighbouring well pairs.

4. The simulation was restarted during the period of stable production to study how the liquid level responds to changes in the production well pressure. The production well pressure was typically incremented or decremented by 10 kPa.

In some cases, smaller steps of 5 kPa were required to obtain the desired resolution in the liquid level data.

5. The data from each simulation (baseline and restarts) was used to define a set of stable operating conditions. The validity of the GIPR was assessed based on the consistency with which it and STARS predict the liquid level for the same conditions.

Even during periods of constant steam chamber height, the inflow rate and liquid level (among other outputs) were found to fluctuate slightly in STARS. Thus, it was not possible to define stable operating *points*. Instead, data from a 100 day period was used to define stable operating *windows*. The size of the operating windows was based on the minimum and maximum liquid levels observed over the 100 day period, adjusted for the uncertainty in the liquid level introduced by the vertical grid block size (roughly $\pm$ 6 cm with a vertical grid block size of 12.5 cm).

There were several efforts to reduce the magnitude of the fluctuations in the STARS outputs, including the refinement of the tolerances that control the automatic time stepping routine (see Section C.1 in Appendix C) and the refinement of the convergence tolerances for iterative calculations. These efforts were unsuccessful. Carlson (2006) has observed similar fluctuations that he attributes to steam injection instabilities arising from the low viscosity of steam and the high permeability of unconsolidated sands.

It should be noted that STARS includes a "steam trapping" mode whereby the simulator adjusts the pressure in the production well to maintain a user-specified subcool. This mode is popular for SAGD simulations because it replicates the control strategy employed by operators.

With the expectation that the liquid level would be a strong monotonic function

of the production well subcool, the reservoir simulations were initially run in the steam trapping mode. Certain subcool settings, however, unexpectedly caused the fluid interface to behave in an unstable manner, resulting in either steam breakthrough or injector flooding. Simulation results later obtained by manipulating the production well pressure reveal that the strength of the correlation between the subcool and the liquid level varies significantly from case to case. This finding has significant implications for SAGD process control strategies and is discussed further in Section 4.3.5.

4.2.5 Assumptions

Thermal Conductivity of Solid-Fluid System

STARS includes two models for calculating the effective thermal conductivity of solid-fluid systems. The first is a simple linear mixing model, whereby the individual conductivities of the solid and fluid phases are weighted by volume. The second is a nonlinear mixing model.[1] Figure 4.3 compares the linear and nonlinear mixing models for an oil-water-sand system, as exists in the steam trap, assuming a reservoir porosity of 0.32. The thermal conductivity for sand was calculated using Equation 4.7 for a quartz volume fraction of 0.5. The thermal conductivity for water corresponds to saturated liquid at 200 °C. The thermal conductivity for oil was calculated using the formula in Section 4.2.6.

With the linear mixing model, the effective thermal conductivity of the sand-fluid system is dominated by the sand conductivity and is relatively insensitive to variations in the fluid saturations. The effective thermal conductivity predicted by the nonlinear mixing model is significantly lower, increasing with water saturation (because the

[1]The documentation attributes the nonlinear mixing model to Anand et al. (1973), but a review of the equations suggests that the model is that of Krupiczka (1967) (cited in Somerton et al. 1974).

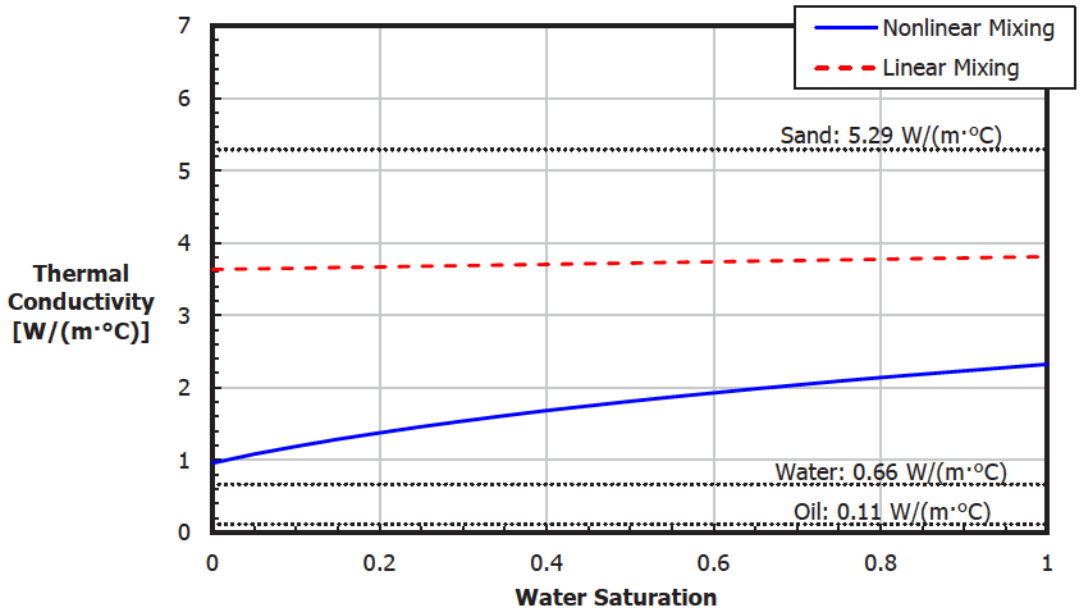

Figure 4.3: Comparison of linear mixing and nonlinear mixing conductivity models

conductivity of water is greater than that of oil). The nonlinear mixing model is believed to be more realistic than the linear mixing model and was used for the reservoir simulations.

Overburden and Underburden Heat Loss

Heat losses to the overburden and underburden were calculated using the semi-analytical infinite-overburden heat loss model in STARS. The model assumes one-dimensional (vertical) conduction in the overburden and underburden. Vinsome and Westerveld (1980) showed the model to be in good agreement with the exact solutions for some common heat transfer problems. The error resulting from neglecting horizontal heat transfer in the underburden is expected to be small because the vertical temperature gradient in the steam trap is expected to be significantly larger than the horizontal gradient.

Well Models

Conventionally, the grid blocks in reservoir simulations are significantly larger than the wells. Analytical equations called *well models* are used to relate the pressure in a well to the pressure in the grid block containing the well. In STARS, the flow rate of phase i out of (or into) a well is given by[2]

$$Q_i = I' \lambda_{ri} (P_{wf} - P) \tag{4.8}$$

where λ_{ri} is the relative mobility of phase i, P_{wf} is the wellbore flowing pressure, and P is the pressure in the grid block containing the well. For a fully screened well going through the centre of a grid block, the well index I' is given by

$$I' = \frac{2\pi l k}{\ln\left(\frac{R_e}{R_p}\right) + s} \tag{4.9}$$

where l is the grid block thickness in the well direction, R_e is the effective radius of the grid block containing the well, and R_p is the well radius. The effective grid block radius is calculated using the method developed by Peaceman (1983).

The well model is merely the equation for steady radial flow. As such, it is similar to the GIPR. For validation of the GIPR, the grid was refined significantly near the production well to minimize the area over which the well model was applied.

Capillary Pressure

As discussed in Section 3.1.5, the capillary pressure is often neglected in SAGD simulations because capillary effects are expected to be small in high-permeability

[2]Equations 4.8 and 4.9 are adapted from Computer Modelling Group Ltd. (2014). Some symbols have been modified to conform to the naming convention in this thesis. Symbols that appear only in these equations (e.g., I') are consistent with the source.

sands. For consistency with the existing body of simulation results and in the absence of capillary pressure data, the capillary pressure was set to zero in the reservoir simulations.

4.2.6 Inputs Summary

The reservoir simulation inputs are summarized in Tables 4.3 to 4.6.

Table 4.3: Reservoir properties

Parameter	Value	Source
Pay Thickness	Variable	-
Well Spacing	90 m (15 m pay) 160 m (45 m pay)	Suncor (2009)
Porosity	0.32	Suncor (2014)
Horizontal Permeability	4 D	Suncor (2014)
Vertical Permeability	Variable	-
Relative Permeability	Fig. 4.4 and 4.5	Based on Good et al. (1997)
Capillary Pressure	0	-
Density	2630 kg/m^3	Butler (1997) for sandstone
Thermal Conductivity	Variable	-
Heat Capacity [kJ/(kg·K), K]	0.73 kJ/(kg·K)	Cassis et al. (1985) for sandstone $C_p = 0.168 + 0.002442T - 1.611 \times 10^{-6}T^2$ $T = 283$ K
Initial Oil Saturation	0.85	Suncor (2014)
Initial Pressure	1500 kPa at production well	-
Initial Temperature	8 °C	Suncor (2014)

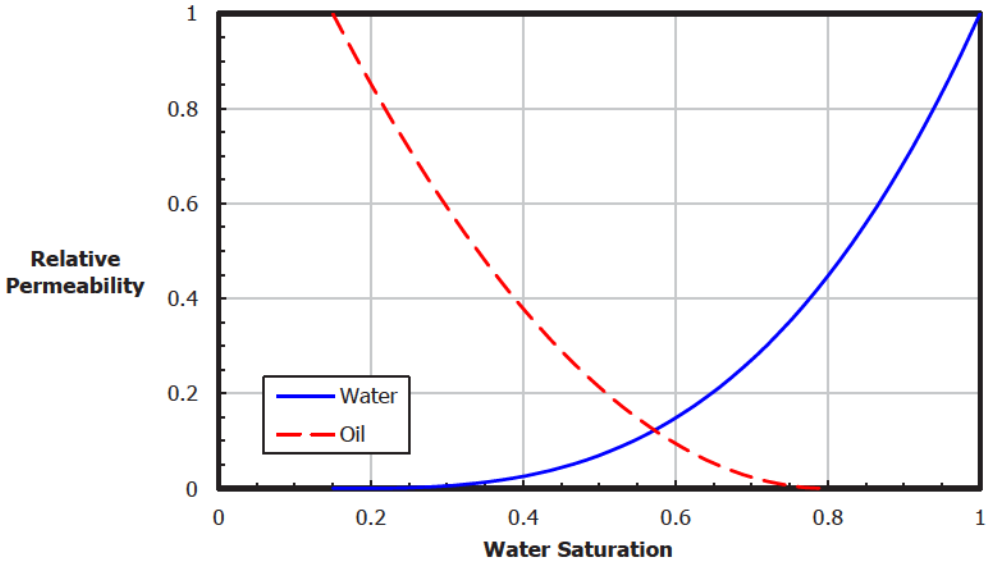

Figure 4.4: Oil-water relative permeability curves

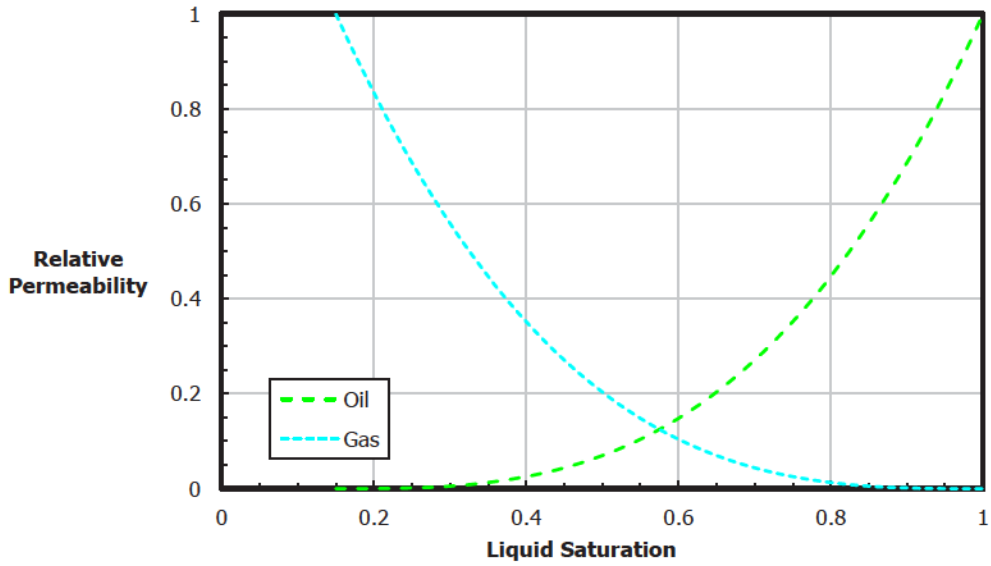

Figure 4.5: Gas-oil relative permeability curves

Table 4.4: Oil properties

Parameter	Value	Source
Density [kg/m^3, °C]	Temperature-dependent	Butler (1997) $\rho = \rho_{15}\left[1 - 0.06285\left(\frac{T-15}{100}\right) + 0.001426\left(\frac{T-15}{100}\right)^2\right]$ $\rho_{15} = \left(\frac{141.5}{131.5+°API}\right)(999)$ $°API = 8.1$
Viscosity [cSt, °C]	Temperature-dependent	Butler (1997) $\log_{10}\left[\log_{10}(\nu + 0.7)\right] = m\log_{10}(T + 273) + b$ $m = 0.3249 - 0.4106b$ $b = 9$
Thermal Conductivity [W/(m·°C), °C]	0.11 W/(m·°C)	Bland and Davidson (1967) (cited in Butler 1997) $\kappa_h = \frac{0.117}{d}(1 - 0.00054T)$ $d = \frac{141.5}{131.5+°API}$ $°API = 8.1$ $T = 10$ °C
Heat Capacity [kJ/(kg·°C), °C]	1.65 kJ/(kg·°C)	Butler (1997) based on Cassis et al. (1985) $c_o = 1.605 + 0.004361T - 4.046 \times 10^{-6}T^2$ $T = 10$ °C

Table 4.5: Overburden and underburden properties

Parameter	Value	Source
Density	Same as reservoir	-
Thermal Conductivity - Overburden	1.7 W/(m·°C)	Farouq Ali (1974) for wet shale (cited in Butler 1997)
Thermal Conductivity - Underburden	3.5 W/(m·°C)	Farouq Ali (1974) for wet limestone (cited in Butler 1997)
Heat Capacity	Same as reservoir	-
Initial Temperature	Same as reservoir	-

Table 4.6: Well properties

Parameter	Value	Source
Injector Size	244 mm	Suncor (2014)
Injector Skin Factor	0	-
Injector Temperature (Circulation)	228 °C (T_{sat} at 2700 kPa)	Firebag Resource Team
Injector Temperature (SAGD)	222 °C (T_{sat} at 2400 kPa)	Firebag Resource Team
Injector Steam Quality (SAGD)	95% (wellhead estimate)	Firebag Resource Team
Producer Size	244 mm	Suncor (2014)
Producer Skin Factor	0	-
Producer Temperature (Circulation)	228 °C (T_{sat} at 2700 kPa)	Firebag Resource Team
Producer Pressure (SAGD)	Variable	-
Circulation Duration	3 months	Firebag Resource Team
Vertical Interwell Spacing	5 m	-
Vertical Spacing between Producer and Underburden	5 m	Firebag Resource Team

4.3 Reservoir Simulation Results

4.3.1 Sample Data

This section presents detailed results for Case 1 to provide a sample of the reservoir simulator output and to demonstrate the simulation procedure. Detailed results for the other cases are presented in Appendix A in Figures A.1 to A.24.

Figure 4.6 shows the inflow rate predicted by STARS for the baseline simulation. Because the reservoir model is two-dimensional, the inflow rate is reported on a specific (per-unit-well-length) basis. Production begins at 90 days, when the well pair is converted to SAGD, and increases rapidly as the steam chamber grows upwards from the injection well. The inflow rate plateaus when the steam chamber reaches the overburden, and production is nearly constant as the steam chamber grows laterally. After approximately 1000 days, the steam chamber coalesces with the steam chambers above the neighbouring well pairs, and the inflow rate begins to decline.

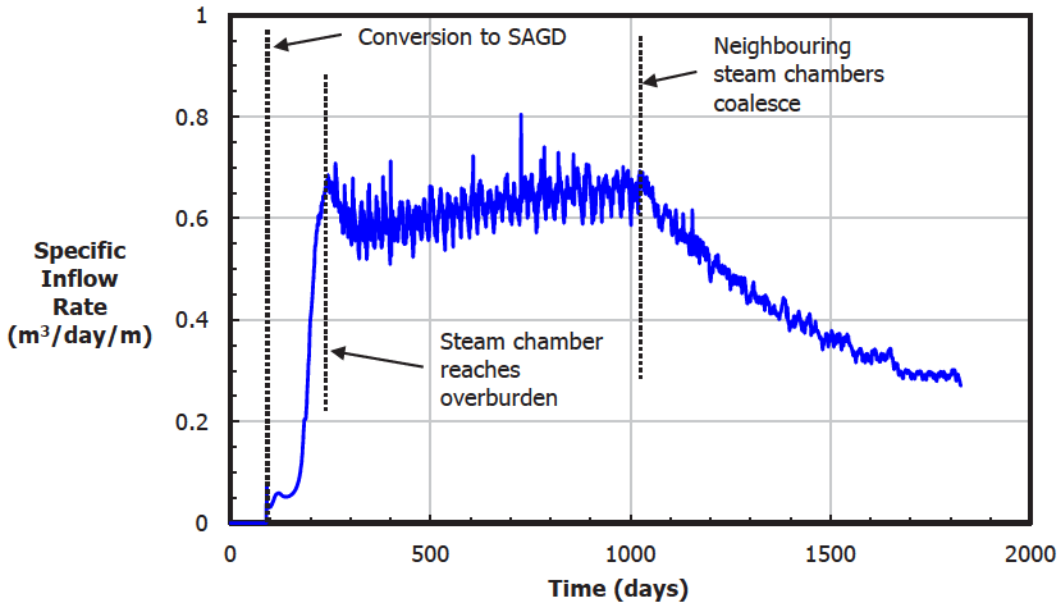

Figure 4.6: Specific inflow rate for Case 1 baseline

The liquid level and inflow temperature for the baseline simulation are shown in Figure 4.7. For the first few months of SAGD, the steam chamber develops only above the injection well; the fluid interface has not yet established itself between the injection and production wells. As the steam chamber matures and the inflow rate stabilizes, the fluid interface moves to an equilibrium position just above the production well. The liquid level is nearly constant during the period of lateral steam chamber growth and decreases slightly after steam chamber coalescence, likely in response to the decreasing inflow rate. The discrete steps in the liquid level correspond to the vertical size of the grid blocks (12.5 cm).

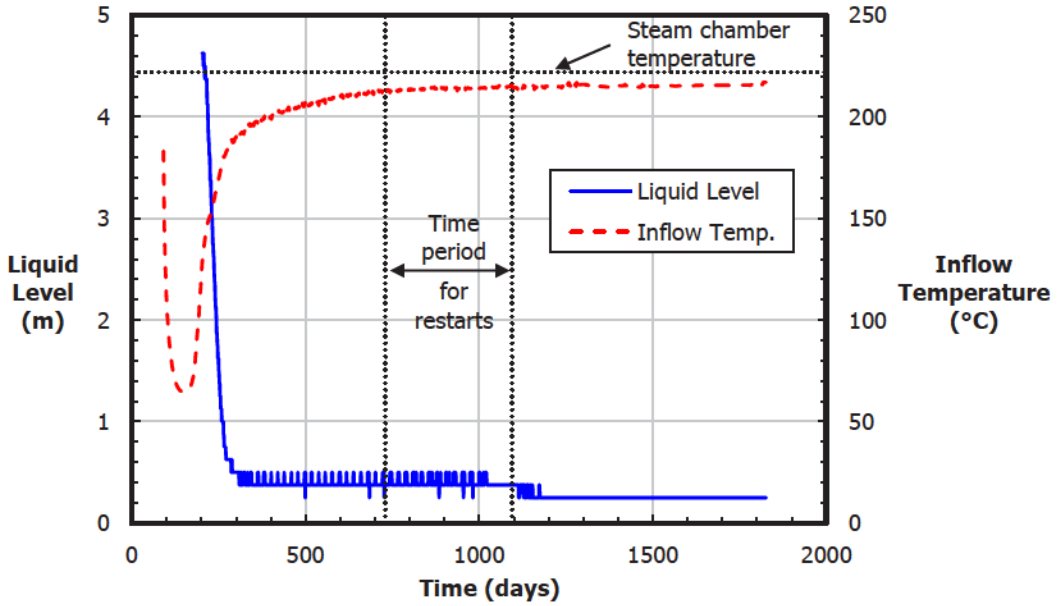

Figure 4.7: Liquid level and inflow temperature for Case 1 baseline

The inflow temperature is initially high as the fluids near the well pair (which were heated during circulation) drain, but it decreases rapidly as fluids that were farther from the well pair (and, hence, cooler) are produced. As the steam chamber develops, the inflow temperature climbs once more and approaches the steam chamber temperature (222 °C). Even after the steam chamber is well-established, there is a

gradual increase in the inflow temperature over time. This increase appears to be related to the angle of the steam chamber walls and is discussed in Section 4.3.5.

The baseline simulation was restarted at two years, during the period of lateral steam chamber growth and fairly stable production, to study the effect of the production well pressure on the liquid level. The pressure in the production well was increased from 2409 kPa in 10 kPa increments to 2419, 2429, and 2439 kPa. Figure 4.8 shows that the fluid interface rises rapidly to a new equilibrium position in response to an increase in the production well pressure, confirming that such responses occur on a relatively short timescale.

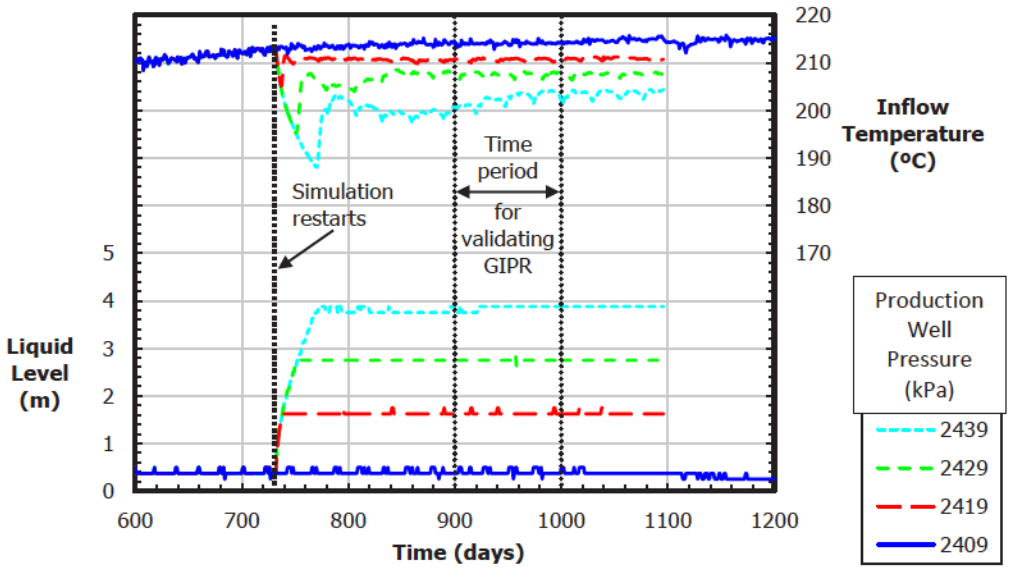

Figure 4.8: Effect of well pressure on liquid level and inflow temperature for Case 1

Each 10 kPa increment in the production well pressure causes the liquid level to rise by about 1 m. This is essentially the hydrostatic response and will be shown to be characteristic of gravity-dominated systems. There is a negative correlation between the liquid level and the inflow temperature; however, the strength of this correlation was found to vary significantly between the cases and is discussed further in Section 4.3.5. Sets of stable operating conditions were defined based on the simulation

results from 900 to 1000 days and used to assess the validity of the GIPR.

4.3.2 Isotropic Permeability

The stable operating windows predicted by STARS for Cases 1 and 3 are shown in Figure 4.9. In both cases, the reservoir was assumed to be isotropic with a permeability of 4 D and the conductivity of the sand was assumed to be 2.86 W/(m·°C). In Case 1, the pay thickness was 15 m; in Case 3, the pay thickness was 45 m, giving higher inflow rates. As discussed in Section 4.2.4, the height of an operating window is defined by the minimum and maximum liquid levels in a 100 day period, adjusted for the uncertainty in the liquid level associated with the vertical grid block size. The width of an operating window is based on the minimum and maximum specific inflow rates in the same period. Figure 4.9 also shows the liquid level predicted by the GIPR for each set of stable operating conditions. The error bars on the GIPR predictions convey the uncertainty arising from fluctuations in the STARS data.

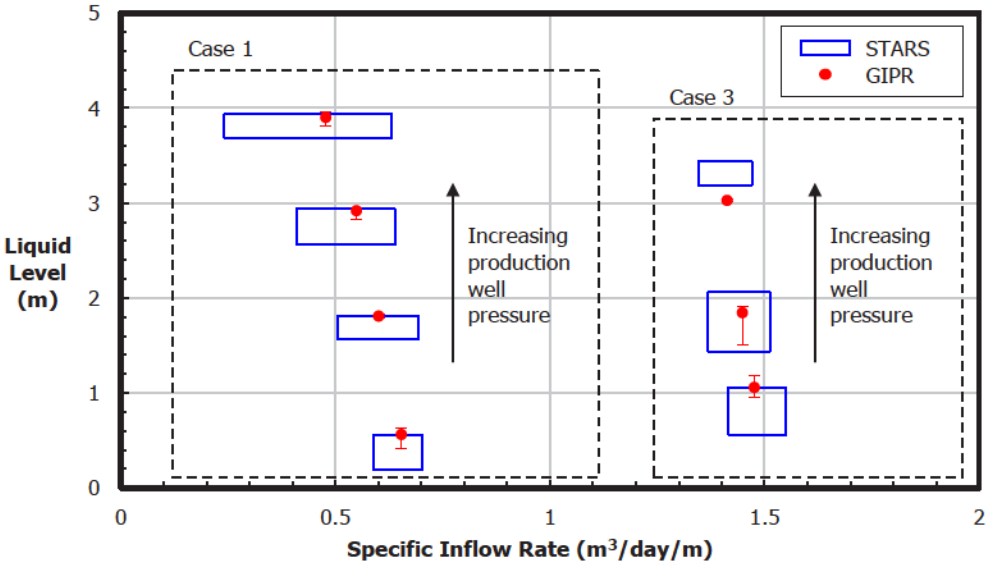

Figure 4.9: Comparison of liquid levels from STARS and GIPR for Cases 1 and 3

Agreement between the GIPR and STARS is generally good. The liquid levels predicted by the two models agree within uncertainty for all but one set of operating conditions. For Case 1, the liquid level predicted by the GIPR is consistently at the high end of the liquid level range from STARS, but this trend is not evident in the results for Case 3. For Case 1, the magnitude of the inflow rate fluctuations increases significantly as the production well pressure is increased. The fluctuations appear to be periodic variations akin to slugging, but their cause is uncertain. Despite the large fluctuations in the inflow rate, the fluctuations in the liquid level (from both STARS and the GIPR) remain relatively small.

Inspection of the pressure distribution in the steam trap provides insight into the trends in the modelling results. Figure 4.10 shows the pressure along a vertical line between the production and injection wells for a single Case 1 time step. The results for the baseline and restart simulations are shown side by side. The STARS data shows the pressure above and below the fluid interface, which appears as a sharp elbow, while the GIPR predicts only the pressure below the fluid interface.

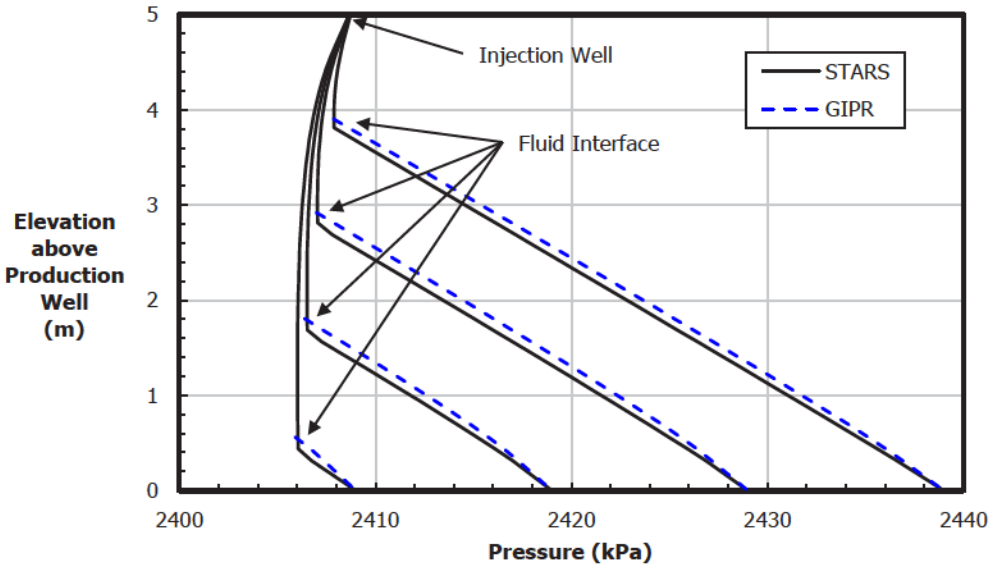

Figure 4.10: Comparison of pressure profiles from STARS and GIPR for Case 1

The near-linear pressure distributions in the steam trap indicate that the flow is gravity dominated; the slope of the pressure profiles is essentially the hydrostatic pressure gradient. The GIPR predicts slightly more potential loss in the near-wellbore region than STARS, which leads to curvature of the pressure distributions and slightly higher liquid level estimates. This discrepancy appears to stem from non-axisymmetry in the velocity distributions predicted by STARS. Figure 4.11 compares the speeds of the water and oil phases for Case 1 with a production well pressure of 2429 kPa (note that the speed scales differ by a factor of ten). The water and oil phases are largely segregated, with the flow of water concentrated at the top of the production well, and the flow of oil concentrated at the sides.

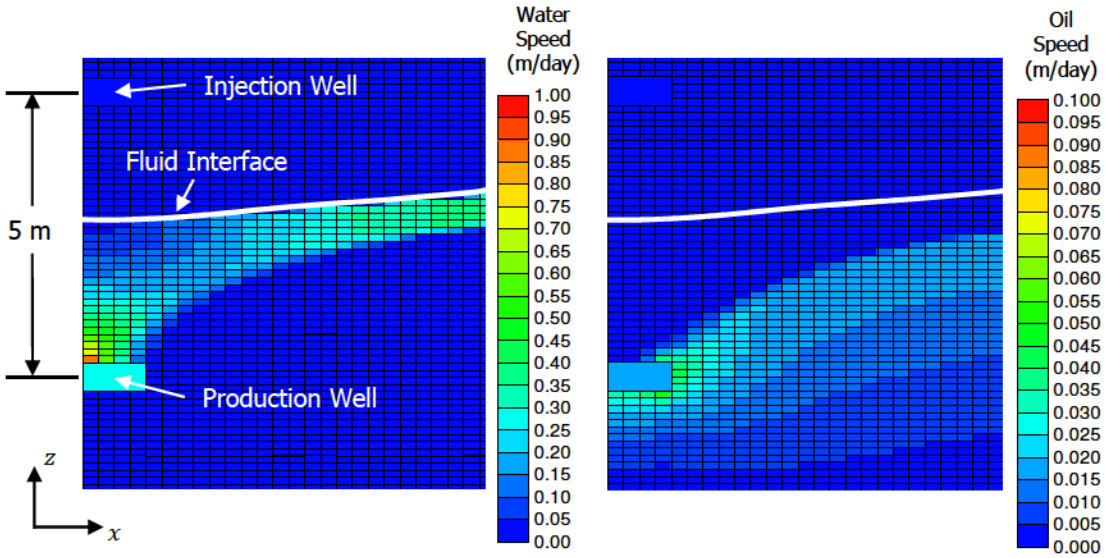

Figure 4.11: Fluid speeds for Case 1 with $P_p = 2429$ kPa

The steam trap pressure distributions for a Case 3 time step are shown in Figure 4.12. Due to higher inflow rates, the potential loss in the near-wellbore region is significantly greater for Case 3 than for Case 1, leading to significantly greater curvature in the pressure profiles. Again, the discrepancy between the GIPR and STARS appears to stem from non-axisymmetry in the velocity distributions

predicted by STARS. The water and oil phases are somewhat segregated, but less so than in Case 1. It is speculated that the degree of segregation between the water and oil phases depends on the angle of the steam chamber walls, which are steeper in Case 3 than in Case 1 (due to the greater pay thickness). In addition, there is some tendency for the flow to concentrate at the top of the production well as the liquid level rises, as depicted in Figures 4.13 and 4.14.

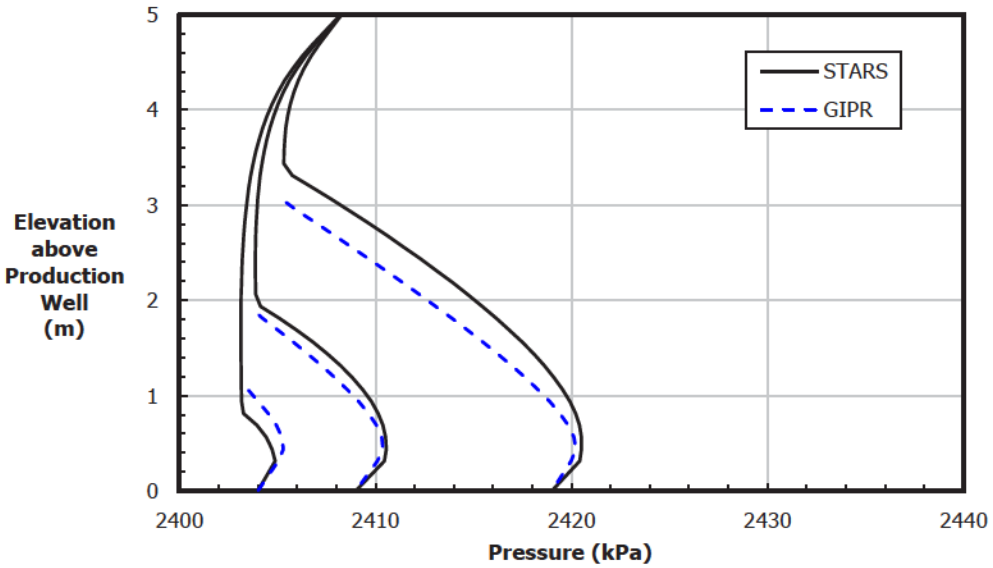

Figure 4.12: Comparison of pressure profiles from STARS and GIPR for Case 3

The agreement between the GIPR and STARS shows little sensitivity to the thermal conductivity of the sand or the oil viscosity data. The liquid levels from the GIPR and STARS for Cases 2, 4, and 23 are compared in Section A.9 of Appendix A.

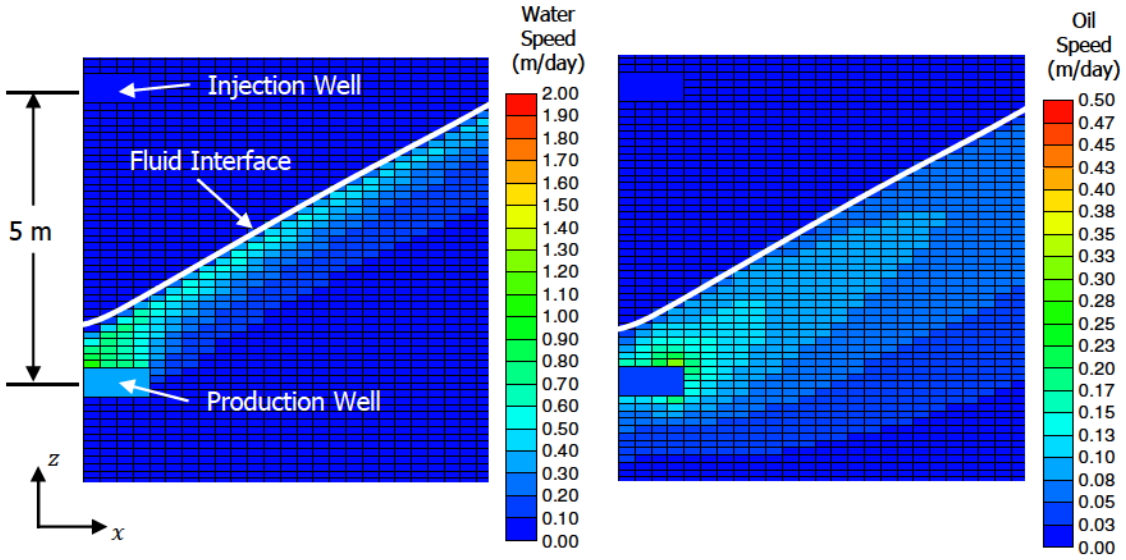

Figure 4.13: Fluid speeds for Case 3 with $P_p = 2404$ kPa

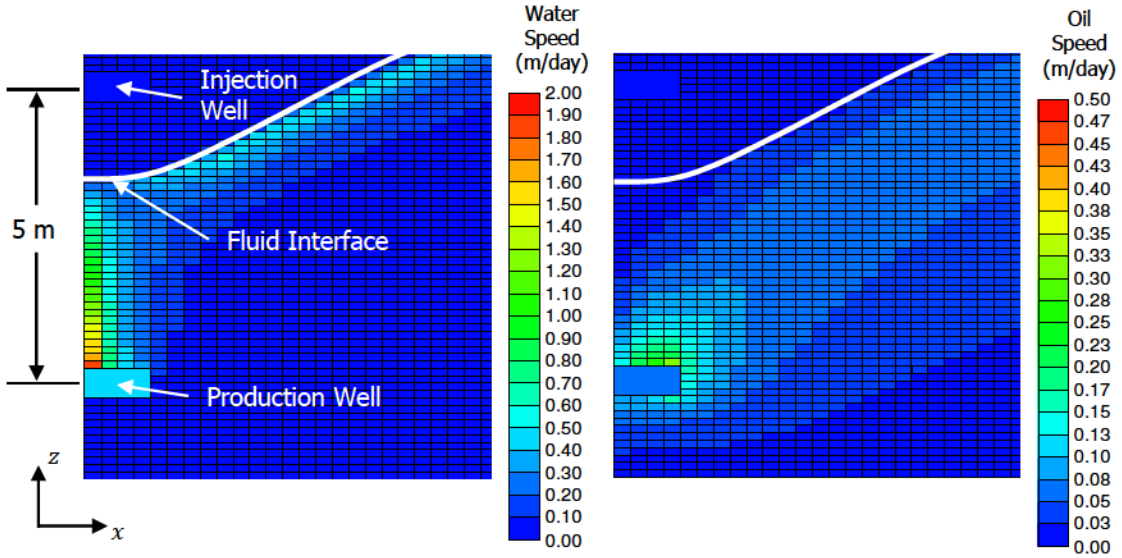

Figure 4.14: Fluid speeds for Case 3 with $P_p = 2419$ kPa

4.3.3 Anisotropic Permeability

The stable operating windows from STARS for Cases 11 and 13 are shown in Figure 4.15, along with the liquid levels predicted by the GIPR. In both cases, the reservoir was assumed to be anisotropic with a horizontal permeability of 4 D and vertical permeability of 2 D. In Case 11, the pay thickness was 15 m; in Case 13, the pay thickness was 45 m. Both cases assumed a thermal conductivity of 2.86 W/(m·°C) for sand.

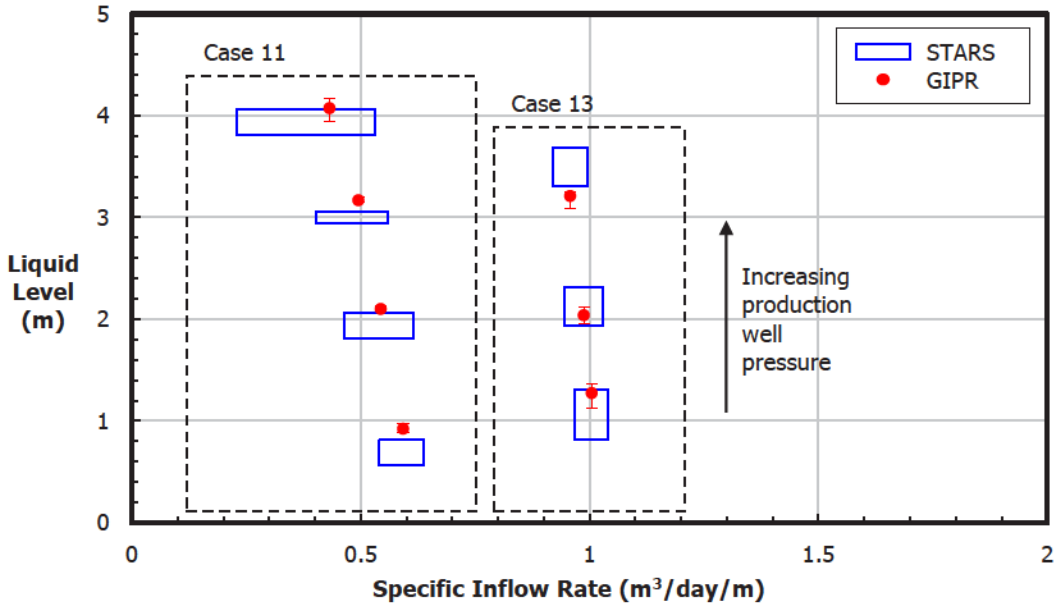

Figure 4.15: Liquid levels from STARS and GIPR for Cases 11 and 13

Once again, the agreement between the GIPR and STARS is generally good, indicating that the modelling basis accurately accounts for permeability anisotropy. The trends for Case 11 are similar to those for Case 1, with the liquid level from the GIPR falling consistently at the high end (or just outside) of the liquid level range from STARS. As before, inspection of the velocity distributions suggests that this discrepancy stems from segregation of the water and oil phases in the reservoir simulations.

Comparing Figures 4.9 and 4.15, a trend is also apparent in the results for Cases 3 and 13. When the fluid interface is close to the production well, the GIPR tends to predict a higher liquid level than STARS. Conversely, when the fluid interface is close to the injection well, the GIPR generally predicts a lower liquid level than STARS. This trend is believed to arise from the tendency for the flow to collect above the production well as the liquid level rises. The greater the flow velocity above the production well, the higher the potential loss, and the higher the liquid level required to overcome the loss.

As for the cases with isotropic permeability, the agreement between the GIPR and STARS shows little sensitivity to the thermal conductivity of the sand in cases with anisotropic permeability. The liquid levels from the GIPR and STARS for Cases 12 and 14, in which the sand thermal conductivity was increased to 7.71 W/(m·°C), are compared in Section A.9 of Appendix A.

4.3.4 Correction Factor

Figure 4.16 summarizes the reservoir simulation results. Each point shows the time-averaged liquid level for a specific set of stable operating conditions. The liquid level from STARS is read off of the x-axis, while the liquid level from the GIPR is read off of the y-axis. When a point falls along the 45° line shown in black, it denotes perfect agreement between the two models. The colours of the points indicate the pay thickness and oil viscosity assumptions (refer to the figure legend). Circles denote cases in which the reservoir permeability was assumed to be isotropic; squares denote permeability anisotropy.

The trends identified in the preceding sections are apparent in the time-averaged data. Most notably, for the cases with a pay thickness of 45 m, the GIPR tends to

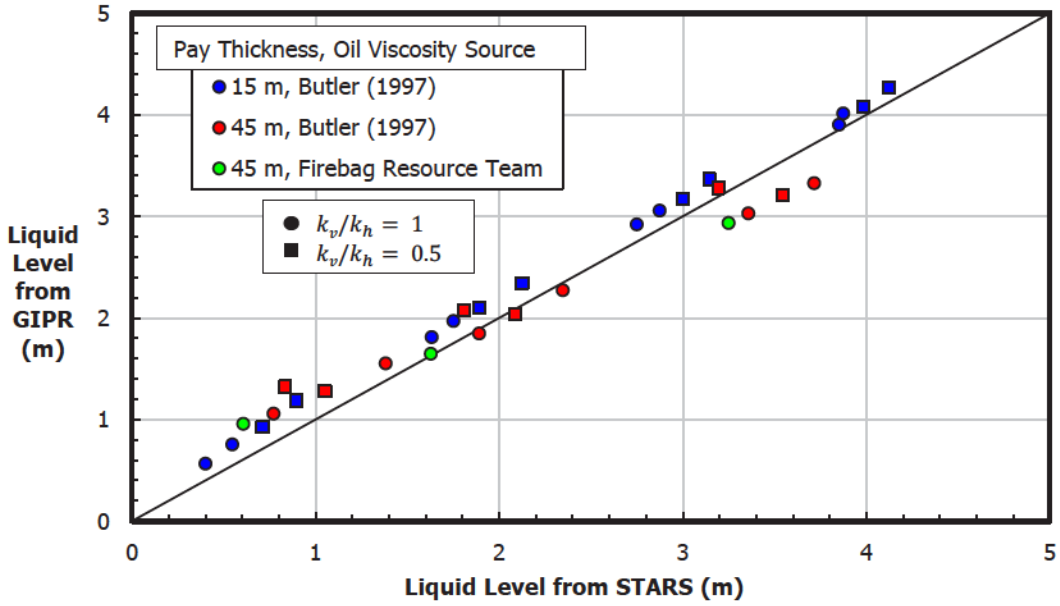

Figure 4.16: Agreement between GIPR and STARS without correction

overestimate the liquid level when the fluid interface is close to the production well, and underestimate the liquid level when the fluid interface is close to the injector.

To attempt to improve the agreement between the GIPR and STARS, a correction factor, $C(h)$, was introduced in the GIPR to yield

$$P_{sc} - P_p + \rho(T_p)gh = \frac{C(h)\mu_a(T_p)q}{2\pi\sqrt{k_h k_v}} \left\{ \ln \left[\frac{\left(\frac{k_h}{k_v}\right)^{\frac{1}{4}} h}{R_p} \right] + s \right\} \tag{4.10}$$

The aim of the correction factor is to attenuate the potential loss when the liquid level is low, when the flow is concentrated at the sides of the production well, and to amplify the potential loss when the liquid level is high, when the flow is concentrated at the top of the production well. In simpler terms, the correction factor captures non-axisymmetry in the inflow distribution; it modifies the GIPR, which was derived assuming axisymmetric flow, based on the conditions *above* the production well, which ultimately govern the position of the fluid interface.

The following correction factor was found to improve the agreement between the GIPR and STARS:

$$C(h) = 0.100h + 0.758 \tag{4.11}$$

where h is the liquid level in metres. With Equation 4.11, the potential loss is about 75% of the uncorrected value at very low liquid levels, and about 125% of the uncorrected value at liquid levels approaching 5 m (the typical spacing between the injection and production wells). Figure 4.17 shows the effect of the correction factor on the modelling results. The agreement between the GIPR and STARS is noticeably improved for the cases with a pay thickness of 45 m. For the cases with a pay thickness of 15 m, the liquid levels are largely unaffected because those cases are gravity dominated. Overall, a modest reduction in the root-mean-square deviation (RMSD) between the GIPR and STARS, from 0.23 m to 0.17 m, is achieved.

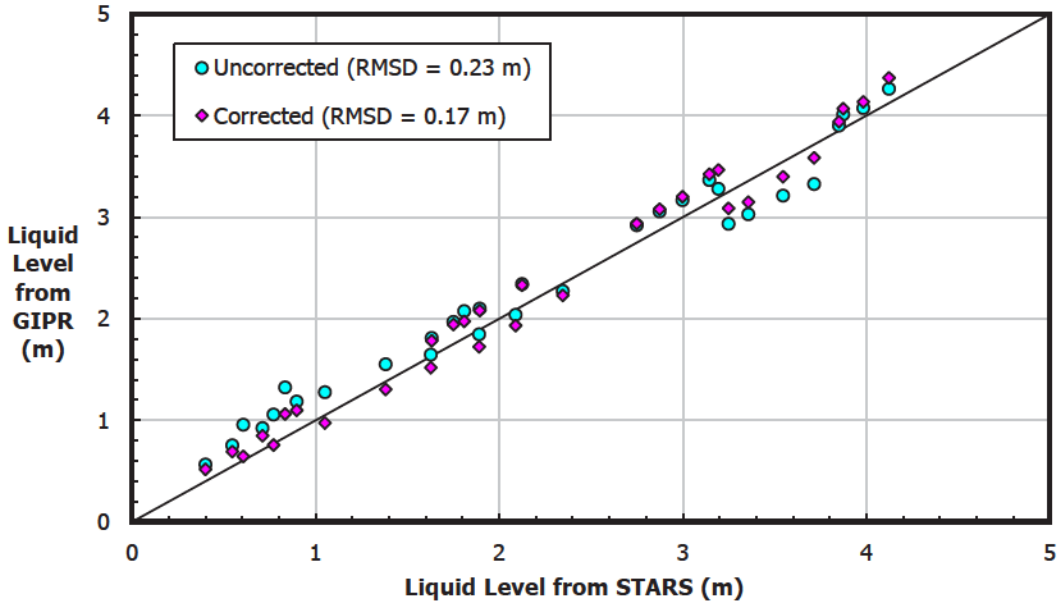

Figure 4.17: Agreement between GIPR and STARS with correction factor

4.3.5 Inflow Temperature

In some cases, it may be possible to determine the inflow temperature, T_p, from simulator or field data, enabling accurate calculation of the fluid viscosities and densities. Such data is not always available, however, and so knowledge of how the inflow temperature varies with other parameters is desirable. There is a rule of thumb in the SAGD industry that the subcool in the production well increases by about 10 °C for every metre of liquid level (Yuan and Nugent 2013), but the validity of this rule is uncertain.

To gain a better understanding of the temperature trends, the difference between the steam chamber temperature and the inflow temperature was plotted against the liquid level for each reservoir simulation to yield Figure 4.18. This temperature difference is effectively equal to the subcool in the production well, provided the pressure difference between the steam chamber and the production well is reasonably small so that the change in the steam saturation temperature is negligible.

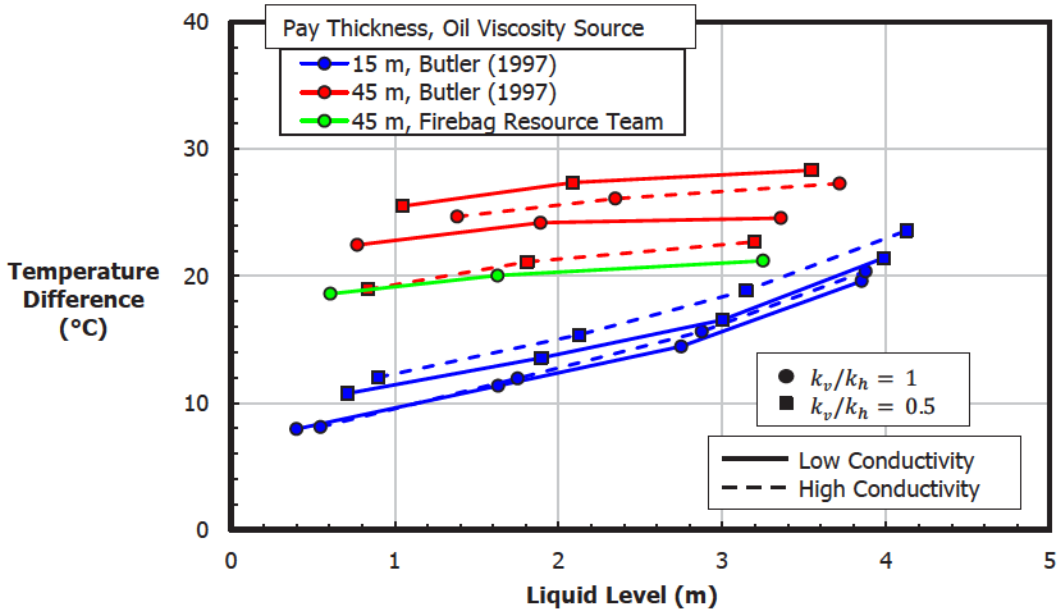

Figure 4.18: Variation of temperature difference with liquid level

The figure reveals several nonintuitive trends. First, the temperature difference is larger for cases with a pay thickness of 45 m than for cases with a pay thickness of 15 m. It ranges from approximately 20 °C to 30 °C with 45 m of pay, and from approximately 10 °C to 20 °C with 15 m of pay. This offset appears to result from a long-timescale increase in the inflow temperature that correlates well with the angle of the steam chamber walls. During the period of lateral steam chamber growth and relatively stable production, when the temperature data was collected, the steam chamber walls are significantly steeper with 45 m of pay than with 15 m of pay (owing simply to the reservoir geometry). It is speculated that the temperature offset would be diminished if the data were collected at times in the simulations with a consistent steam chamber angle. Edmunds (2000) has also noted the influence of the steam chamber angle on the inflow temperature.

Second, the temperature difference is more sensitive to the liquid level in the cases with a pay thickness of 15 m than in the cases with a pay thickness of 45 m. The inflow rates appear to be sufficiently higher with 45 m of pay that the heat transfer in the steam trap is convection dominated; the inflow temperature is governed by the temperature of the liquids draining down the steam chamber walls. With 15 m of pay, the inflow rates are much lower and conduction plays a more significant role (although the increase in the temperature difference with the liquid level is a far cry from the 10 °C/m rule of thumb). Unexpectedly, the temperature data appears largely insensitive to the thermal conductivity of the sand. It is possible that the nonlinear mixing model for thermal conductivity blunts the effect of the sand conductivity, which would otherwise dominate the conductivity of the oil-water-sand system.

Finally, the temperature difference does not tend to zero at low liquid levels. Given the significant role of convection in the cases considered, the inflow temperature appears to be less an indicator of the liquid level, and more an indicator of the

average temperature of the fluid entering the production well. As such, the inflow temperature may be less than the steam chamber temperature even when steam is drawn into the top of the production well, provided there is cooler fluid entering the sides and bottom of the well. This result challenges the practice of inferring the liquid level from temperature measurements in the production well – or at least the notion that maintaining a subcool in the producer guarantees a liquid level – but it corroborates the findings of other researchers. For example, Ito and Suzuki (1999) have observed the inflow of steam in simulations where the production well was maintained at subcooled conditions. They note that the temperature of the liquids draining down the steam chamber walls was approximately 40 °C less than the steam chamber temperature, such that the specification of a subcool of less than 40 °C required steam to be drawn near or into the production well to heat the draining liquids.

In light of these temperature trends, the best strategy for estimating the inflow temperature in the GIPR appears to be case specific. In cases with high inflow rates, when the heat transfer in the steam trap is convection dominated, it seems appropriate to assume a constant or near-constant inflow temperature. In cases with low inflow rates, however, it appears more appropriate to couple the inflow temperature to the liquid level (but it cannot be assumed that the inflow temperature tends to the steam chamber temperature at low liquid levels). The heat transfer in the steam trap warrants further research.

Chapter 5

Case Studies

This chapter presents the findings of case studies conducted to investigate the uniformity and stability of the fluid interface along the length of a SAGD well pair. The case studies examine three challenges to steam trap control: (1) variable pay thickness, (2) non-uniform reservoir permeability, and (3) an inclined production well trajectory. The chapter begins with a description of the approach for extending the GIPR to three dimensions, along with a discussion of the uniqueness and stability of GIPR solutions.

5.1 Approach

In general, the parameters that appear in the GIPR – in particular, the production well pressure, the inflow rate, and the reservoir permeability – vary along the length of a SAGD well pair. As a result, the position of the fluid interface is not uniform, but varies according to the local conditions. To investigate the variability in the fluid interface position, three case studies were conducted using a three-dimensional model that incorporates the GIPR. The analysis approach is unique because the model

domain is limited to the production well and the surrounding steam trap. Instead of predicting the pressure and drainage rate in the steam chamber, the model receives the steam chamber conditions as input and returns the liquid level distribution along the well pair.

The case studies were designed to explore three different challenges to steam trap control: (1) variable pay thickness, (2) non-uniform reservoir permeability, and (3) an inclined production well trajectory. Each case study began with an evaluation of the performance of conventional completion designs for the production well. Then, the completion design was modified to improve the uniformity of the fluid interface and reduce the risk of steam trap failure.

5.1.1 Extension of the GIPR to Three Dimensions

Within the steam trap, there are two paths by which fluid may flow parallel to the axis of the production well: through the reservoir and through the production well itself. The relative significance of these two flow paths may be assessed by comparing their *flow resistance*, a hydraulic concept analogous to electrical resistance where pressure difference takes the place of voltage and flow rate takes the place of current. To facilitate the comparison, single-phase flow is assumed through the reservoir and laminar flow is considered in the production well. These assumptions lead to low-end estimates for the flow resistance through the two paths, since relative permeability effects in the reservoir and turbulence in the wellbore tend to increase flow resistance, but they permit an order-of-magnitude comparison.

With these simplifications, the axial flow through the near-wellbore reservoir is

governed by Darcy's law for single-phase flow:

$$Q = \frac{kA}{\mu}\frac{\Delta P}{L} \tag{5.1}$$

where Q is the volumetric flow rate, k is the reservoir permeability, A is the flow area, μ is the fluid viscosity, ΔP is the pressure loss, and L is the length over which the pressure loss occurs. The flow resistance is the pressure loss per unit of flow rate:

$$\Omega_r = \frac{\mu L}{kA} \tag{5.2}$$

The flow through the production well is governed by the Hagen-Poiseuille equation for laminar flow:

$$Q = \frac{\Delta P \pi {D_p}^4}{128 \mu L} \tag{5.3}$$

and

$$\Omega_p = \frac{128 \mu L}{\pi {D_p}^4} \tag{5.4}$$

The ratio of the flow resistance through the near-wellbore reservoir to the flow resistance through the production well is thus

$$\frac{\Omega_r}{\Omega_p} = \frac{\pi {D_p}^4}{128 k A} \tag{5.5}$$

A typical production well diameter is 219 mm (8 5/8 inches), and a typical permeability for high-quality sand is 6 D. It is comparatively difficult to quantify the axial flow area in the near-wellbore reservoir. Indeed, the flow through the reservoir

is not purely axial. For the purpose of this comparison, however, a flow area on the order of 10 m^2 is assumed. Substituting these values into Equation 5.5 gives a ratio of about 10^6 - the flow resistance through the near-wellbore reservoir is orders higher than the flow resistance through the wellbore itself. Thus, the production well is the primary conduit for axial flow in the steam trap.

On the basis that the axial flow through the near-wellbore reservoir is negligible, the two-dimensional GIPR was coupled to a wellbore hydraulics model to extend the analysis approach to three dimensions. The production well was discretized into segments 10 m in length, and GIPR "elements" were attached at the junctions between segments, yielding a hydraulic network like the one shown in Figure 5.1. Because the focus of the case studies was the fluid interface, the model domain was limited to the productive well length (i.e., the riser section was not modelled). The steam chamber pressure, P_{sc}, and drainage rate, q_{sc}, were specified as boundary conditions at the fluid interface. To obtain a unique liquid level distribution, it was also necessary to specify the production well pressure, P_p, at one location in the wellbore.

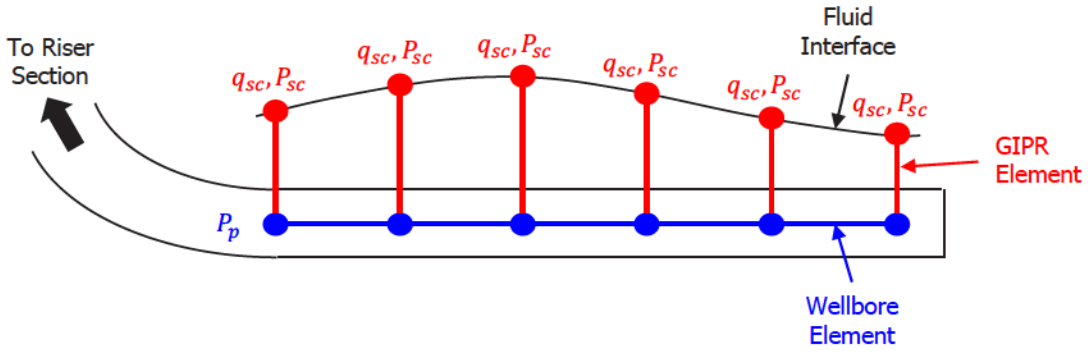

Figure 5.1: Hydraulic network and boundary conditions

Note that little distinction was made between the terms *drainage rate* and *inflow rate* in the previous chapters. In this chapter, *drainage rate* will be used to refer to the

rate at which liquid drains from the steam chamber to the steam trap, while *inflow rate* will be used to refer to the flow rate into the production well. At steady-state conditions, the inflow rate equals the drainage rate and the liquid level is static. It will be shown, however, that – under certain conditions – there may be no liquid level at which the inflow rate predicted by the GIPR would match the prescribed drainage rate. The nonexistence of a GIPR solution indicates that the prescribed drainage rate would not be sustainable.

Note also that the steam chamber pressure is assumed to be uniform in the subsequent case studies. Some authors have suggested that the steam chamber pressure reflects the pressure gradient along the injection well (Edmunds and Gittins 1993; Edmunds 2000); however, the extent to which the steam chamber pressure varies is disputed in the literature. A uniform steam chamber pressure may be considered representative of a well-designed injection well with minimal pressure gradient. Further research is recommended to investigate the uniformity of the steam chamber pressure and the influence of the injection well on the fluid interface position.

5.1.2 Wellbore Hydraulics Model

The pressure distribution in the production well was predicted using FloNet, a wellbore hydraulics model developed by Noetic Engineering 2008 Inc. The model assumes that the production fluid is a homogeneous mixture of oil and water and calculates the mixture viscosity based on the water cut. The model selects from three flow regimes based on the Reynolds number:

$$Re = \frac{\rho u D_p}{\mu} \tag{5.6}$$

where ρ is the mixture density, u is the average flow velocity, D_p is the production well diameter, and μ is the mixture viscosity. The flow is treated as laminar for $Re < 2000$, turbulent for $Re > 3000$, and transitional for $2000 < Re < 3000$. The friction loss for laminar flow is determined from the Hagen-Poiseuille equation, while the friction factor for turbulent flow is calculated using the Colebrook equation (see Cengel and Cimbala 2006). The friction factor for transitional flow is linearly interpolated from the friction factors for laminar and turbulent flow based on the Reynolds number. The model accounts for both friction loss and gravity, and so it is well-suited to analyzing the flow through production wells with inclined trajectories, in which gravity can play a significant role.

A tubing string is often extended to the toe of SAGD production wells, creating two axial flow paths in the wellbore – one through the tubing string, and another through the annulus between the tubing string and the slotted liner. Both flow paths can be included in the wellbore model, along with connections between the flow paths (as would be created, for example, by drilling ports in the tubing string). Because the tubing string is not typically centralized in the slotted liner, the annulus between the tubing and the liner is generally eccentric. The wellbore model includes a geometry factor in the calculation of the friction factor for eccentric annuli, following the method described by Brill and Mukherjee (1999).

5.1.3 Uniqueness and Stability of GIPR Solutions

Prediction of the fluid interface position along the length of a well pair is complicated by the non-uniqueness of solutions to the GIPR. For a given pressure difference between the steam chamber and the production well, there may be multiple liquid levels at which the inflow rate would match the specified drainage rate. This is illustrated in Figure 5.2, which shows the characteristic relationship between the inflow rate and the liquid level when the production well pressure is less than or equal to the steam chamber pressure. There are two liquid levels, h_1 and h_2, at which the specified drainage rate, q_{sc}, would be sustained.

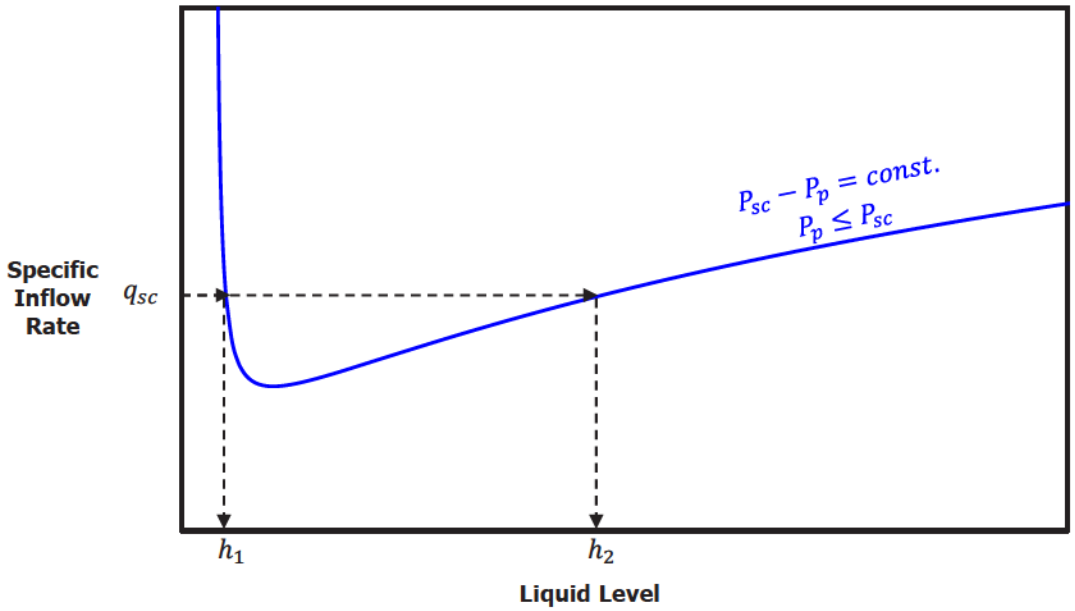

Figure 5.2: Non-uniqueness of GIPR solutions

Solutions h_1 and h_2 may be reduced to a single solution by considering the stability of the fluid interface. From Figure 5.2, it is apparent that the liquid level and the inflow rate are positively correlated near h_2. Solution h_2 can be said to be *stable*. A positive perturbation to the liquid level would cause an increase in the inflow rate, which would pull the liquid level back to its equilibrium position. Likewise, a negative

perturbation to the liquid level would cause a reduction in the inflow rate, which would allow the liquid level to climb back to its equilibrium position. By contrast, the liquid level and the inflow rate are negatively correlated near h_1. Solution h_1 can be said to be *unstable*. Any perturbation to the liquid level would unsettle the system, and so solution h_1 must be discarded.

Unique solutions to the GIPR may thus be obtained by discarding unstable ones. A mathematical criterion for the stability of the fluid interface may be formulated by noting that transitions to instability occur where $\partial(P_{sc} - P_p)/\partial h = 0$. Returning to Equation 4.10, an expression for $P_{sc} - P_p$ is obtained by rearranging the variables:

$$P_{sc} - P_p = \frac{C(h)\mu_a q}{2\pi\sqrt{k_h k_v}} \left\{ \ln \left[\frac{\left(\frac{k_h}{k_v}\right)^{\frac{1}{4}} h}{R_p} \right] + s \right\} - \rho g h \tag{5.7}$$

If the correction factor, $C(h)$, and the apparent fluid viscosity, μ_a, are both permitted to vary with h, then differentiation with respect to h yields

$$\frac{\partial(P_{sc} - P_p)}{\partial h} = \frac{q}{2\pi\sqrt{k_h k_v}} \left\{ \frac{C\mu_a}{h} + \frac{d(C\mu_a)}{dh} \left\{ \ln \left[\frac{\left(\frac{k_h}{k_v}\right)^{\frac{1}{4}} h}{R_p} \right] + s \right\} \right\} - \rho g \tag{5.8}$$

By setting Equation 5.8 to zero, a *stability envelope* is obtained:

$$\frac{C\mu_a}{h} + \frac{d(C\mu_a)}{dh} \left\{ \ln \left[\frac{\left(\frac{k_h}{k_v}\right)^{\frac{1}{4}} h}{R_p} \right] + s \right\} = \frac{2\pi\rho g\sqrt{k_h k_v}}{q} \tag{5.9}$$

Equation 5.9 may be used to assess the stability of GIPR solutions. In addition, it provides significant insight into the mechanics of steam trap control. Perhaps most remarkably, it suggests that, for a given set of operating conditions, there may be

a minimum liquid level below which the fluid interface is unstable. Equation 5.9 is plotted in Figure 5.3 for $C = 0.100h + 0.758$ and $\mu_a = const$. Note that when the production well pressure exceeds the steam chamber pressure, there is no minimum liquid level for stability; the fluid interface is unconditionally stable.

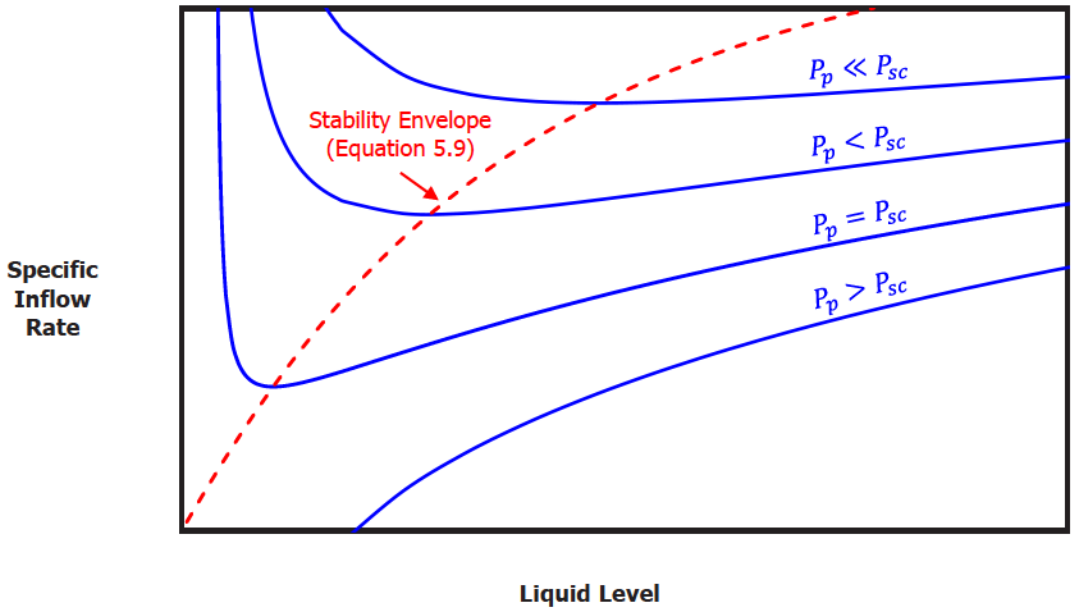

Figure 5.3: Fluid interface stability envelope

5.1.4 Additional Remarks on Stability

Further insight into the stability of the fluid interface may be gained by considering the pressure distribution above the production well. Two such distributions are shown in Figure 5.4, one corresponding to a high-permeability reservoir in which the flow is gravity dominated, and the other corresponding to a low-permeability reservoir with a much greater loss of fluid potential in the near-wellbore region.

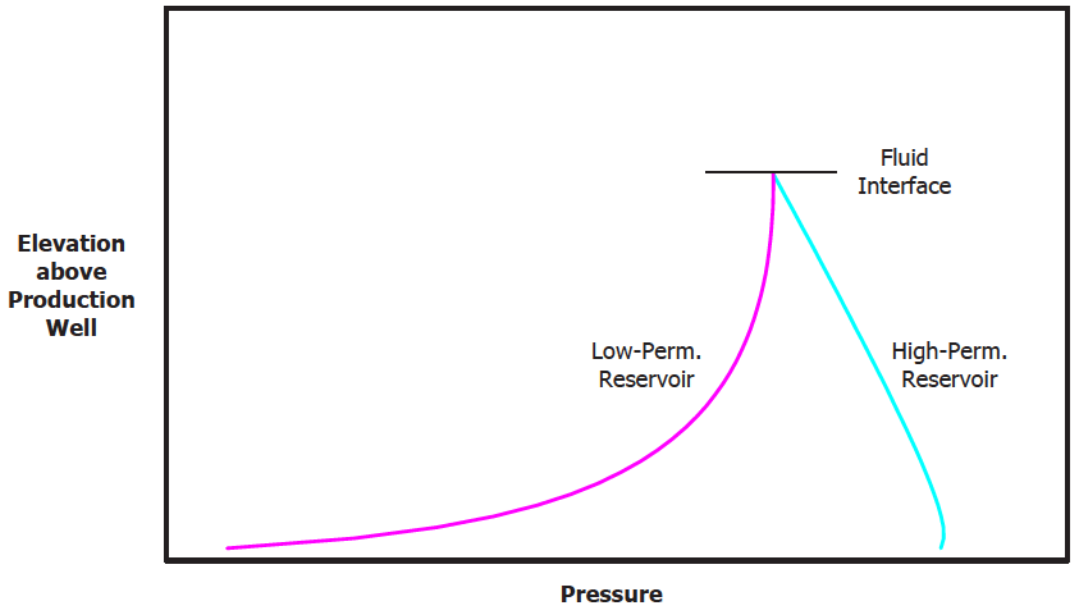

Figure 5.4: Pressure distributions in high- and low-permeability reservoirs

In the high-permeability reservoir, the pressure gradient near the fluid interface is negative in the upward direction. Because the density of steam is very low, this pressure gradient is nearly equal to the potential gradient for steam. A steam bubble would tend to rise through the liquid pool (because fluid flows in the direction of decreasing potential), and so the liquid pool prevents the flow of steam into the production well. By contrast, in the low-permeability reservoir, the pressure gradient is negative in the downward direction. A steam bubble in the liquid pool would be

drawn toward the production well. In this case, the steam trap would fail.[1]

An approximate condition for the stability of the fluid interface (neglecting the density of steam) is thus

$$\frac{\partial P}{\partial r} < 0 \quad at \quad r = h, \theta = \frac{\pi}{2} \tag{5.10}$$

For a reservoir with isotropic permeability, the pressure distribution in the steam trap was given on page 27 by Equation 3.20:

$$P(r,\theta) = P_p + \frac{\mu_a q}{2\pi k} \ln\left(\frac{r}{R_p}\right) - \rho g r \sin\theta$$

Differentiating Equation 3.20 with respect to r yields

$$\frac{\partial P}{\partial r} = \frac{\mu_a q}{2\pi k}\frac{1}{r} - \rho g \sin\theta \tag{5.11}$$

Setting Equation 5.11 to zero at $r = h, \theta = \frac{\pi}{2}$ gives the stability envelope

$$\frac{\mu_a q}{2\pi k}\frac{1}{h} - \rho g = 0 \tag{5.12}$$

or

$$\frac{\mu_a}{h} = \frac{2\pi\rho g k}{q} \tag{5.13}$$

Equation 5.13 is equivalent to Equation 5.9 with $k_h = k_v = k$, $C = 1$, and $\mu_a = const.$

[1]This interpretation follows that of Edmunds (2000), who has observed similar pressure distributions in reservoir simulations.

5.2 Case Study 1: Variable Pay Thickness

The pay thickness generally varies along the length of a SAGD well pair. Variation in the pay thickness leads to variation in the steam chamber height, which gives rise to variation in the drainage rate. As a first approximation, the drainage rate may be expected to vary with the square root of the steam chamber height (recall Equation 4.3 on page 45).

The first case study investigates the effect of pay thickness variation on the uniformity of the fluid interface position. The pay thickness is assumed to decrease linearly from the heel of the well pair to the toe, as depicted in Figure 5.5, so that the steam chamber height ranges from 30 m down to just 5 m. The drainage rate, plotted as function of position in Figure 5.6, varies with the square root of the steam chamber height, from about 1.35 m^3/day/m (total liquids) at the heel of the well pair to about 0.55 m^3/day/m at the toe. Total production is 1000 m^3/day, a typical rate for a well-performing well pair in high-quality sand. In this scenario, the production challenge is to maintain a uniform liquid level while sustaining a highly non-uniform drainage distribution.

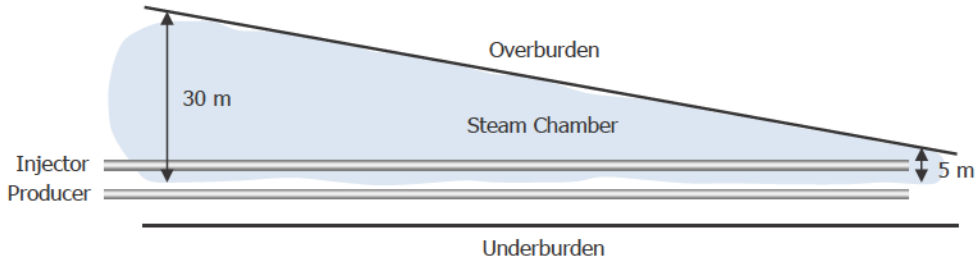

Figure 5.5: Schematic for Case Study 1

The inputs for the first case study are summarized in Table 5.1. The reservoir was assumed to be homogeneous and isotropic with a permeability of 6 D. Given the weak correlation observed in Section 4.3.5 between the inflow temperature and

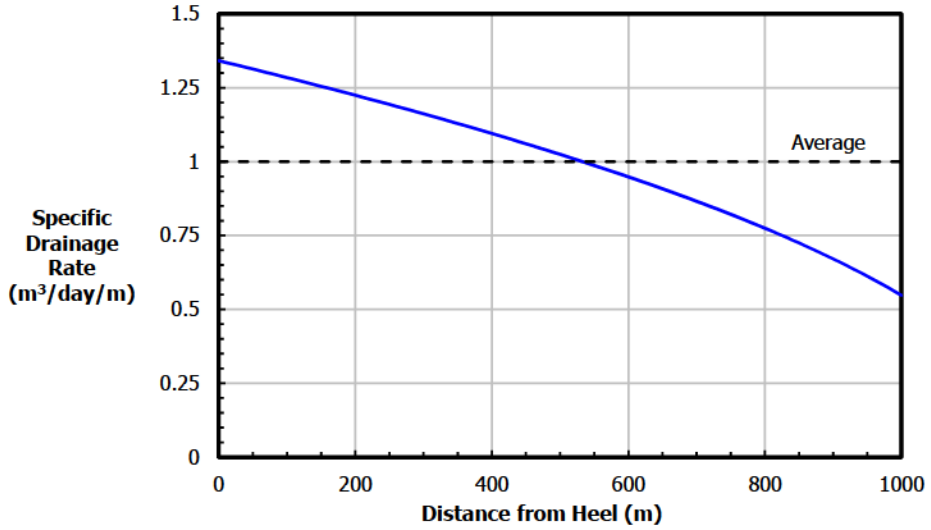

Figure 5.6: Drainage distribution for Case Study 1

the liquid level in the reservoir simulations with high drainage rates, a constant inflow temperature of 202 °C was specified. This inflow temperature corresponds approximately to a production well subcool of 20 °C. The remaining inputs, including the oil properties and oil-water relative permeability curves, were consistent with the reservoir simulations.

Table 5.1: Inputs for Case Study 1

Parameter	Value
Reservoir Permeability	6 D
Relative Permeability	See Figure 4.4
Oil Viscosity	From Firebag Resource Team
Oil Density	See Table 4.4
Water Cut	75%
Steam Chamber Temperature	222 °C
Inflow Temperature	202 °C
Productive Well Length	1000 m
Production Rate (Total Liquids)	1000 m^3/day
Production Well Skin Factor	0

5.2.1 Performance of Conventional Completion Designs

Two conventional completion designs were considered for the production well and are illustrated in Figure 5.7. In the first design, only slotted liner is installed in the horizontal borehole. Production fluid entering the liner flows in the uphole direction. In the second design, fluid is produced through a tubing string or *tailpipe* that is extended to the toe of the liner. Fluid entering the liner must flow to the toe of the well before reversing direction and entering the tailpipe. In all cases, the diameter of the slotted liner was assumed to be 219 mm (8 5/8 inches). Two tailpipe sizes were considered: 114 mm (4 1/2 inches) and 140 mm (5 1/2 inches).

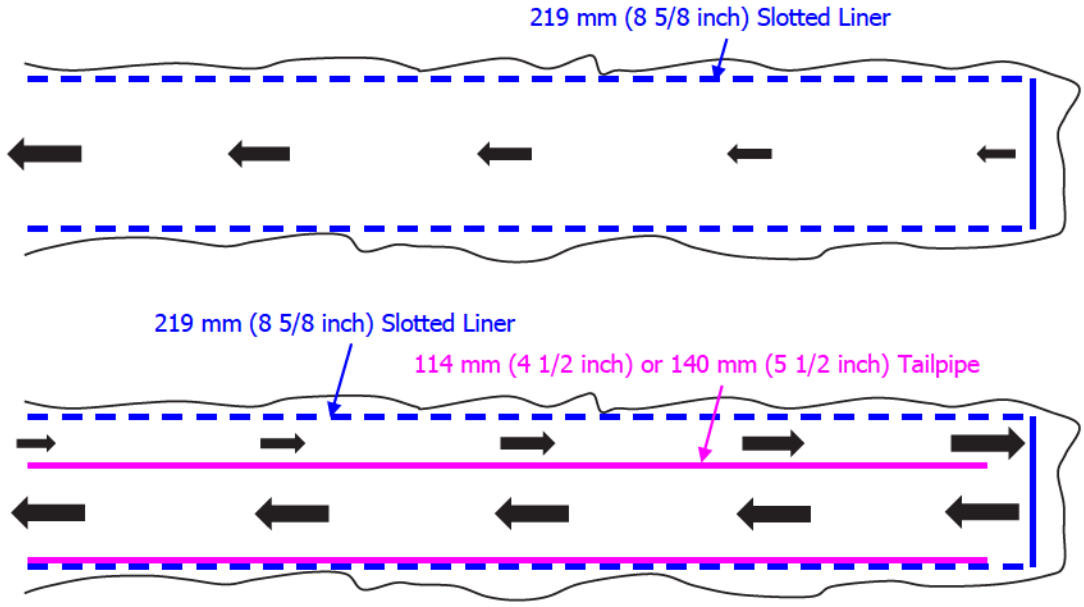

Figure 5.7: Conventional completion designs for production well

The liquid level distribution predicted by the three-dimensional model without a tailpipe is presented in Figure 5.8. The pressure distribution in the wellbore is plotted on a secondary vertical axis. In the upper half of the figure, dashed horizontal lines denote the locations of the injection and production wells. In the lower half of the figure, the dashed horizontal line denotes the steam chamber pressure (2409 kPa). In this and subsequent cases, the pressure at the heel of the production well has been adjusted to maintain a minimum liquid level of 1 m.

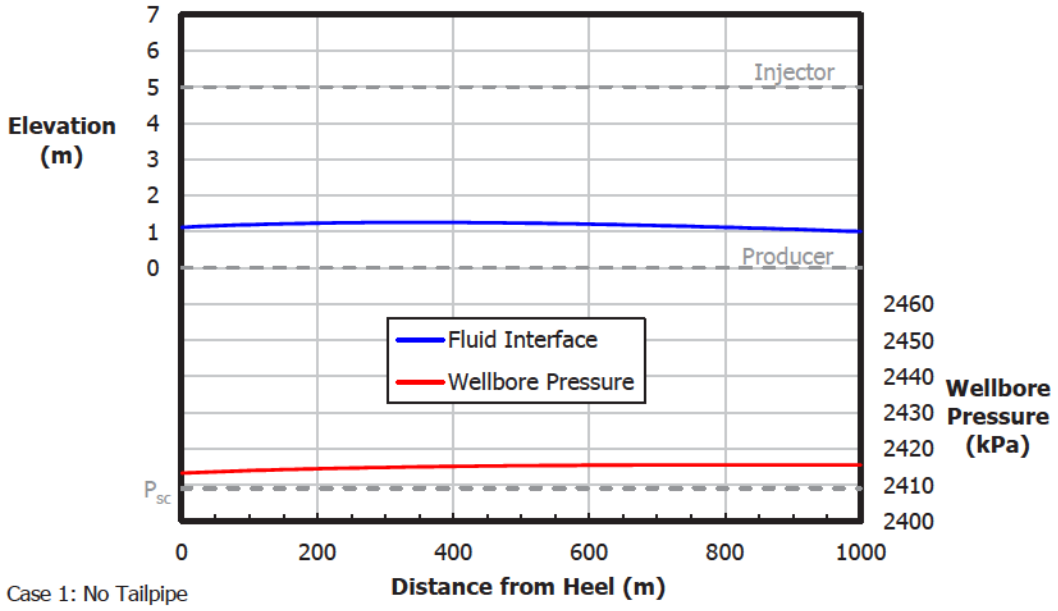

Figure 5.8: Liquid level distribution without tailpipe in Case Study 1

Two competing effects are apparent in the modelling results. First, there is a slight drop in the wellbore pressure from the toe of the well to the heel due to friction loss, which tends to pull down the liquid level at the heel. Second, the non-uniform drainage distribution promotes an opposing tilt of the fluid interface. By chance, these two effects largely cancel each other out, resulting in a fairly uniform liquid level along the length of the well pair.

The liquid level distribution obtained with a 114 mm (4 1/2 inch) tailpipe is presented in Figure 5.9. Here, the "wellbore pressure" is the pressure in the eccentric annulus between the tailpipe and the slotted liner. The wellbore pressure can alternatively be thought of as the *sandface pressure*, the pressure at the interface between the wellbore and the reservoir. Whereas the effects of the wellbore pressure gradient and the non-uniform drainage distribution counteract each other without a tailpipe, the two effects act together when there is a tailpipe. Higher drainage rates and higher wellbore pressures result in higher liquid levels near the heel of the well; lower drainage rates and lower wellbore pressures result in lower liquid levels near the toe. The tailpipe occupies much of the available flow area in the slotted liner, giving rise to an appreciable sandface pressure gradient and an appreciable tilt of the fluid interface.

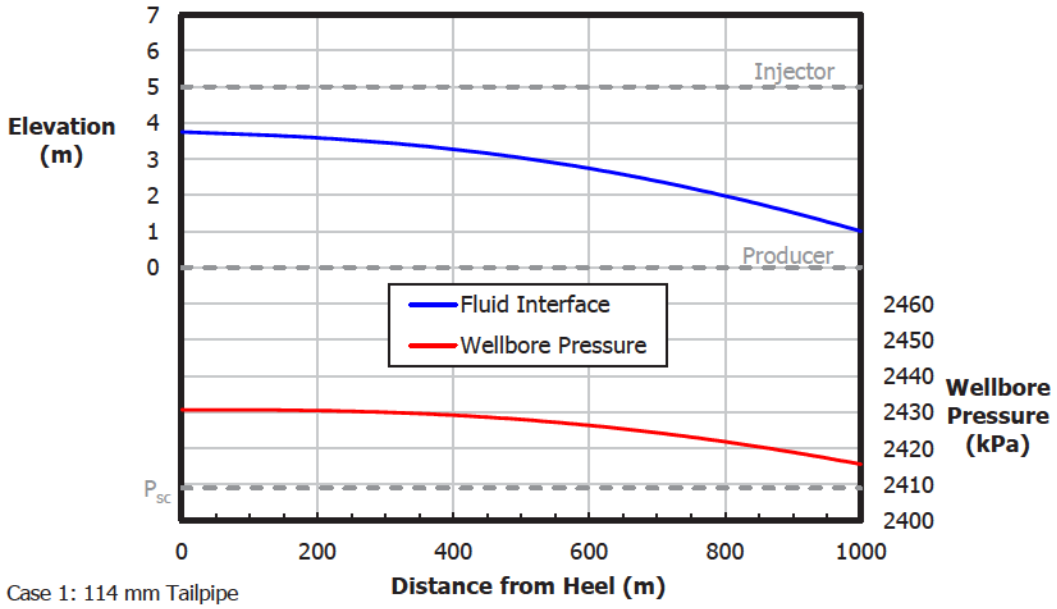

Figure 5.9: Liquid level distribution with 114 mm tailpipe in Case Study 1

Finally, the liquid level distribution obtained with a 140 mm (5 1/2 inch) tailpipe is presented in Figure 5.10. The friction loss in the annulus between the 140 mm tailpipe and 219 mm liner is sufficiently high that the predicted variation in the liquid level exceeds 5 m, the typical spacing between the injection and production wells. Thus, steam trap failure – injector flooding at the heel of the well or steam breakthrough at the toe – would be expected with this completion design. In practice, low liquid levels near the toe of the well would likely not be detected by flowing temperature measurements in the annulus, since the temperature reading would be influenced by cooler fluid originating from the heel. It should be noted that the liquid level near the heel of the well exceeds the range over which the GIPR was verified (up to about 5 m). Nevertheless, it is clear from the modelling results that this completion design is a poor match to the reservoir conditions.

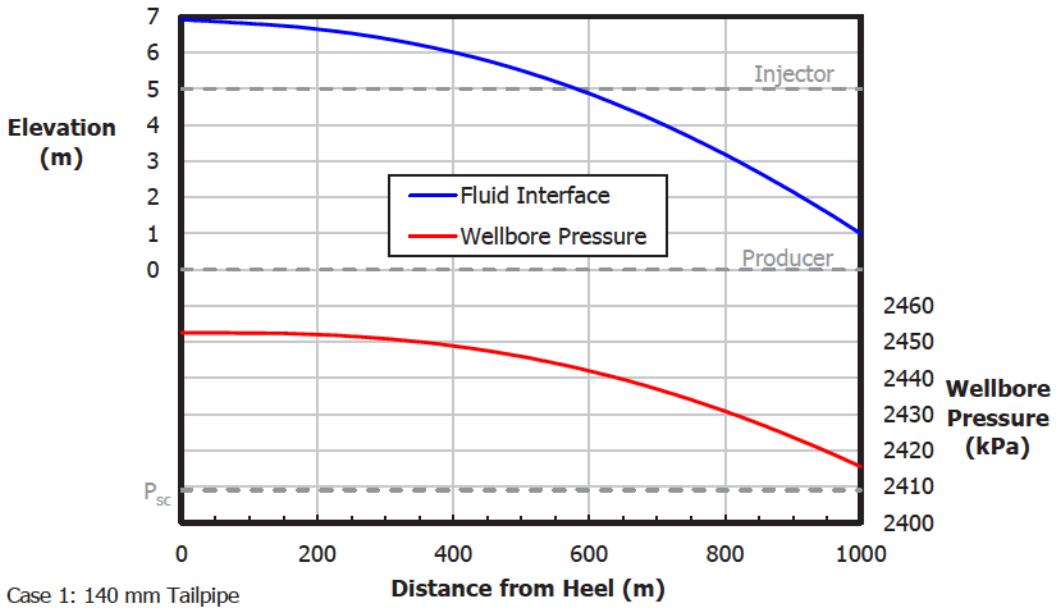

Figure 5.10: Liquid level distribution with 140 mm tailpipe in Case Study 1

5.2.2 Completion Design Optimization

It is apparent that a customized completion design is not required to achieve a uniform liquid level in this scenario; an open liner will suffice. Some operators prefer to install a tailpipe, however, because they feel it provides a safeguard against steam breakthrough in production wells with mechanical lift. Such wells are often controlled based on the subcool at the intake of a pump that is installed at the heel of the well. The friction loss through the tailpipe ensures that the pressure at the pump intake is lower than the pressure at the sandface. Thus, even if control issues permit the pump intake to reach saturated conditions, there is a chance that the sandface will remain at subcooled conditions due to the higher local pressure.

In anticipation of a scenario in which an operator may wish to retain a tailpipe, an alternate completion design was considered in which a 114 mm tailpipe is landed 500 m from the heel of the well, as illustrated in Figure 5.11. The design objective is to reduce the sandface pressure gradient while retaining some friction loss through the tailpipe as a safeguard against steam breakthrough.

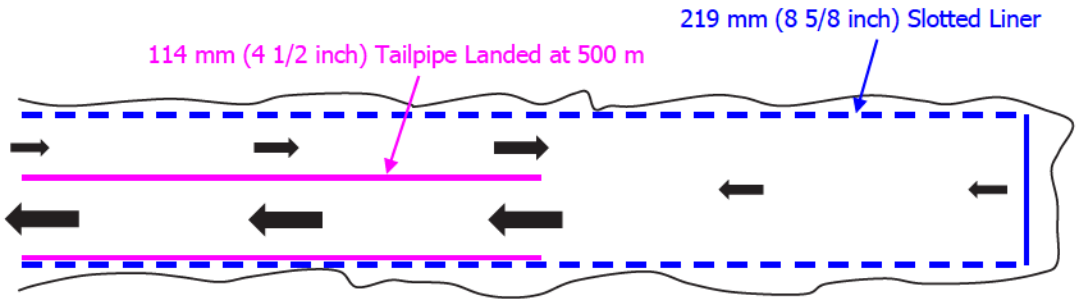

Figure 5.11: 114 mm tailpipe landed at 500 m from the heel

The liquid level distribution achieved with the shortened 114 mm tailpipe is presented in Figure 5.12. The completion design succeeds in reducing the sandface pressure gradient significantly, decreasing the liquid level variation to less than 1 m.

Although the pressure distribution in the tailpipe is not shown, the total friction loss through the tailpipe is approximately 100 kPa, which would provide a modest operational safeguard.

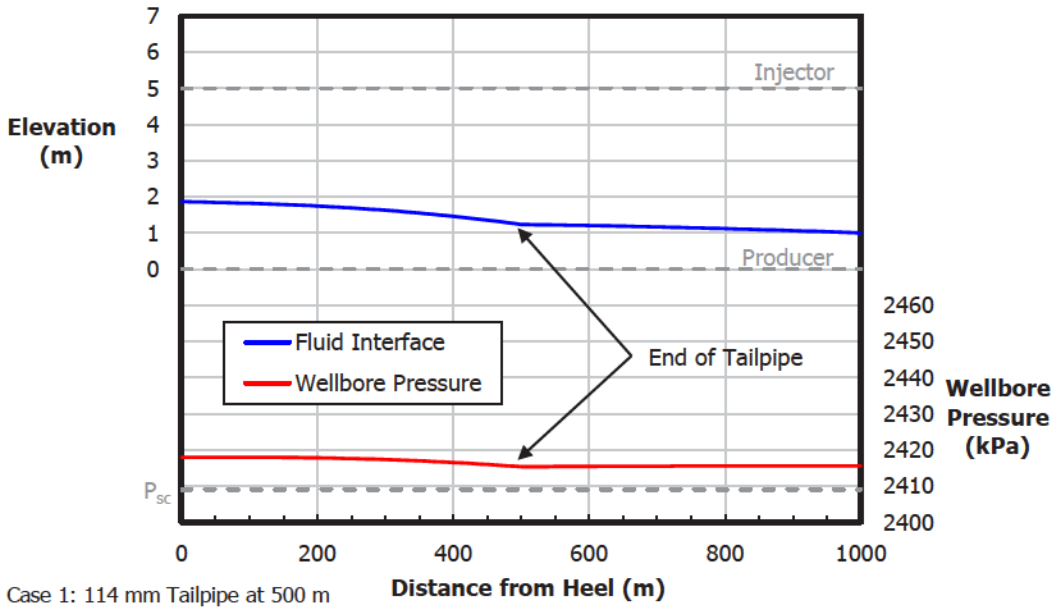

Figure 5.12: Liquid level with shortened 114 mm tailpipe in Case Study 1

5.2.3 Remarks

This case study reveals the robustness of the SAGD process in high-permeability reservoirs. Only a small variation in the fluid interface position is required to support a large variation in the drainage rate. The non-uniformity of the preceding liquid level distributions is mainly the result of sandface pressure gradients introduced by the completion designs. Indeed, this case study demonstrates the potential of simple, open liner completions in high-quality reservoirs.

5.3 Case Study 2: Non-Uniform Permeability

Like the pay thickness, the reservoir permeability generally varies along the length of a SAGD well pair. Low-permeability zones above the injection well hinder steam chamber growth and reduce the drainage rate. Low-permeability zones between the injection and production wells increase the difference in fluid potential that is required to drive liquid to the production well.

The second case study investigates the effect of a low-permeability zone on the uniformity and stability of the fluid interface. A 200 m interval with a permeability of just 200 mD is introduced in an otherwise 6 D reservoir, as illustrated in Figure 5.13. The low-permeability zone is assumed to be sufficiently large to affect both the drainage rate in the steam chamber and the flow through the steam trap. The drainage rate varies with the square root of the permeability according to Equation 4.3, as shown in Figure 5.14. The remaining inputs are consistent with the first case study and summarized in Table 5.1. In this scenario, the production challenge is to recover bitumen from the low-permeability zone, which requires drawing down the sandface pressure significantly, while maintaining the steam trap elsewhere along the well.

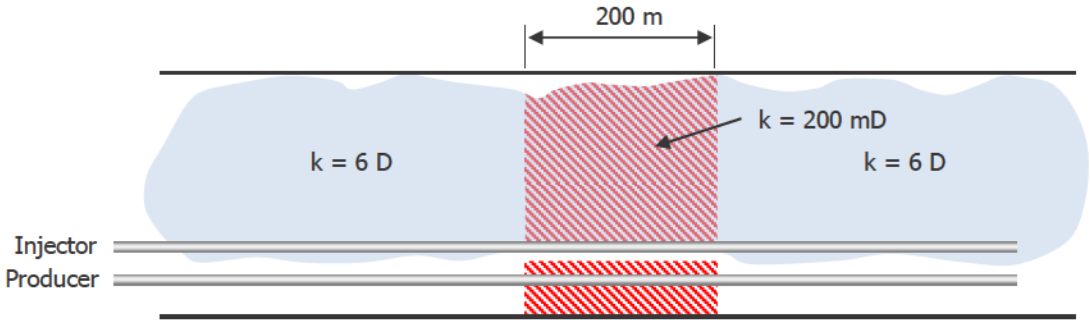

Figure 5.13: Schematic for Case Study 2

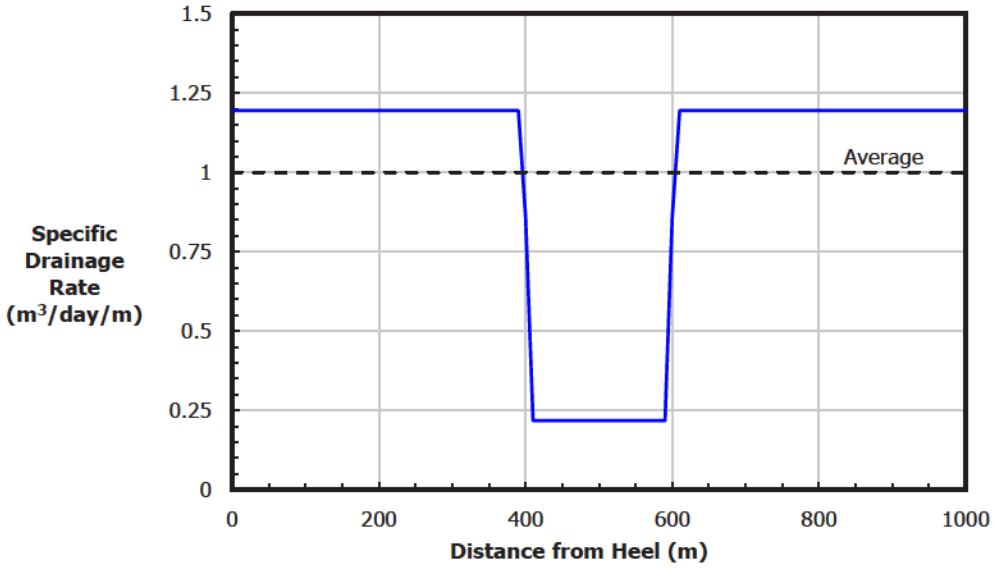

Figure 5.14: Drainage distribution for Case Study 2

5.3.1 Performance of Conventional Completion Designs

An abrupt change in the reservoir permeability along the length of the production well presents a major operational challenge. Where the permeability is high, fluid may be produced at a relatively high sandface pressure because the loss of fluid potential in the near-wellbore reservoir is small. Where the permeability is low, however, a lower sandface pressure is required. Because the high- and low-permeability regions are hydraulically coupled by the wellbore, it is difficult to apply the appropriate sandface pressures to both zones simultaneously.

The liquid level distribution predicted for an open 219 mm liner (no tailpipe) is presented in Figure 5.15 to demonstrate the production challenge. A relatively high wellbore pressure has been specified based on the conditions in the high-permeability regions of the reservoir. In these regions, the inflow rate matches the prescribed drainage rate and the fluid interface is stable. In the low-permeability zone, however, there is no liquid level at which the inflow rate would match the specified drainage

rate; no solution to the GIPR exists. The nonexistence of a solution indicates that the prescribed steam chamber conditions could not be sustained by this completion design. Physically, the accumulation of liquid around the production well would be expected to impede or prevent steam chamber development in the low-permeability zone. The inflow rate in the low-permeability zone could be increased by reducing the wellbore pressure, but this would compromise the steam trap in the high-permeability regions.

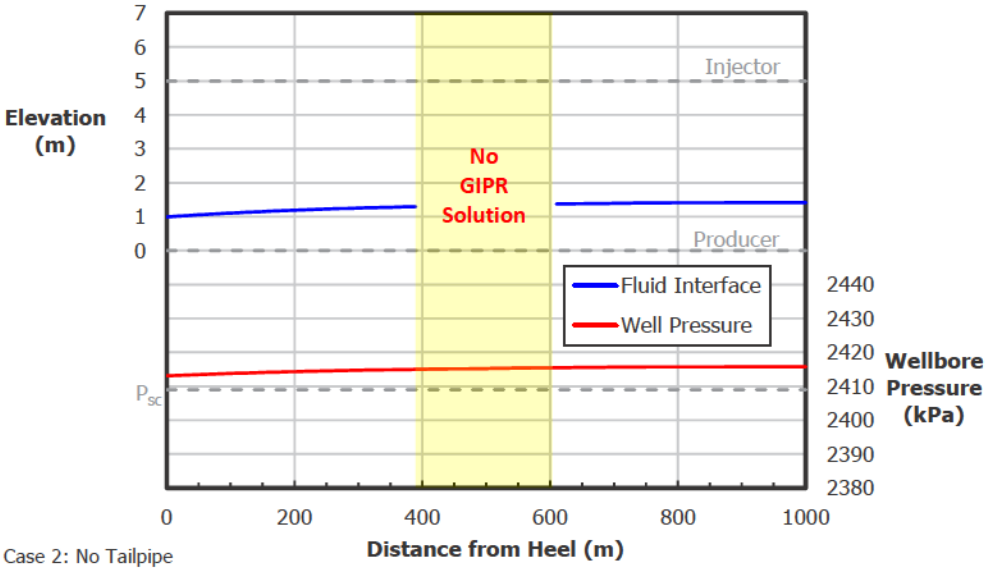

Figure 5.15: Liquid level distribution without tailpipe in Case Study 2

The same production challenge is encountered with 114 mm and 140 mm tailpipes. When a relatively high wellbore pressure is specified based on the conditions in the high-permeability regions of the reservoir, there is no solution to the GIPR in the low-permeability zone. The partial liquid level distributions obtained with tailpipes are included in Appendix B.

It should be noted that the influence of the liquid level on the drainage rate was neglected in this case study. In reality, a rise in the liquid level reduces the effective height of the steam chamber and, in turn, the drainage rate. If the liquid level and

the drainage rate were coupled in the model, then it is possible that a solution to the GIPR would exist in the low-permeability zone. In any event, however, the modelling results would indicate a tendency for liquid to accumulate in the low-permeability zone, and the conclusions from the analysis would be the same.

5.3.2 Completion Design Optimization

In conventional oil and gas wells, it is common to isolate different zones of the reservoir hydraulically using *packers* – devices that expand once downhole to provide a seal between the production tubing and the liner. Packers have seen comparatively little use in SAGD wells, likely due in part to the technological demands of the high-temperature SAGD environment and in part to the high quality of early SAGD reservoirs. As packer technology evolves and operators apply the SAGD process to more and more challenging reservoirs, however, it is anticipated that their use in SAGD wells will increase.

In this case study, a novel completion design was trialed which incorporates *baffles* in a 140 mm tailpipe to provide hydraulic isolation between the high- and low-permeability regions of the reservoir. Here, the term baffle is substituted for packer to highlight the uniqueness of the SAGD application. Whereas high-pressure seals are often required in other applications, it will be demonstrated that the pressure difference across the baffles is relatively small in this application. The completion design is depicted in Figure 5.16, and its key features are as follows:

- Two baffles are included in the tailpipe at 400 m and 600 m from the heel of the well to hydraulically isolate the low-permeability zone.
- Clusters of ports through which fluid may enter the tailpipe are drilled at 200 m, 500 m, and 800 m from the heel of the well. The flow resistance through the port

clusters may be customized by adjusting the number and size of the ports. The completion design could alternatively incorporate tubing-conveyed flow control devices.

- The end of the tailpipe is capped so that fluid from the toe of the reservoir must flow through the ports at 800 m from the heel, providing improved control over the sandface pressure distribution.

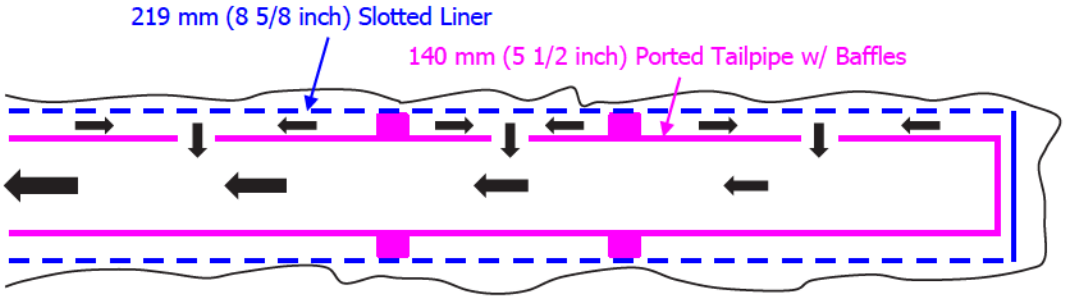

Figure 5.16: Ported 140 mm tailpipe with baffles

After optimization of the number and size of the ports, the liquid level distribution presented in Figure 5.17 was achieved. In the high-permeability zones, the sandface pressure exceeds the steam chamber pressure and production is gravity driven. In the low-permeability zone, the sandface pressure is drawn down to about 20 kPa below the steam chamber pressure. A uniform liquid level was desired along the full length of the well pair; however, the stability envelope given by Equation 5.9 restricts the minimum liquid level in the low-permeability zone.

To investigate the stability of the fluid interface in the low-permeability zone, the GIPR was plotted for $k = 200$ mD and $P_p = 2390$ kPa to yield Figure 5.18. The minimum stable liquid level given by Equation 5.9 is denoted by a dashed vertical line, and the operating conditions in the low-permeability zone are denoted by a green point. The near-horizontal relationship between the inflow rate and the liquid

level around the operating point indicates that the fluid interface is only marginally stable. In reality, the liquid level distribution shown in Figure 5.17 could not likely be sustained. Thus, even with a highly customized completion design, steam trap failure would be anticipated in the low-permeability zone.

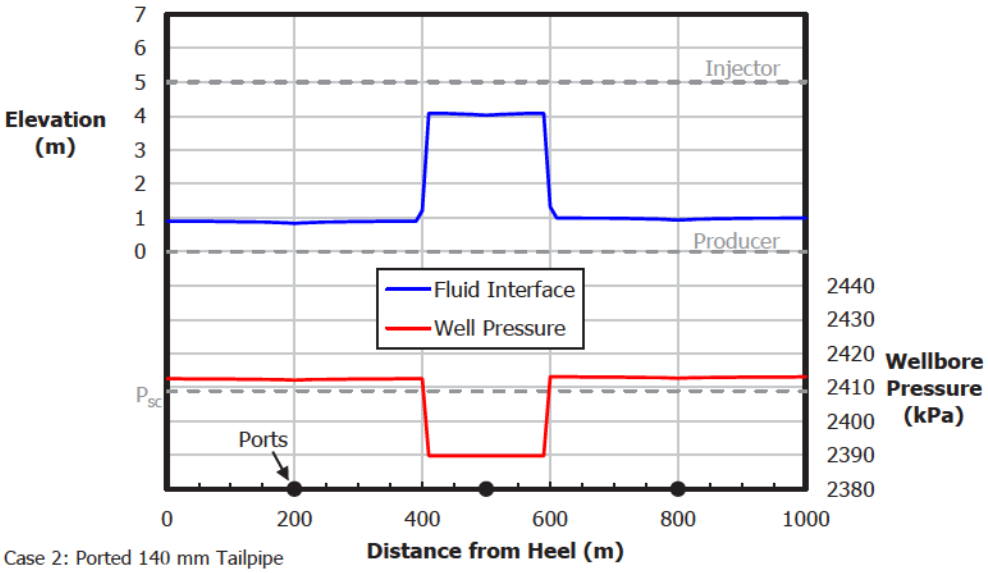

Figure 5.17: Liquid level distribution with ported 140 mm tailpipe in Case Study 2

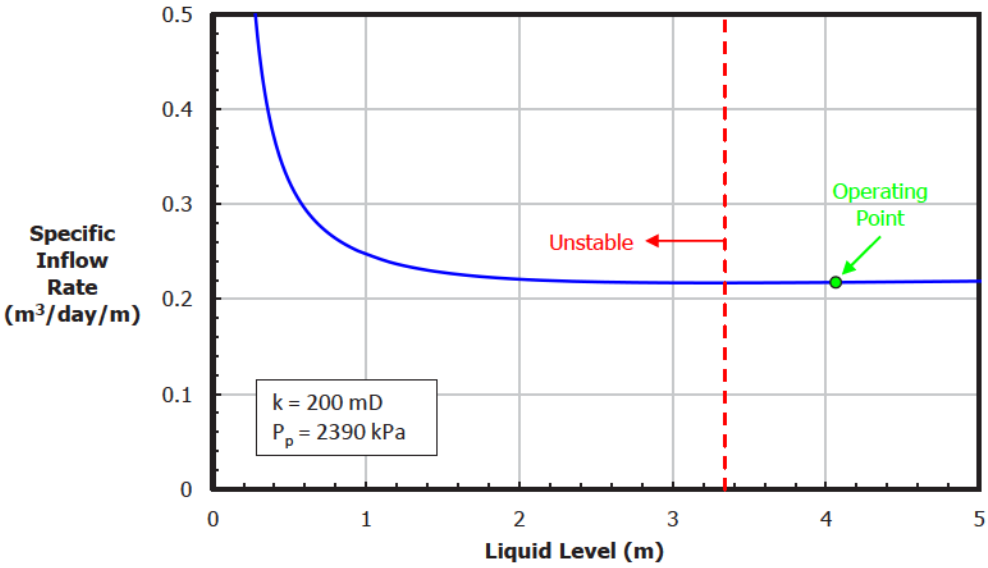

Figure 5.18: GIPR for $k = 200$ mD, $P_p = 2390$ kPa

5.3.3 Remarks

This case study reveals a fundamental limit to the permeability of the reservoir in which steam trap control can be successfully applied. The existence of a limit becomes apparent by noting that the potential loss through the steam trap scales with q/k, while the drainage rate in the steam chamber scales approximately with $\sqrt{k}$. As the permeability of the reservoir decreases, the rise in the flow resistance through the steam trap outpaces the reduction in drainage from the steam chamber. The flow through the steam trap shifts from gravity driven to pressure driven, and with a sufficient reduction in permeability, the steam trap fails. Further research is recommended to quantify the reservoir requirements for steam trap control.

Note that axial flow through the near-wellbore reservoir was neglected in this case study. If included in the model, axial flow through the reservoir would help to redistribute liquid from the low-permeability zone to the adjacent high-permeability regions. The axial flow resistance through the low-permeability reservoir would be exceptionally high, however, and so this effect would be small.

The best operating policy in this scenario would likely be to sacrifice production from the low-permeability zone in order to maintain the steam trap in the regions with higher permeability. Even with a well-developed steam chamber, the drainage rate in the low-permeability zone would be low, and so the sacrifice would be small. A related scenario for future consideration is one with a localized zone of unusually high permeability. The operational challenge would be to maintain production from the predominantly low-permeability reservoir while avoiding steam breakthrough in the high-permeability zone. Throttling back the production well to prevent steam breakthrough would yield a stiff penalty to the production rate, and so there would be opportunity for performance improvements through completion design optimization.

5.4 Case Study 3: Inclined Production Well

So far, SAGD well pairs – and the reservoirs into which they are drilled – have been depicted as perfectly horizontal. In reality, the depth of the reservoir floor generally varies along the length of a well pair. Instead of drilling horizontal wells, some operators drill wells *toe-up* or *toe-down* so that they closely follow the slope of the reservoir floor. This drilling practice is motivated by a desire to minimize the volume of oil that is "trapped" below the production well.

The third case study investigates the relationship between the production well trajectory and the fluid interface position. A 2 m drop in elevation is introduced along the production well to yield the toe-down trajectory shown in Figure 5.19. A uniform drainage rate of 1 m^3/day/m is assumed, and all other inputs are consistent with the first two case studies (see Table 5.1). Note that the injection well is also depicted as toe-down in Figure 5.19 because operators typically maintain a uniform spacing between the injector and producer. The injection well trajectory, however, has no bearing on the modelling results; the steam chamber pressure is assumed to be uniform, as in the previous case studies.

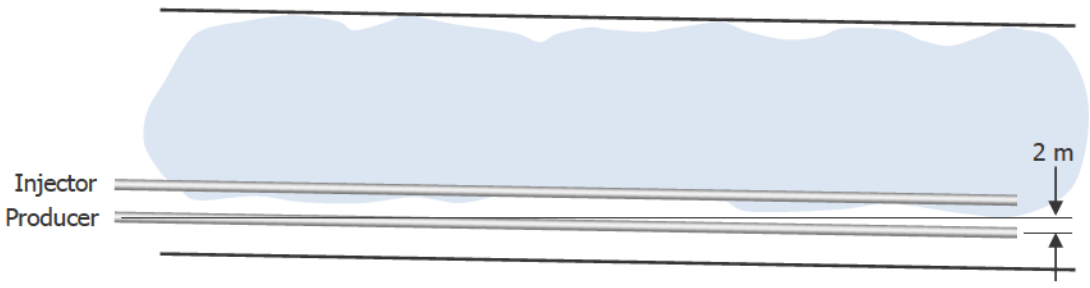

Figure 5.19: Schematic for Case Study 3

5.4.1 Performance of Conventional Completion Designs

The conventional completion designs considered in the third case study were identical to those considered in the first two case studies. The liquid level and wellbore pressure distributions predicted without a tailpipe are presented in Figure 5.20. Here, the liquid level is reported relative to the toe of the production well so that the figure accurately portrays the position of the fluid interface in relation to the well pair.

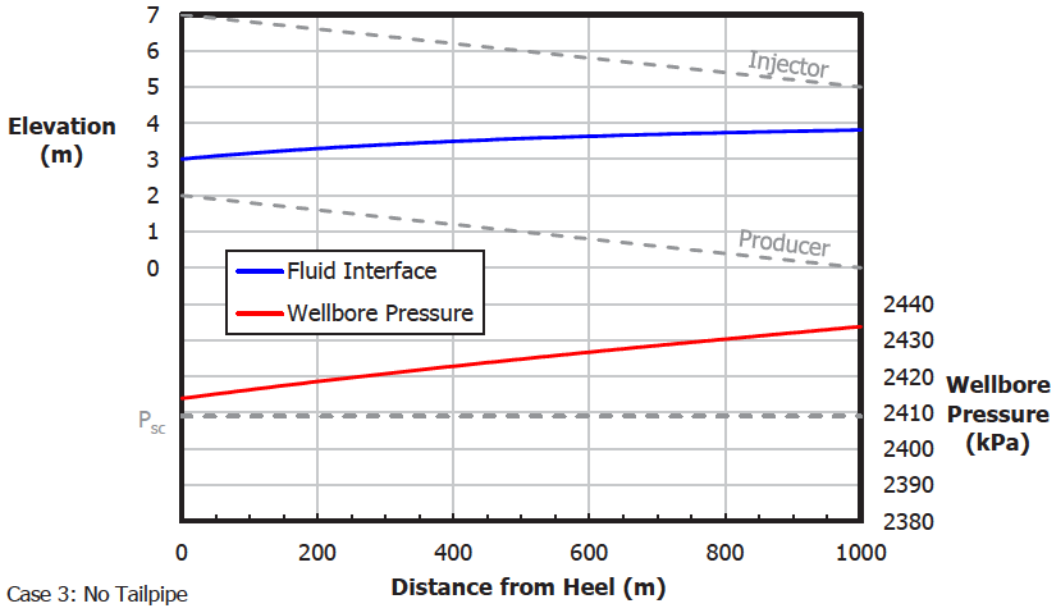

Figure 5.20: Liquid level distribution without tailpipe in Case Study 3

The modelling results reveal that drilling the production well toe-down poses a major challenge to steam trap conformance. The wellbore pressure decreases by about 20 kPa from the toe of the well to the heel, corresponding approximately to the hydrostatic pressure gradient and 2 m of elevation change. As a result, the fluid interface is much nearer to the heel of the production well than to the toe. While steam breakthrough and injector flooding are avoided, a more severe incline – with, for example, 5 m of elevation change – would lead to failure of the steam trap unless counteracted by the wellbore completion design.

The liquid level distributions obtained with 114 mm (4 1/2 inch) and 140 mm (5 1/2 inch) tailpipes are presented in Figures 5.21 and 5.22, respectively. With a 114 mm tailpipe, the friction loss in the annulus between the tailpipe and the liner is on the order of 20 kPa, and so it nearly cancels out the pressure variation associated with elevation change. Consequently, the separation between the fluid interface and the production well is fairly uniform – the completion design is a good match to the conditions. By contrast, with a 140 mm tailpipe, the friction loss in the annulus far exceeds the pressure variation due to elevation change. The fluid interface is much nearer to the toe of the production well than to the heel, and the operating window in which there is neither steam breakthrough nor injector flooding is narrowed.

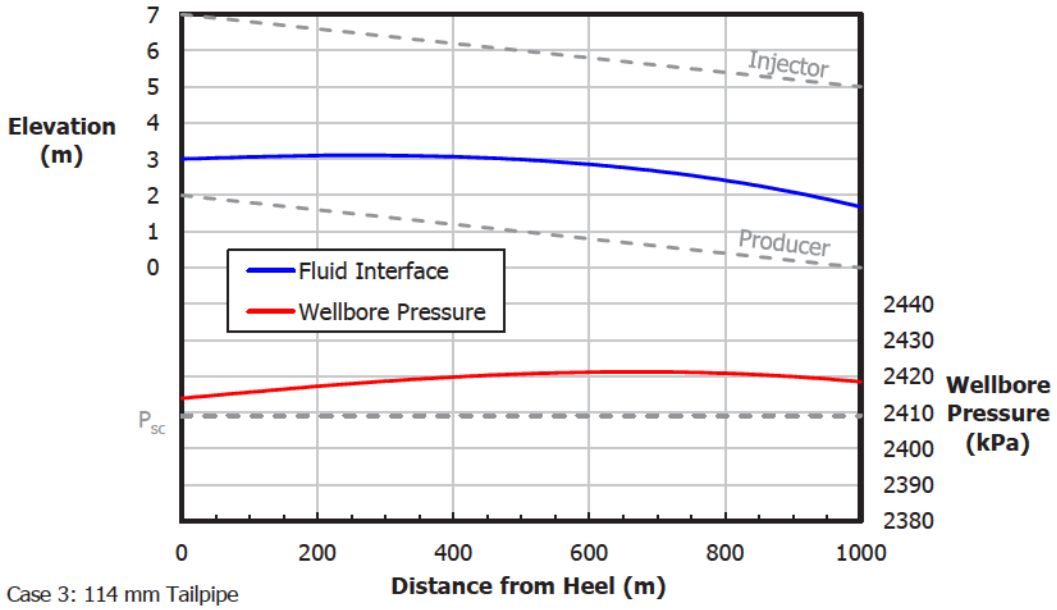

Figure 5.21: Liquid level distribution with 114 mm tailpipe in Case Study 3

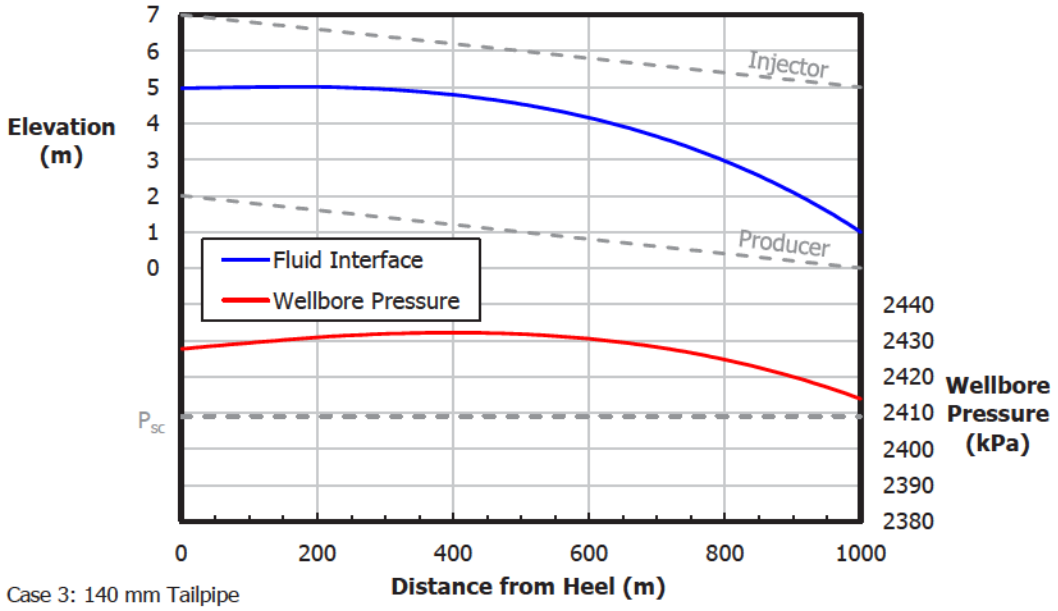

Figure 5.22: Liquid level distribution with 140 mm tailpipe in Case Study 3

5.4.2 Completion Design Optimization

While the separation between the fluid interface and the production well is fairly uniform with a 114 mm tailpipe, the friction loss in the annulus and the hydrostatic pressure variation do not cancel each other out exactly. The hydrostatic pressure gradient is constant and gives rise to a linear wellbore pressure distribution, but the friction loss gradient increases from the heel of the well to the toe (due to increasing flow velocity) and gives rise to a nonlinear pressure distribution.

In an attempt to promote a uniform flow velocity in the annulus between the tailpipe and the slotted liner, a completion design was trialed in which the diameter of the tailpipe decreases from the heel of the well to the toe. After some experimentation, the design shown in Figure 5.23 was reached. The tailpipe comprises 178 mm (7 inch) tubing for the first 200 m of the productive well length, 140 mm tubing for the next 300 m, and 114 mm tubing for the remaining 500 m.

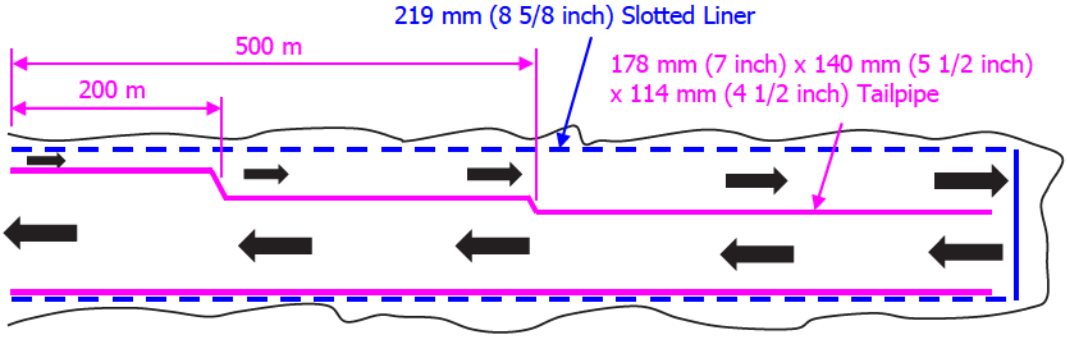

Figure 5.23: Tapered tailpipe

Figure 5.24 presents the liquid level achieved with the tapered tailpipe. The annulus pressure is nearly uniform along the length of the well, leading to a uniform separation between the fluid interface and the producer. Relative to the conventional completion designs, the tapered tailpipe maximizes the operating window in which there is neither steam breakthrough nor injector flooding. The fluid interface may rise or fall in response to changing reservoir or wellbore conditions with reduced risk of steam trap failure.

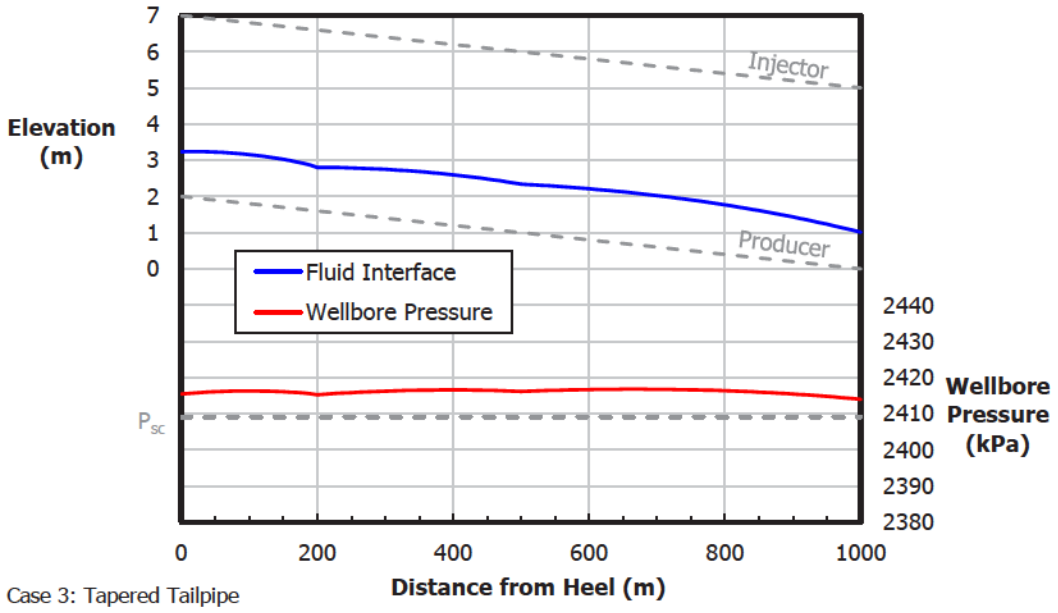

Figure 5.24: Liquid level distribution with tapered tailpipe in Case Study 3

5.4.3 Remarks

This case study highlights the challenge of drilling SAGD well pairs that follow the slope of the reservoir floor. Nevertheless, the value of the bitumen trapped below the production well can be compelling, and it is anticipated that operators will continue to drill well pairs toe-up or toe-down. As more and more such well pairs are drilled, the GIPR and similar models will become increasingly useful for optimizing wellbore completion designs to the unique challenges faced in each reservoir.

Chapter 6

Conclusions and Recommendations

6.1 Conclusions

6.1.1 Model Formulation and Verification

An analytical model called a *gravity inflow performance relationship* (GIPR) was formulated to describe the flow through the SAGD steam trap. The GIPR predicts the position of the liquid-vapour interface given the inflow rate, the pressure difference between the steam chamber and the production well, and the reservoir and fluid properties. The GIPR accounts for permeability anisotropy and relative permeability effects, making it unique from previous models.

The GIPR was verified through simulations in STARS, a higher-order numerical model. The verification cases were designed to represent commercial SAGD projects in the Athabasca oil sands. The agreement between the GIPR and STARS was initially good and improved further by introducing a liquid level-dependent correction factor in the GIPR to capture non-axisymmetry in the flow conditions. The correction factor reduced the root mean square deviation (RMSD) in liquid level between the

two models from 0.23 m to just 0.17 m.

Consistent with previous research, the numerical simulations indicate a positive correlation between the subcool in the production well and the liquid level. The slope of the correlation, however, is not consistent with the 10 °C/m rule of thumb and depends on the inflow rate, which is thought to influence whether the heat transfer in the steam trap is conduction or convection dominated. The numerical simulations also indicate that the subcool in the production well does not necessarily tend to zero at low liquid levels, which challenges (or at least complicates) the practice of inferring the liquid level from the subcool.

6.1.2 Case Studies

The GIPR was coupled to FloNet, a wellbore hydraulics model, to investigate the uniformity and stability of the fluid interface along the length of a SAGD well pair. Three case studies were conducted, each exploring a different challenge to steam trap control. The performance of conventional completion designs for the production well was evaluated. Then, the completion design was optimized to improve the uniformity of the fluid interface and reduce the risk of steam trap failure.

Variable Pay Thickness

In high-permeability reservoirs, large variations in the pay thickness – and, hence, the drainage rate – cause only small variations in the liquid level. In this case study, the best performance was achieved with an open liner, which minimized the pressure variation along the sandface. Long tailpipes introduced an undue wellbore pressure gradient and a corresponding tilt of the fluid interface.

Non-Uniform Reservoir Permeability

When the permeability of the reservoir is low (e.g., 200 mD), the GIPR reveals that the liquid-vapour interface is likely to be unstable, even at low flow rates. Instability occurs because the loss of fluid potential through the near-wellbore reservoir overwhelms the stabilizing effect of gravity. In this case study, the instability of the fluid interface could not be resolved by optimizing the completion design for the production well – either steam breakthrough or injector flooding would be expected.

Inclined Production Well

Drilling the production well toe-up or toe-down may narrow the operating window in which there is neither steam breakthrough nor injector flooding. In the absence of drawdown, the fluid interface tends to a horizontal position; it does not follow the slope of the production well. In this case study, a uniform separation between the fluid interface and the production well was achieved using a tapered tailpipe, which creates friction loss to counteract the hydrostatic pressure variation along the well.

6.2 Recommendations

6.2.1 Validation with Field Data

The GIPR was verified against a higher-order numerical model, but it has not been validated using field data. As instrumentation for SAGD wells improves and distributed temperature, pressure, and flow rate measurements become available, further validation of the model is recommended. Production wells with multiple instrumented and hydraulically isolated zones would be good candidates for validating the GIPR, since the uncertainty associated with spatial variation of the model

parameters would be reduced.

6.2.2 Effect of Skin Factor

The skin factor was set to zero throughout this thesis to permit the fundamental verification of the GIPR. In reality, however, it is likely that the skin factor is almost always nonzero because fluid must converge to slots or screens on the production liner, introducing additional potential loss. In cases with plugging or scaling, the skin factor may be substantial. Therefore, an investigation of the effect of the skin factor on the uniformity and stability of the fluid interface is recommended. The investigation should consider scenarios in which the skin factor varies along the length of the production well.

6.2.3 Effect of Steam Chamber Pressure Variation

There are conflicting statements in the literature about the capacity of the steam chamber for axial flow, and thus about the uniformity of the steam chamber pressure. It is speculated that the capacity for axial flow depends on the maturity of the steam chamber, but further study of this topic is recommended. The analysis methodology demonstrated in this thesis provides an efficient means of quantifying the effect of steam chamber pressure variation on steam trap conformance.

6.2.4 Relationship Between Subcool and Liquid Level

The results of the numerical simulations conducted in this thesis – namely, that the subcool in the production well may be nearly insensitive to the liquid level, and that the subcool does not always tend to zero at low liquid levels – challenge current methods for inferring the position of the fluid interface. Continued research on

the relationship between wellbore temperature measurements and the fluid interface position is recommended. Both flowing measurements, taken while the well is producing, and fall-off measurements, taken while the well is shut-in, are of interest.

Bibliography

AER (2015). Alberta's Energy Reserves 2014 and Supply/Demand Outlook 2015-2024. Report No. ST98-2015, Alberta Energy Regulator, Calgary, Alberta (June 2015).

Aherne, A. L. and B. Maini (2008). Fluid Movement in the SAGD Process: A Review of the Dover Project. *Journal of Canadian Petroleum Technology 47*(1), 31–37. PETSOC-08-01-31. http://dx.doi.org/10.2118/08-01-31.

Akin, S. (2005). Mathematical Modeling of Steam-Assisted Gravity Drainage. *SPE Reservoir Evaluation & Engineering 8*(5), 372–376. SPE-86963-PA. http://dx.doi.org/10.2118/86963-PA.

Anand, J., W. H. Somerton, and E. Gomaa (1973). Predicting Thermal Conductivities of Formations From Other Known Properties. *Society of Petroleum Engineers Journal 13*(5), 267–273. SPE-4171-PA. http://dx.doi.org/10.2118/4171-PA.

Azad, A. and R. J. Chalaturnyk (2010). A Mathematical Improvement to SAGD Using Geomechanical Modelling. *Journal of Canadian Petroleum Technology 49*(10), 53–64. SPE-141303-PA. http://dx.doi.org/10.2118/141303-PA.

Azad, A. and R. J. Chalaturnyk (2012). An improved SAGD analytical

simulator: Circular steam chamber geometry. *Journal of Petroleum Science and Engineering 82-83*, 27–37. http://dx.doi.org/10.1016/j.petrol.2012.01.003.

Azad, A. and R. J. Chalaturnyk (2013). Application of Analytical Proxy Models in Reservoir Estimation for SAGD Process: UTF-Project Case Study. *Journal of Canadian Petroleum Technology 52*(3), 219–232. SPE-165576-PA. http://dx.doi.org/10.2118/165576-PA.

Banerjee, S., R. Jobling, T. Abdelfattah, and H. Nguyen (2013). The Role of Autonomous Flow Control in SAGD Well Design. Paper SPE-166266-MS presented at the SPE Annual Technical Conference and Exhibition, New Orleans, Louisiana, 30 September-2 October. http://dx.doi.org/10.2118/166266-MS.

Becerra, O., B. Kearl, and A. Sanwoolu (2014). A Systematic Approach for Inflow Control Devices Testing in Mackay River SAGD Wells. Paper SPE-170055-MS presented at the SPE Heavy Oil Conference-Canada, Calgary, Alberta, 10-12 June. http://dx.doi.org/10.2118/170055-MS.

Bedry, M. and J. Shaw (2012). Using a new Intelligent Well Technology Completions Strategy to Increase Thermal EOR Recoveries-SAGD Field Trial. Paper SPE-154760-MS presented at the SPE EOR Conference at Oil and Gas West Asia, Muscat, Oman, 16-18 April. http://dx.doi.org/10.2118/154760-MS.

Bennion, D. B., S. Gupta, S. Gittins, and D. Hollies (2009). Protocols for Slotted Liner Design for Optimum SAGD Operation. *Journal of Canadian Petroleum Technology 48*(11), 21–26. SPE-130441-PA. http://dx.doi.org/10.2118/130441-PA.

Bland, W. F. and R. L. Davidson (1967). *Petroleum Processing Handbook*. New York: McGraw-Hill.

Brand, S. (2010). Results from Acid Stimulation in Lloydminster SAGD Applications. Paper SPE-126311-MS presented at the SPE International Symposium and Exhibition on Formation Damage Control, Lafayette, Louisiana, 10-12 February. http://dx.doi.org/10.2118/126311-MS.

Brill, J. P. and H. Mukherjee (1999). *Multiphase Flow in Wells*, Vol. 17. Richardson, Texas: Monograph Series, SPE.

Buckley, S. E. and M. C. Leverett (1942). Mechanism of Fluid Displacement in Sands. *Transactions of the AIME 146*(1), 107–116. http://dx.doi.org/10.2118/942107-G.

Butler, R. M. (1997). *Thermal Recovery of Oil and Bitumen*. Calgary, Alberta: GravDrain Inc.

Butler, R. M., G. S. McNab, and H. Y. Lo (1981). Theoretical Studies on the Gravity Drainage of Heavy Oil During In-Situ Steam Heating. *The Canadian Journal of Chemical Engineering 59*(4), 455–460. http://dx.doi.org/10.1002/cjce.5450590407.

Butler, R. M. and D. J. Stephens (1981). The Gravity Drainage of Steam-heated Heavy Oil to Parallel Horizontal Wells. *Journal of Canadian Petroleum Technology 20*(2), 90–96. PETSOC-81-02-07. http://dx.doi.org/10.2118/81-02-07.

Carlson, M. R. (2006). *Practical Reservoir Simulation - Using, Assessing, and Developing Results*. Tulsa, Oklahoma: PennWell.

Cassis, R., N. Fuller, L. G. Hepler, R. J. C. McLean, A. Skauge, N. S. Srinivasan, and H. Yan (1985). Specific Heat Capacities of Bitumens and Heavy Oils, Reservoir Minerals, Clays, Dehydrated Clays, Asphaltenes, and Cokes. *AOSTRA Journal of Research 1*(3), 163–173.

Cengel, Y. A. and J. M. Cimbala (2006). *Fluid Mechanics: Fundamentals and Applications* (1st ed.). New York: McGraw-Hill.

Cenovus (2014a). Christina Lake In-situ Oil Sands Scheme 8591 2013 Update. https://www.aer.ca/documents/oilsands/insitu-presentations/2014AthabascaCenovusChristinaSAGD8591.pdf (downloaded 7 October 2014).

Cenovus (2014b). Foster Creek in-situ oilsands scheme (8623) update for 2013. https://www.aer.ca/documents/oilsands/insitu-presentations/2014AthabascaCenovusFosterCreekSAGD8623.pdf (downloaded 7 October 2014).

Cheung, T. and M. Scheck (2013). Novel Scale Remediation for Steam Assisted Gravity Drainage (SAGD) Operations. Paper SPE-164048-MS presented at the SPE International Symposium on Oilfield Chemistry, The Woodlands, Texas, 8-10 April. http://dx.doi.org/10.2118/164048-MS.

Chow, L. and R. M. Butler (1996). Numerical Simulation of the Steam-assisted Gravity Drainage Process (SAGD). *Journal of Canadian Petroleum Technology 35*(6), 55–62. PETSOC-96-06-06. http://dx.doi.org/10.2118/96-06-06.

Chung, K. H. and R. M. Butler (1988). Geometrical effect of steam injection on the formation of emulsions in the steam-assisted gravity drainage process. *Journal of Canadian Petroleum Technology 27*(1), 36–42. PETSOC-88-01-02. http://dx.doi.org/10.2118/88-01-02.

Cokar, M., M. S. Kallos, and I. D. Gates (2013). A New Thermogeomechanical Theory for Gravity Drainage in Steam-Assisted Gravity Drainage. *SPE Journal 18*(4), 736–742. SPE-163136-PA. http://dx.doi.org/10.2118/163136-PA.

Computer Modelling Group Ltd. (2014). STARS User Guide. Version 2014.

Computer Modelling Group Ltd. (2015). STARS - Thermal & Advanced Processes Reservoir Simulator. http://www.cmgl.ca/software/stars2014 (accessed 14 September 2015).

Das, S. (2005). Improving the Performance of SAGD. Paper SPE-97921-MS presented at the SPE International Thermal Operations and Heavy Oil Symposium, Calgary, Alberta, 1-3 November. http://dx.doi.org/10.2118/97921-MS.

Devon (2013). 2013 Subsurface Performance Presentation - Jackfish SAGD Project. https://www.aer.ca/documents/oilsands/insitu-presentations/2013AthabascaDevonJackfishSAGD10097.pdf (downloaded 19 November 2014).

Duncan, G. J., R. M. Stahl, and P. E. Moseley (2014). Nodal Analysis for SAGD Production Wells with ESPs. Paper SPE-170054-MS presented at the SPE Heavy Oil Conference-Canada, Calgary, Alberta, 10-12 June. http://dx.doi.org/10.2118/170054-MS.

Duncan, G. J., S. A. Young, and P. E. Moseley (2015). Nodal Analysis for SAGD Production Wells with Gas Lift. Paper SPE-174521-MS presented at the SPE Canada Heavy Oil Technical Conference, Calgary, Alberta, 9-11 June. http://dx.doi.org/10.2118/174521-MS.

Edmunds, N. (2000). Investigation of SAGD Steam Trap Control in Two and Three Dimensions. *Journal of Canadian Petroleum Technology 39*(1), 30–40. PETSOC-00-01-02. http://dx.doi.org/10.2118/00-01-02.

Edmunds, N. R. and S. D. Gittins (1993). Effective Application of Steam Assisted Gravity Drainage of Bitumen to Long Horizontal Well Pairs.

Journal of Canadian Petroleum Technology *32*(6), 49–55. PETSOC-93-06-05. http://dx.doi.org/10.2118/93-06-05.

Farouq Ali, S. M. (1974). Steam Injection. In *Secondary and Tertiary Oil Recovery Processes*. Oklahoma City, Oklahoma: Interstate Oil Compact Commission.

Ferguson, F. R. S. and R. M. Butler (1988). Steam-assisted gravity drainage model incorporating energy recovery from a cooling steam chamber. *Journal of Canadian Petroleum Technology* *27*(5), 75–83. PETSOC-88-05-09. http://dx.doi.org/10.2118/88-05-09.

Gates, I. D. and C. Leskiw (2010). Impact of steam trap control on performance of steam-assisted gravity drainage. *Journal of Petroleum Science and Engineering* *75*(1-2), 215–222. http://dx.doi.org/10.1016/j.petrol.2010.11.014.

Ghesmat, K. and L. Zhao (2014). SAGD Wellbore Completion Optimization Using Scab Liner and Steam Splitter. Paper SPE-170076-MS presented at the SPE Heavy Oil Conference-Canada, Calgary, Alberta, 10-12 June. http://dx.doi.org/10.2118/170076-MS.

Gonzalez, L. E., P. Ficocelli, and T. Bostick (2012). Real Time Optimization of SAGD Wells. Paper SPE-157923-MS presented at the SPE Heavy Oil Conference Canada, Calgary, Alberta, 12-14 June. http://dx.doi.org/10.2118/157923-MS.

Good, W. K., C. Rezk, and B. D. Felty (1997). Possible Effects of Gas Caps on SAGD Performance. Technical Report, Alberta Energy, Calgary, Alberta (March 1997).

Gotawala, D. R. and I. D. Gates (2012). A Basis for Automated Control of Steam Trap Subcool in SAGD. *SPE Journal* *17*(3), 680–686. SPE-159170-PA. http://dx.doi.org/10.2118/159170-PA.

Ito, Y. and S. Suzuki (1999). Numerical Simulation of the SAGD Process in the Hangingstone Oil Sands Reservoir. *Journal of Canadian Petroleum Technology 38*(9), 27–35. PETSOC-99-09-02. http://dx.doi.org/10.2118/99-09-02.

JuneWarren-Nickle's Energy Group (2015). Alberta Oil Sands Industry Quarterly Update: Summer 2015. http://albertacanada.com/files/albertacanada/AOSID_QuarterlyUpdate_Summer2015.pdf (downloaded 6 September 2015).

Kaiser, T. M. V. and S. P. Taubner (2013). Method for Controlling Fluid Interface Level in Gravity Drainage Oil Recovery Processes with Crossflow. Canadian Patent Application 2835751.

Kisman, K. E. (2003). Artificial Lift - A Major Unresolved Issue for SAGD. *Journal of Canadian Petroleum Technology 42*(8), 39–45. PETSOC-03-08-02. http://dx.doi.org/10.2118/03-08-02.

Krupiczka, R. (1967). Analysis of Thermal Conductivity in Granular Materials. *International Chemical Engineering 7*, 122–144.

Kyanpour, M. and Z. Chen (2014). Design and Optimization of Orifice based Flow Control Devices in Steam Assisted Gravity Drainage: A Case Study. Paper SPE-171109-MS presented at the SPE Heavy and Extra Heavy Oil Conference - Latin America, Medellin, Colombia, 24-26 September. http://dx.doi.org/10.2118/171109-MS.

Lake, L. (1989). *Enhanced Oil Recovery*. Prentice-Hall.

Least, B., S. Greci, R. Huffer, R. V. Rajan, and H. Golbeck (2014). Steam Flow Tests for Comparing Performance of Nozzle, Tube, and Fluidic Diode Autonomous ICDs in SAGD Wells. Paper SPE-170083-MS presented

at the SPE Heavy Oil Conference-Canada, Calgary, Alberta, 10-12 June. http://dx.doi.org/10.2118/170083-MS.

Leverett, M. C. (1941). Capillary Behavior in Porous Solids. *Transactions of the AIME 142*(1), 152–169. http://dx.doi.org/10.2118/941152-G.

Leverett, M. C., W. B. Lewis, and M. E. True (1942). Dimensional-model Studies of Oil-field Behavior. *Transactions of the AIME 146*(1), 175–193. http://dx.doi.org/10.2118/942175-G.

McCormack, M. (2002). SAGD Injection Wells - What Your Prof Never Told You. *Journal of Canadian Petroleum Technology 41*(3), 17–23. PETSOC-02-03-DA. http://dx.doi.org/10.2118/02-03-DA.

Mukherjee, N. J., S. D. Gittins, N. R. Edmunds, and K. E. Kisman (1995). A Comparison of Field versus Forecast Performance for Phase B of the UTF SAGD Project in the Athabasca Oil Sands. Presented at the 6th UNITAR International Conference on Heavy Crude and Tar Sands, Houston, Texas, 12-17 February.

Muskat, M. (1937). *The Flow of Homogeneous Fluids through Porous Media* (1st ed.). New York: McGraw-Hill.

Nasr, T. N., D. H.-S. Law, H. Golbeck, and G. Korpany (2000). Counter-current Aspect of the SAGD Process. *Journal of Canadian Petroleum Technology 39*(1), 41–47. PETSOC-00-01-03. http://dx.doi.org/10.2118/00-01-03.

Nexen (2014). 2013 Performance Presentation (Subsurface) - Long Lake. https://www.aer.ca/documents/oilsands/insitu-presentations/2014AthabascaNexenLongLakeSAGD9485.pdf (downloaded 19 November 2014).

Nield, D. A. and A. Bejan (2013). *Convection in Porous Media* (4th ed.). New York: Springer.

Noroozi, M., M. Melo, R. P. Singbeil, and B. Neil (2014). Investigation of Orifice Type Flow-Control Device Properties on the SAGD Process Using Coupled Wellbore Reservoir Modeling. Paper SPE-171131-MS presented at the SPE Heavy and Extra Heavy Oil Conference - Latin America, Medellin, Colombia, 24-26 September. http://dx.doi.org/10.2118/171131-MS.

Ong, T. S. and R. M. Butler (1990). Wellbore flow resistance in steam-assisted gravity drainage. *Journal of Canadian Petroleum Technology 29*(6), 49–55. PETSOC-90-06-04. http://dx.doi.org/10.2118/90-06-04.

Parappilly, R. and L. Zhao (2009). SAGD with a Longer Wellbore. *Journal of Canadian Petroleum Technology 48*(6), 71–77. PETSOC-09-06-71. http://dx.doi.org/10.2118/09-06-71.

Peaceman, D. W. (1983). Interpretation of Well-Block Pressures in Numerical Reservoir Simulation With Nonsquare Grid Blocks and Anisotropic Permeability. *Society of Petroleum Engineers Journal 23*(3), 531–543. SPE-10528-PA. http://dx.doi.org/10.2118/10528-PA.

Reis, J. C. (1992). A steam-assisted gravity drainage model for tar sands: linear geometry. *Journal of Canadian Petroleum Technology 31*(10), 14–20. PETSOC-92-10-01. http://dx.doi.org/10.2118/92-10-01.

Riel, A., R. C. Burton, G. P. Vachon, T. J. Wheeler, and M. Heidari (2014). An Innovative Modeling Approach to Unveil Flow Control Devices' Potential in SAGD Application. Paper SPE-170045-MS presented

at the SPE Heavy Oil Conference-Canada, Calgary, Alberta, 10-12 June. http://dx.doi.org/10.2118/170045-MS.

Shad, S. and M. M. Yazdi (2014). Wellbore modeling and design of Nozzle-Based Inflow Control Device (ICD) for SAGD wells. Paper SPE-170145-MS presented at the SPE Heavy Oil Conference-Canada, Calgary, Alberta, 10-12 June. http://dx.doi.org/10.2118/170145-MS.

Sharma, J. and I. D. Gates (2010). Multiphase Flow at the Edge of a Steam Chamber. *The Canadian Journal of Chemical Engineering 88*(3), 312–321. http://dx.doi.org/10.1002/cjce.20280.

Shen, C. (2013). SAGD for Heavy Oil Recovery. In *Enhanced Oil Recovery - Field Case Studies*. Waltham, Massachusetts: Elsevier.

Shin, H., T. Hwang, and B. Chon (2012). Optimal Grid System Design for SAGD Simulation. Paper SPE-157900-MS presented at the SPE Heavy Oil Conference Canada, Calgary, Alberta, 12-14 June. http://dx.doi.org/10.2118/157900-MS.

Singhal, A. K., Y. Ito, and M. Kasraie (1998). Screening and Design Criteria for Steam Assisted Gravity Drainage (SAGD) Projects. Paper SPE-50410-MS presented at the SPE International Conference on Horizontal Well Technology, Calgary, Alberta, 1-4 November. http://dx.doi.org/10.2118/50410-MS.

Smith, D., T. Handfield, and T. Kaiser (2014). SAGD Producer Wellbore Optimization - Concept to Completion. Presented at the 2014 World Heavy Oil Congress, New Orleans, Louisiana, 5-7 March.

Somerton, W. H., J. A. Keese, and S. L. Chu (1974). Thermal Behavior of

Unconsolidated Oil Sands. *Society of Petroleum Engineers Journal 14*(5), 513–521. SPE-4506-PA. http://dx.doi.org/10.2118/4506-PA.

Somiari, A.-B., R. Jobling, E. Pederson, and A. Cao (2014). Quantifying the Impact of Flow Control Devices in SAGD Applications in the Surmont Area Through Numerical Analysis. Paper SPE-170112-MS presented at the SPE Heavy Oil Conference-Canada, Calgary, Alberta, 10-12 June. http://dx.doi.org/10.2118/170112-MS.

Stahl, R. M., J. D. Smith, S. Hobbs, and C. M. Clarke (2014). Application of Intelligent Well Technology to a SAGD Producer: Firebag Field Trial. Paper SPE-170153-MS presented at the SPE Heavy Oil Conference-Canada, Calgary, Alberta, 10-12 June. http://dx.doi.org/10.2118/170153-MS.

Stalder, J. L. (2013). Test of SAGD Flow-Distribution-Control Liner System in the Surmont Field, Alberta, Canada. *Journal of Canadian Petroleum Technology 52*(2), 95–100. SPE-153706-PA. http://dx.doi.org/10.2118/153706-PA.

Suncor (2009). Suncor Firebag 2009 ERCB Performance Presentation. https://www.aer.ca/documents/oilsands/insitu-presentations/2009AthabascaSuncorFirebag8870.pdf (downloaded 24 October 2014).

Suncor (2014). Suncor Firebag 2014 AER Performance Presentation. https://www.aer.ca/documents/oilsands/insitu-presentations/2014AthabascaSuncorFirebagSAGD8870.pdf (downloaded 7 October 2014).

Tan, T. B., E. Butterworth, and P. Yang (2002). Application of a Thermal Simulator with Fully Coupled Discretized Wellbore Simulation to SAGD. *Journal of Canadian Petroleum Technology 41*(1), 25–30. PETSOC-02-01-01. http://dx.doi.org/10.2118/02-01-01.

Thorne, T. and L. Zhao (2009). The Impact of Pressure Drop on SAGD Process Performance. *Journal of Canadian Petroleum Technology 48*(9), 41–46. PETSOC-09-09-41. http://dx.doi.org/10.2118/09-09-41.

Vachon, G. P., W. Klaczek, P. J. Erickson, D. C. Langer, D. Booy, and A. Baugh (2015). Use of Flow Control Devices (FCDs) to Enforce Conformance in Steam Assisted Gravity Drainage (SAGD) Completions. Paper SPE-174416-MS presented at the SPE Canada Heavy Oil Technical Conference, Calgary, Alberta, 9-11 June. http://dx.doi.org/10.2118/174416-MS.

Vander Valk, P. A. and P. Yang (2007). Investigation of Key Parameters in SAGD Wellbore Design and Operation. *Journal of Canadian Petroleum Technology 46*(6), 49–56. PETSOC-07-06-02. http://dx.doi.org/10.2118/07-06-02.

Vinsome, P. K. W. and J. Westerveld (1980). A Simple Method For Predicting Cap And Base Rock Heat Losses In Thermal Reservoir Simulators. *Journal of Canadian Petroleum Technology 19*(3), 87–90. PETSOC-80-03-04. http://dx.doi.org/10.2118/80-03-04.

Walls, E., C. Palmgren, and K. Kisman (2003). Residual Oil Saturation Inside the Steam Chamber During SAGD. *Journal of Canadian Petroleum Technology 42*(1), 39–47. PETSOC-03-01-03. http://dx.doi.org/10.2118/03-01-03.

Yang, C., C. Card, and L. Nghiem (2009). Economic Optimization and Uncertainty Assessment of Commercial SAGD Operations. *Journal of Canadian Petroleum Technology 48*(9), 33–40. PETSOC-09-09-33. http://dx.doi.org/10.2118/09-09-33.

Yuan, J. and D. Nugent (2013). Subcool, Fluid Productivity, and Liquid Level Above a SAGD Producer. *Journal of Canadian Petroleum Technology 52*(5), 360–367. SPE-157899-PA. http://dx.doi.org/10.2118/157899-PA.

Yuan, J.-Y., T. Nasr, and D. H.-S. Law (2003). Impacts of Initial Gas-to-Oil Ratio (GOR) on SAGD Operations. *Journal of Canadian Petroleum Technology 42*(1), 48–52. PETSOC-03-01-04. http://dx.doi.org/10.2118/03-01-04.

Zhao, L., D. B. Anderson, and C. O'Rourke (2007). Understanding SAGD Producer Wellbore/Reservoir Damage Using Numerical Simulation. *Journal of Canadian Petroleum Technology 46*(1), 50–55. PETSOC-07-01-06. http://dx.doi.org/10.2118/07-01-06.

Zhao, L., D. H.-S. Law, and R. Coates (2003). Numerical Study and Economic Evaluation of SAGD Wind-Down Methods. *Journal of Canadian Petroleum Technology 42*(1), 53–57. PETSOC-03-01-05. http://dx.doi.org/10.2118/03-01-05.

Appendix A

Supplemental Simulation Results

A.1 Detailed Results for Case 2

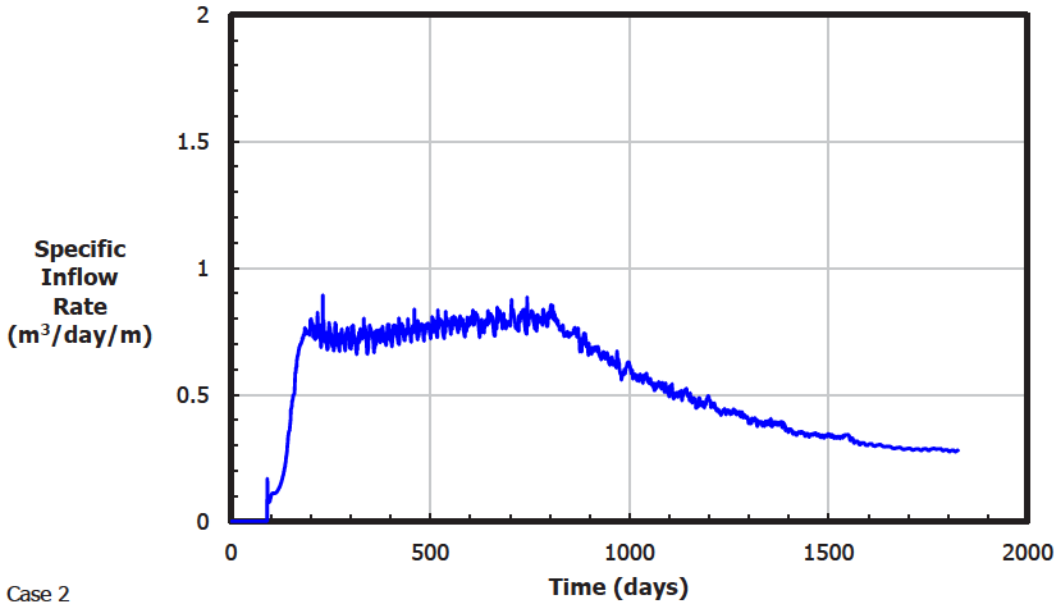

Figure A.1: Specific inflow rate for Case 2 baseline

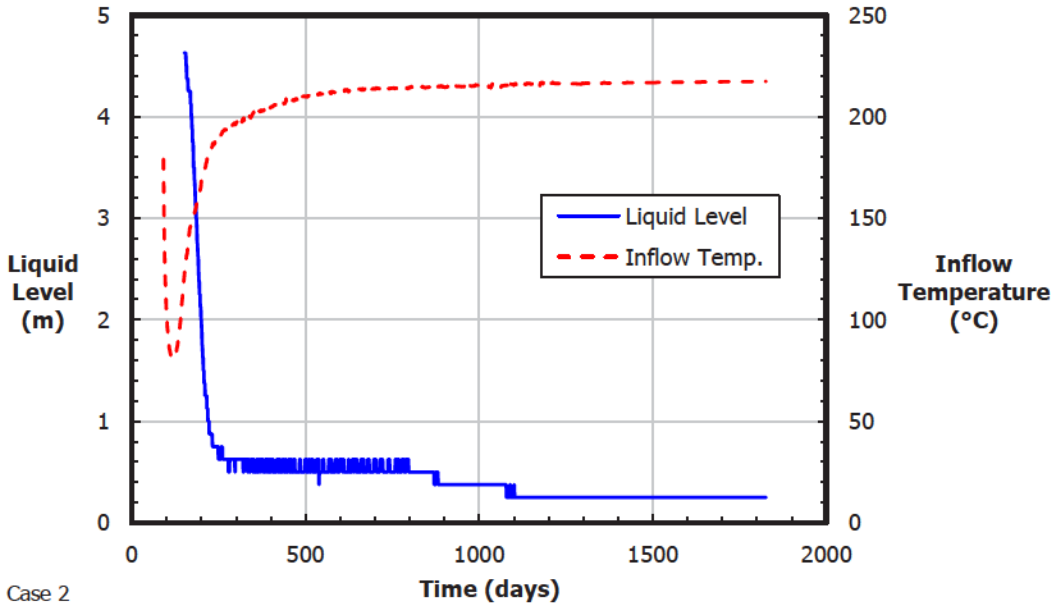

Figure A.2: Liquid level and inflow temperature for Case 2 baseline

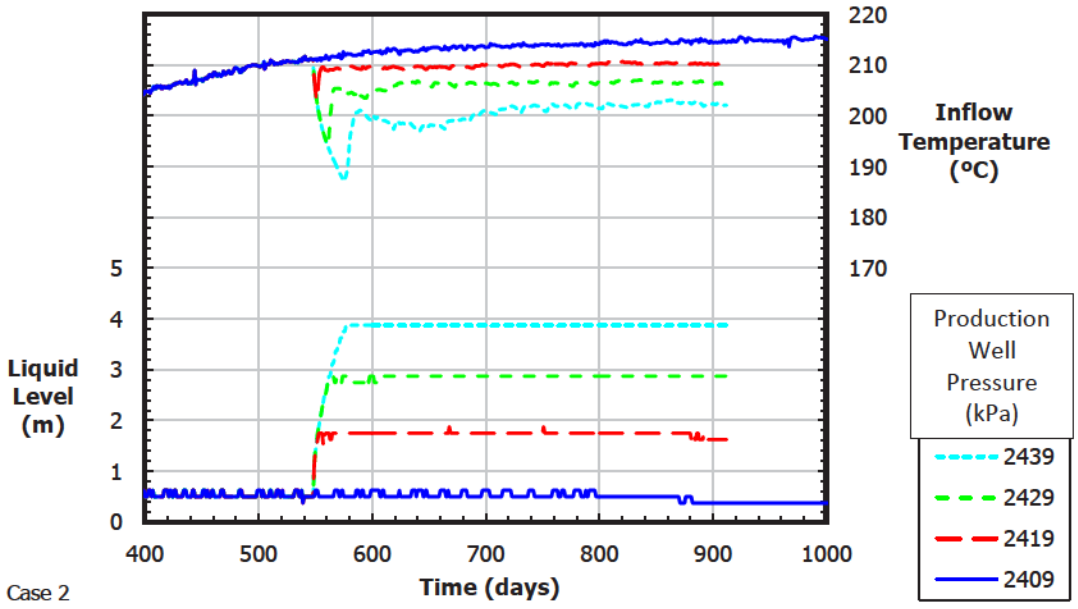

Figure A.3: Effect of well pressure on liquid level and inflow temperature for Case 2

A.2 Detailed Results for Case 3

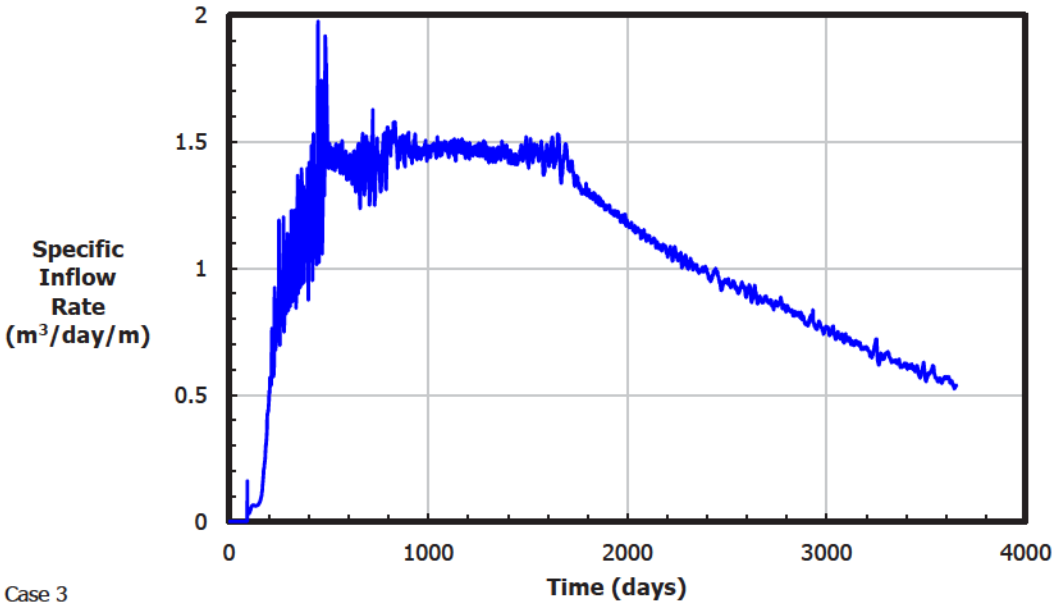

Figure A.4: Specific inflow rate for Case 3 baseline

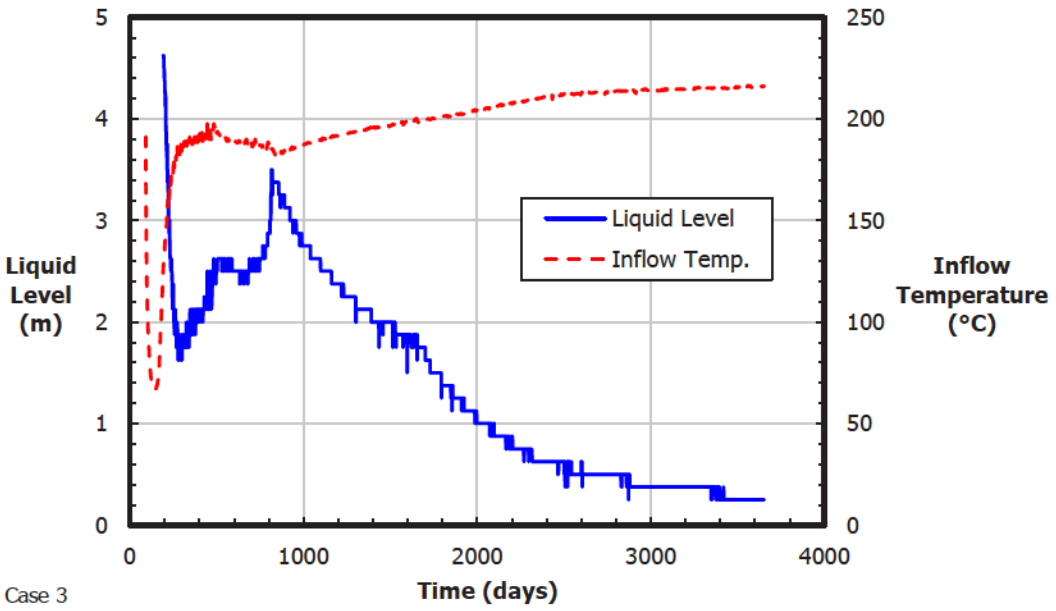

Figure A.5: Liquid level and inflow temperature for Case 3 baseline

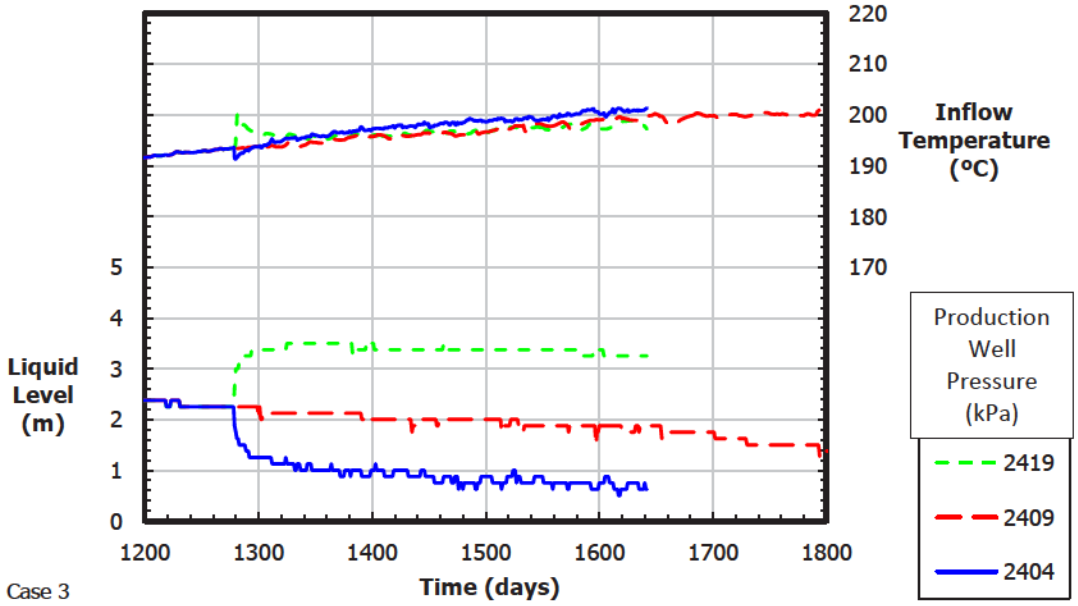

Figure A.6: Effect of well pressure on liquid level and inflow temperature for Case 3

A.3 Detailed Results for Case 4

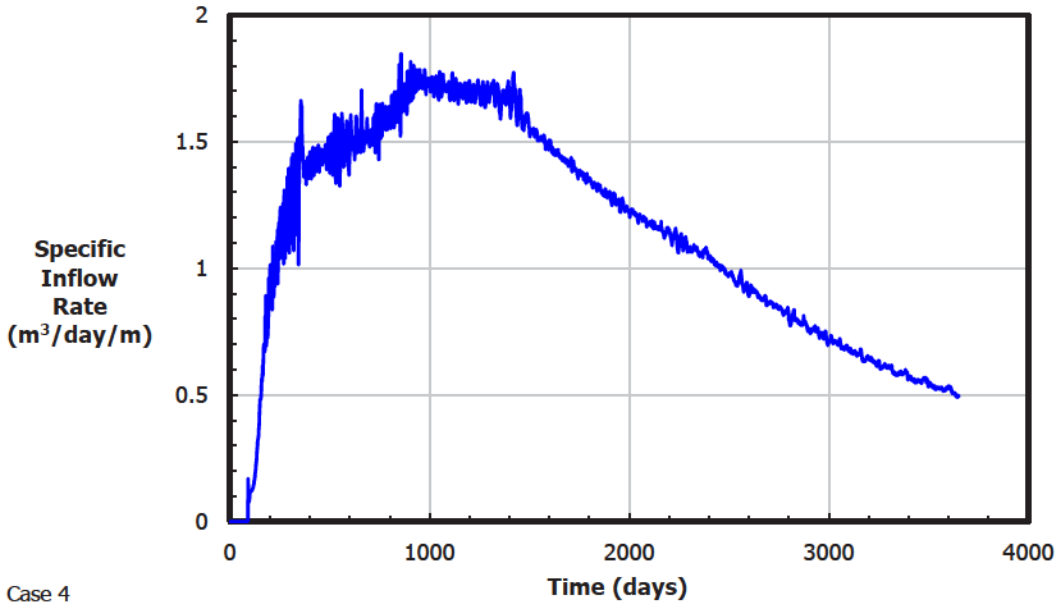

Figure A.7: Specific inflow rate for Case 4 baseline

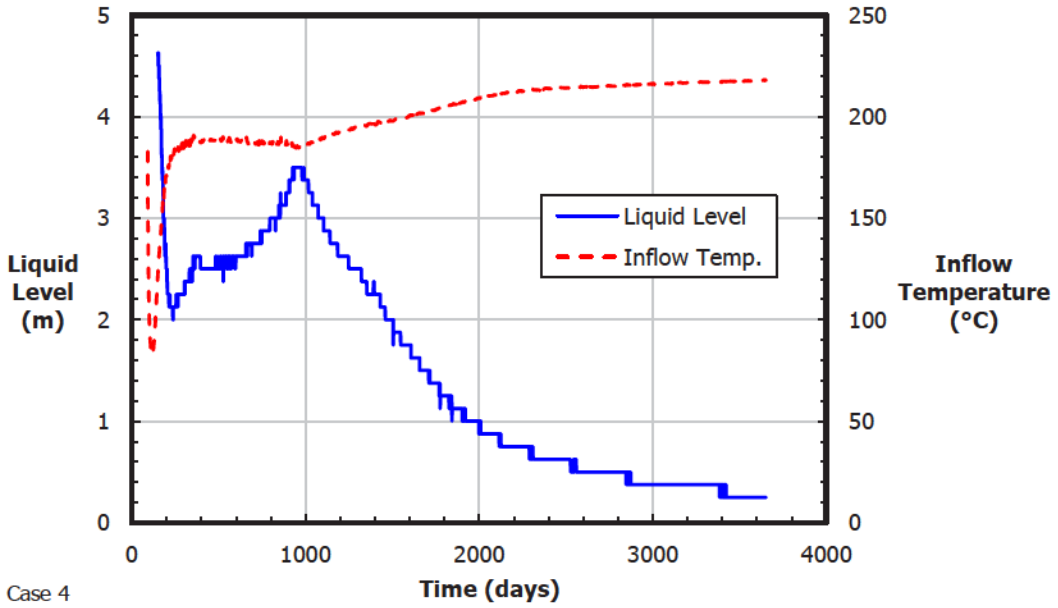

Figure A.8: Liquid level and inflow temperature for Case 4 baseline

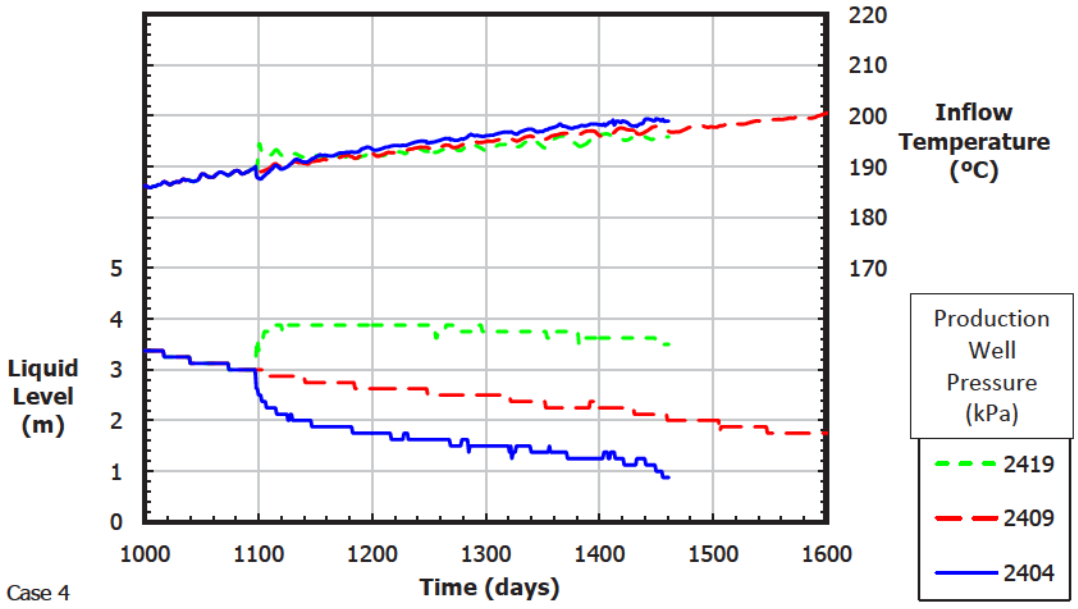

Figure A.9: Effect of well pressure on liquid level and inflow temperature for Case 4

A.4 Detailed Results for Case 11

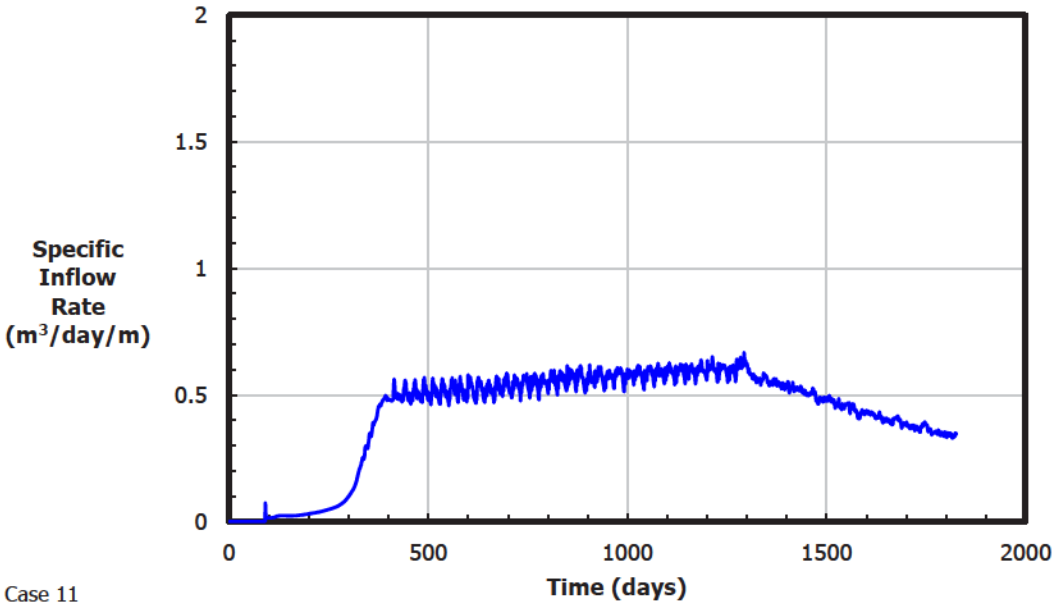

Figure A.10: Specific inflow rate for Case 11 baseline

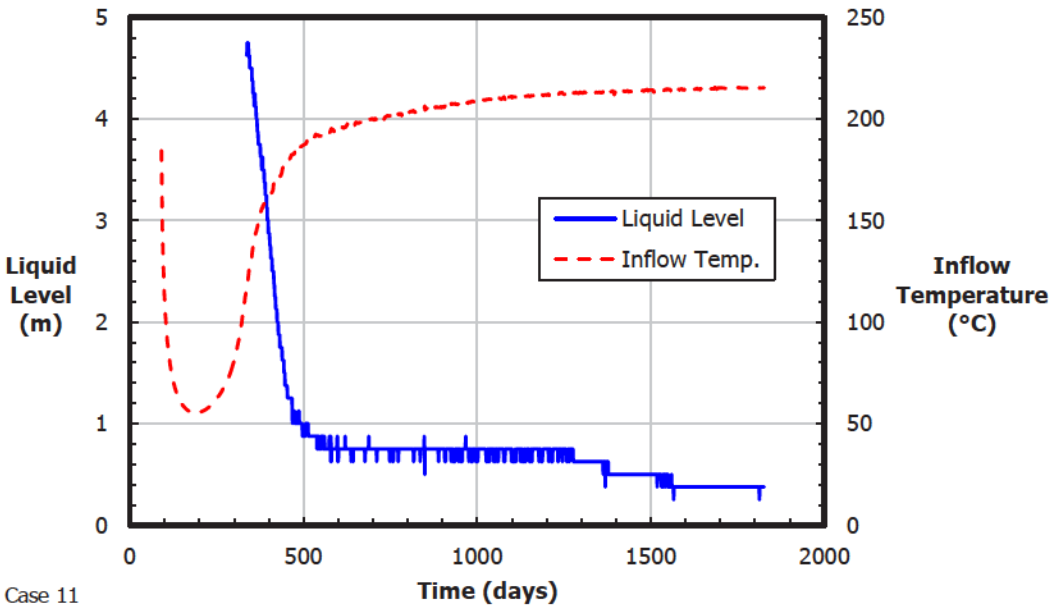

Figure A.11: Liquid level and inflow temperature for Case 11 baseline

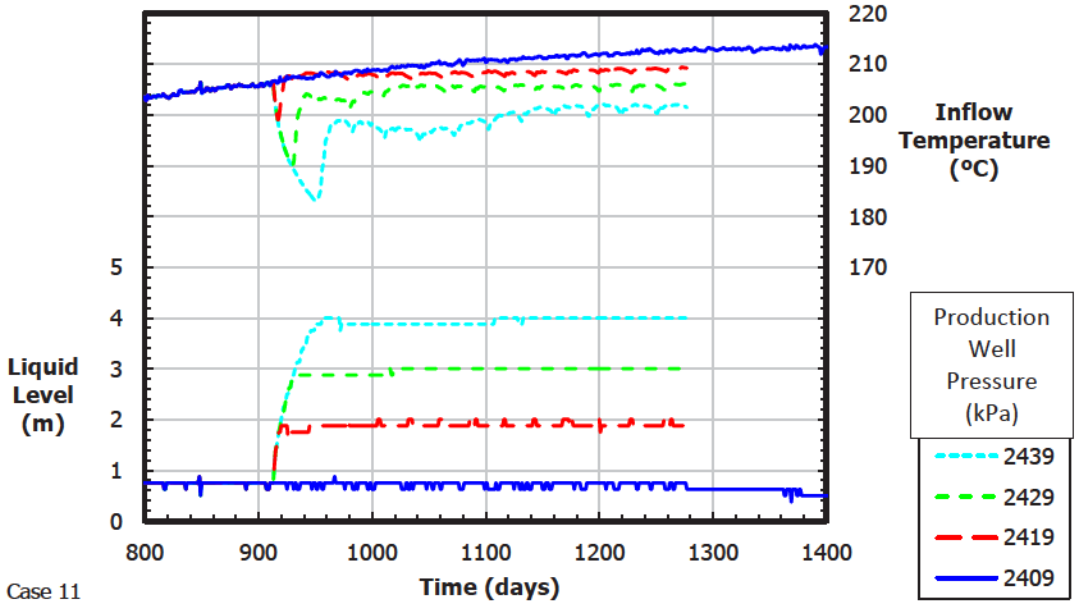

Figure A.12: Effect of well pressure on liquid level and inflow temp. for Case 11

A.5 Detailed Results for Case 12

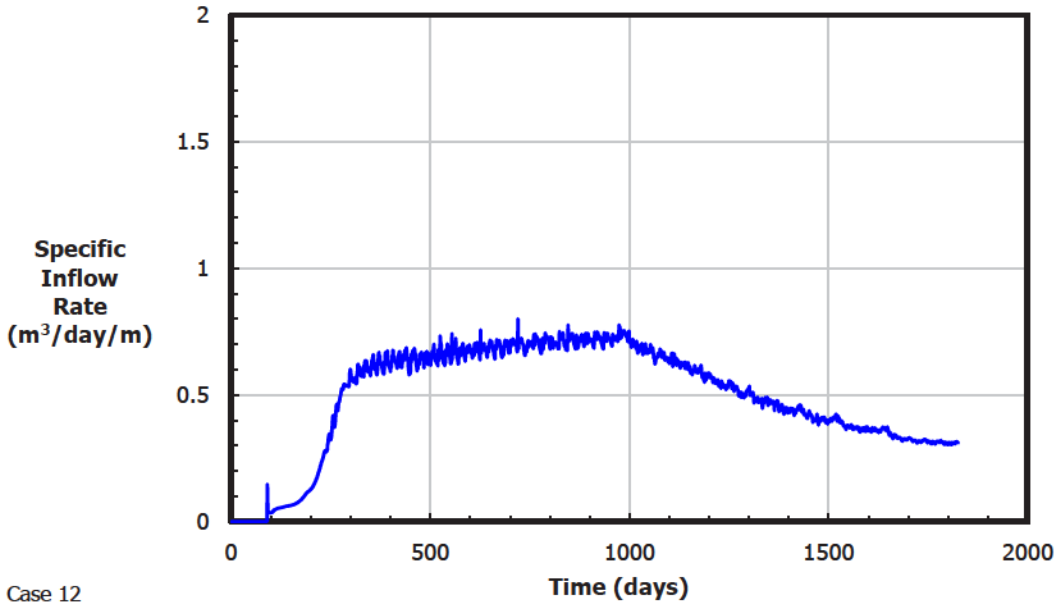

Figure A.13: Specific inflow rate for Case 12 baseline

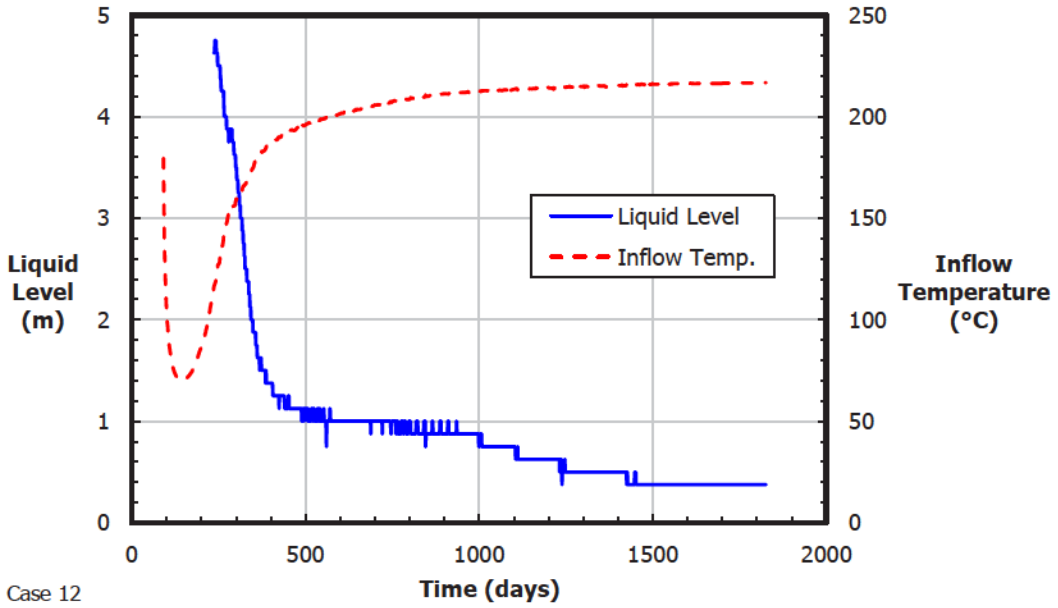

Figure A.14: Liquid level and inflow temperature for Case 12 baseline

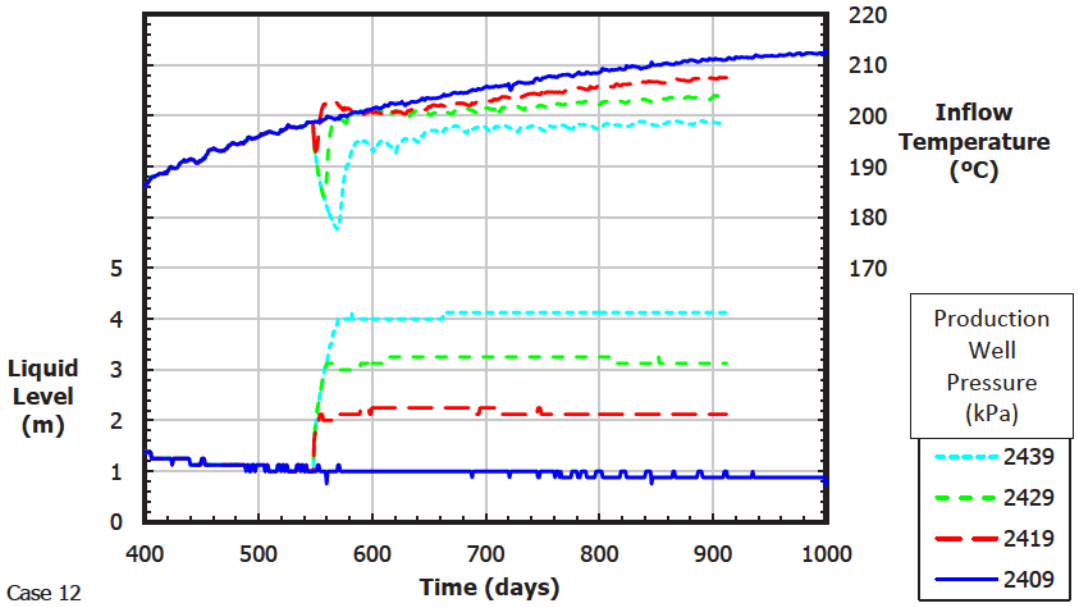

Figure A.15: Effect of well pressure on liquid level and inflow temp. for Case 12

A.6 Detailed Results for Case 13

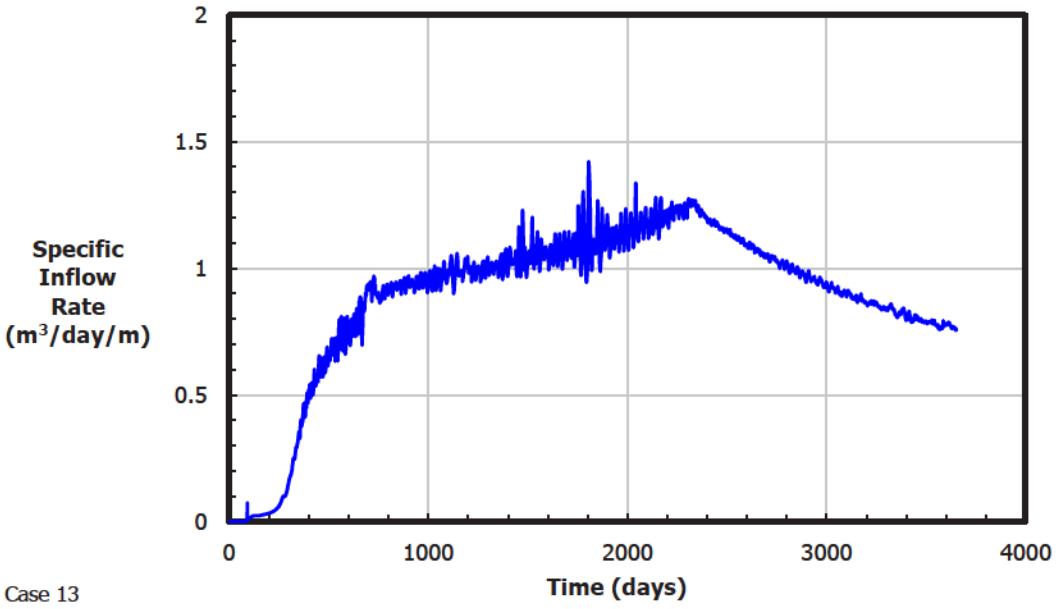

Figure A.16: Specific inflow rate for Case 13 baseline

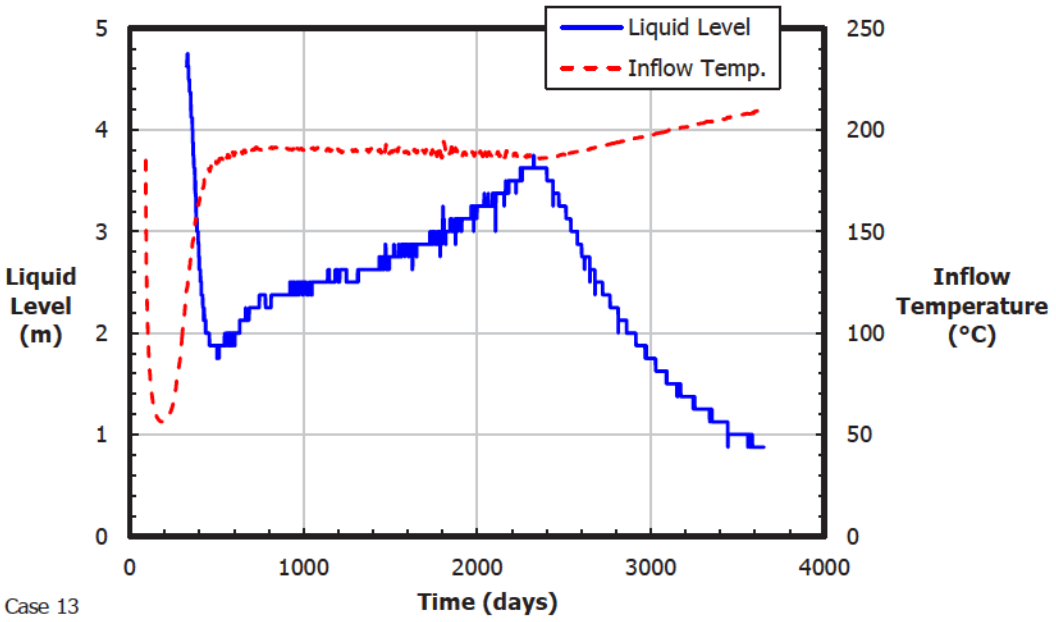

Figure A.17: Liquid level and inflow temperature for Case 13 baseline

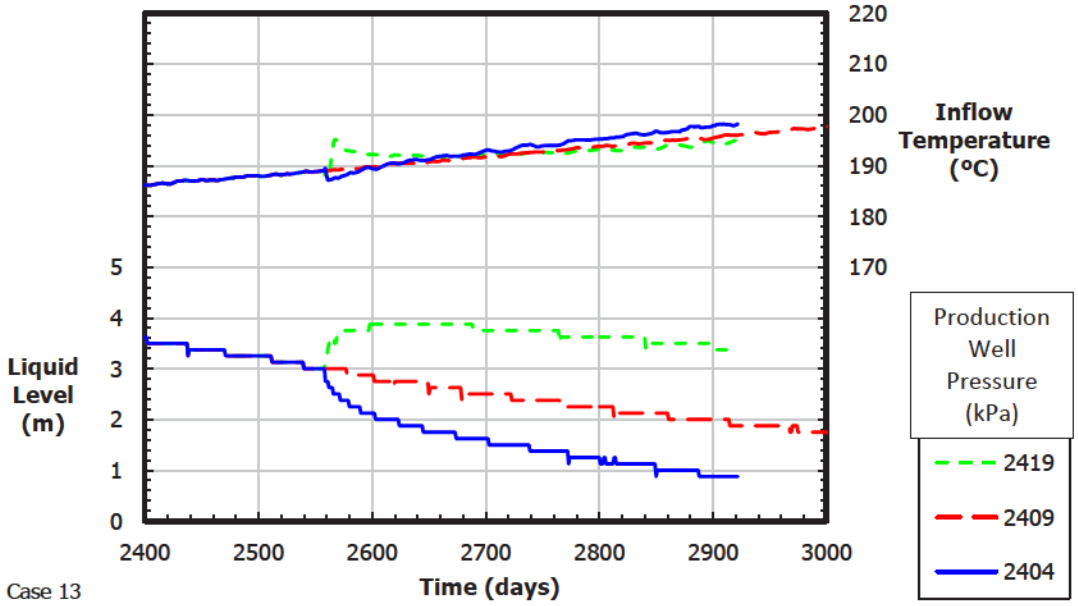

Figure A.18: Effect of well pressure on liquid level and inflow temp. for Case 13

A.7 Detailed Results for Case 14

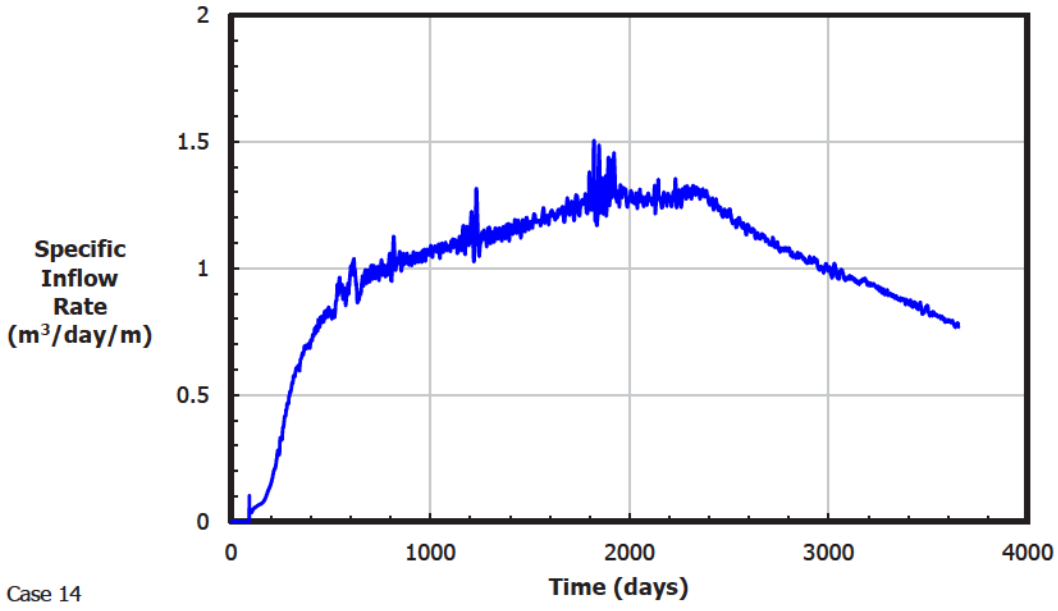

Figure A.19: Specific inflow rate for Case 14 baseline

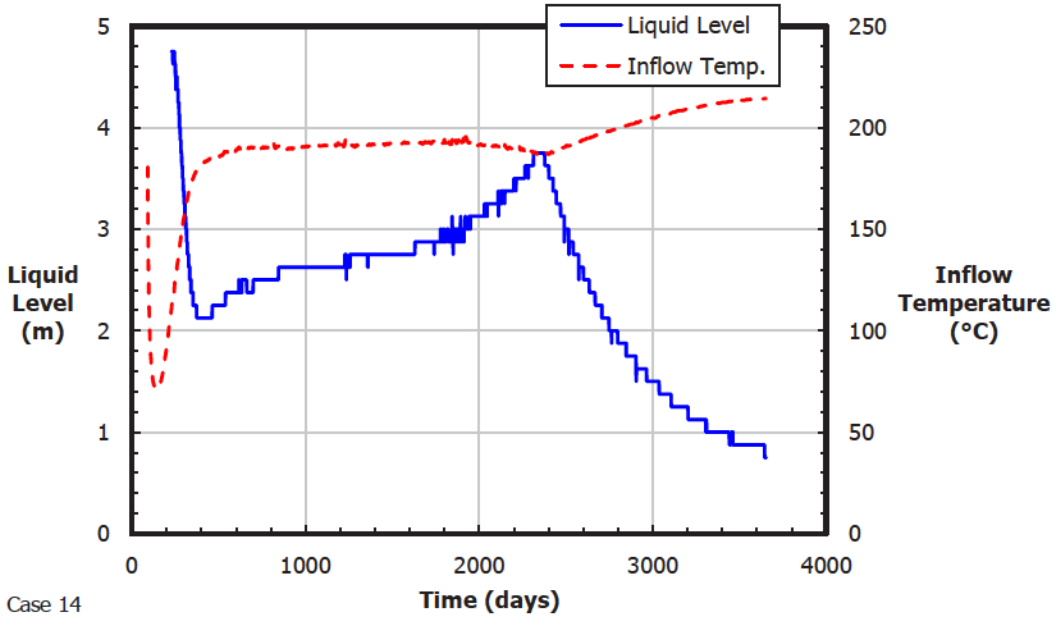

Figure A.20: Liquid level and inflow temperature for Case 14 baseline

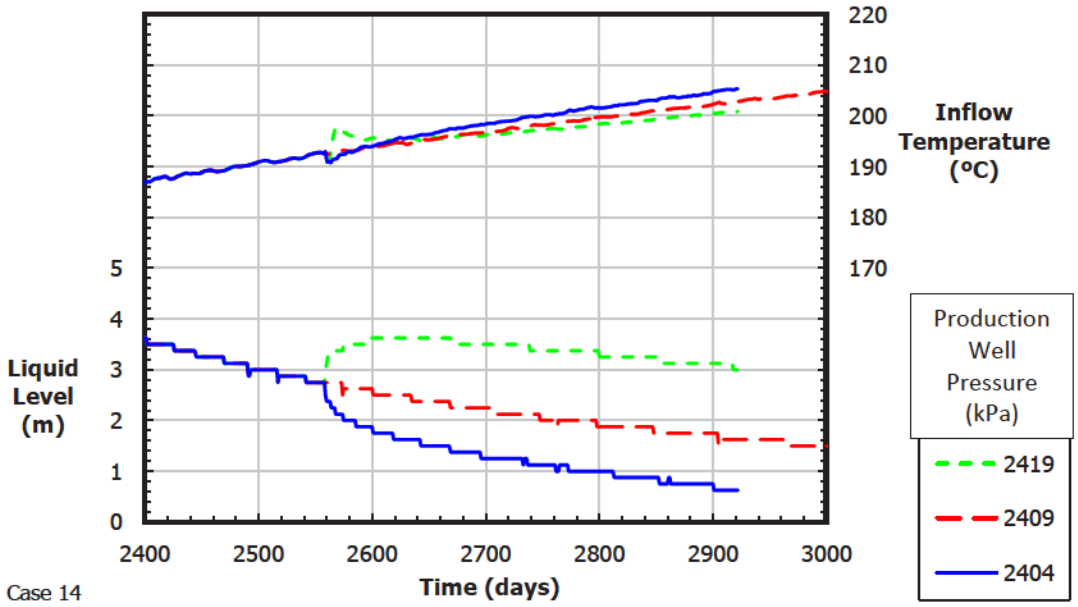

Figure A.21: Effect of well pressure on liquid level and inflow temp. for Case 14

A.8 Detailed Results for Case 23

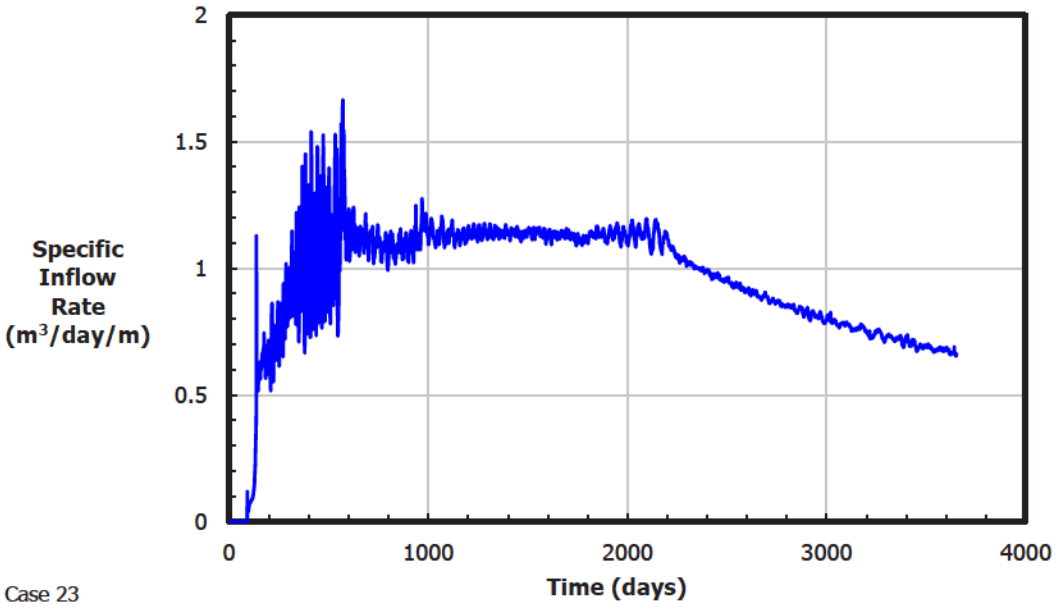

Figure A.22: Specific inflow rate for Case 23 baseline

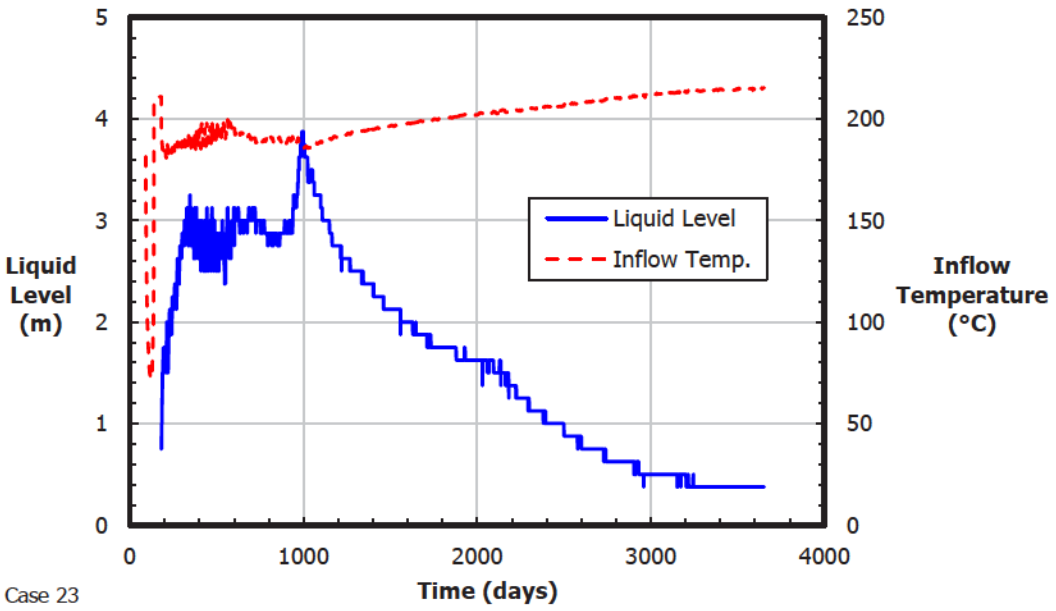

Figure A.23: Liquid level and inflow temperature for Case 23 baseline

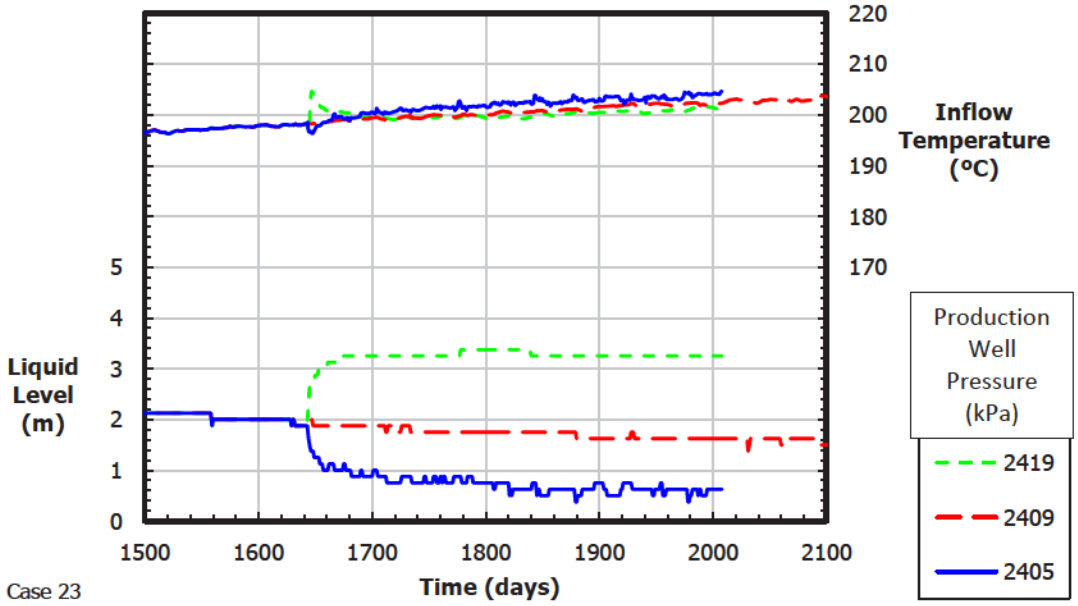

Figure A.24: Effect of well pressure on liquid level and inflow temp. for Case 23

A.9 Comparison of Liquid Levels from STARS and GIPR for Cases 2, 4, 12, 14, and 23

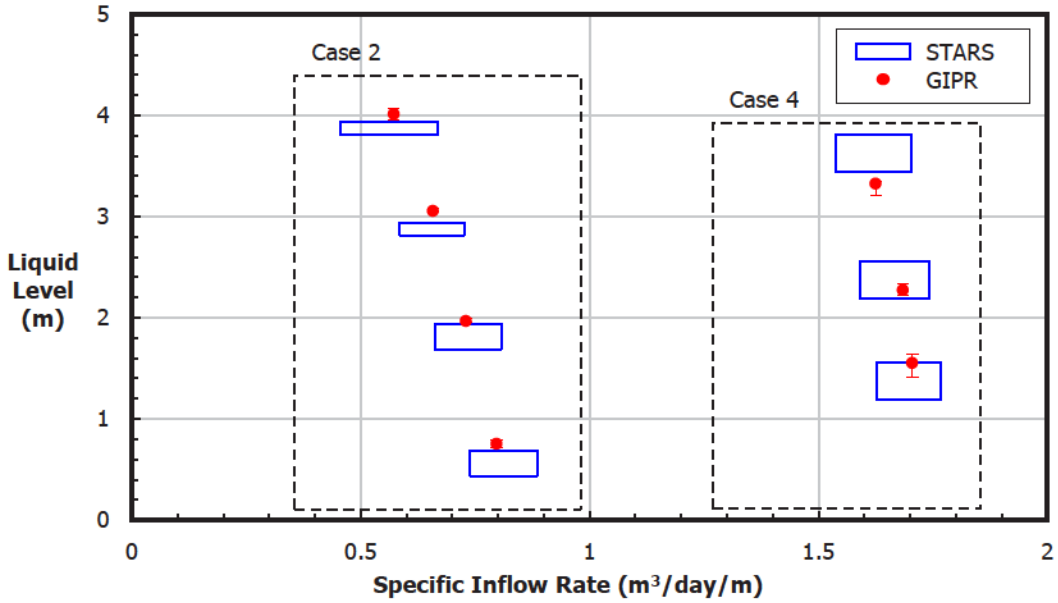

Figure A.25: Comparison of liquid levels from STARS and GIPR for Cases 2 and 4

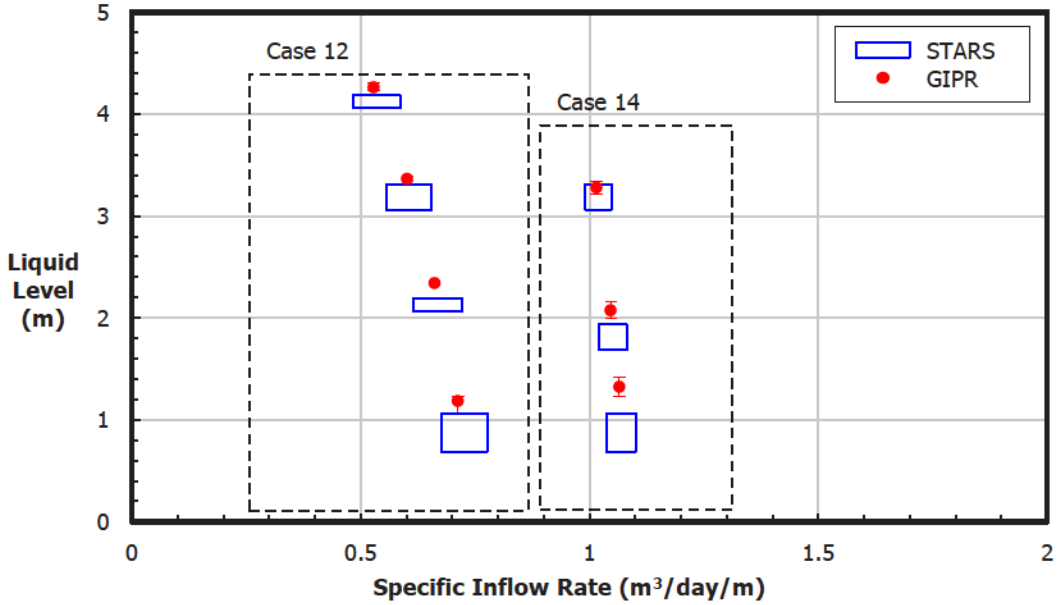

Figure A.26: Liquid levels from STARS and GIPR for Cases 12 and 14

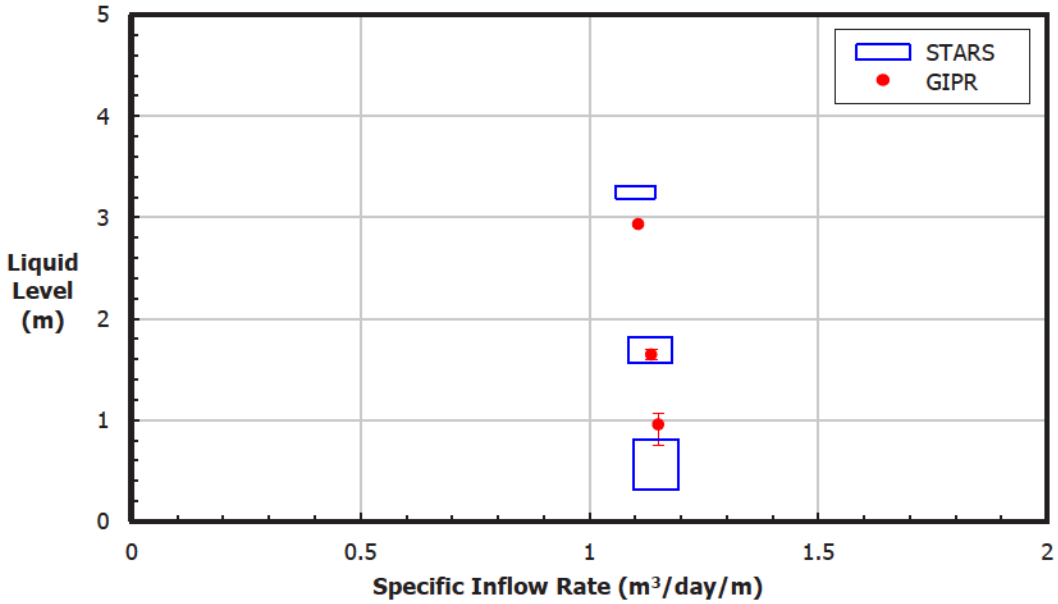

Figure A.27: Comparison of liquid levels from STARS and GIPR for Case 23

Appendix B

Supplemental Case Study Results

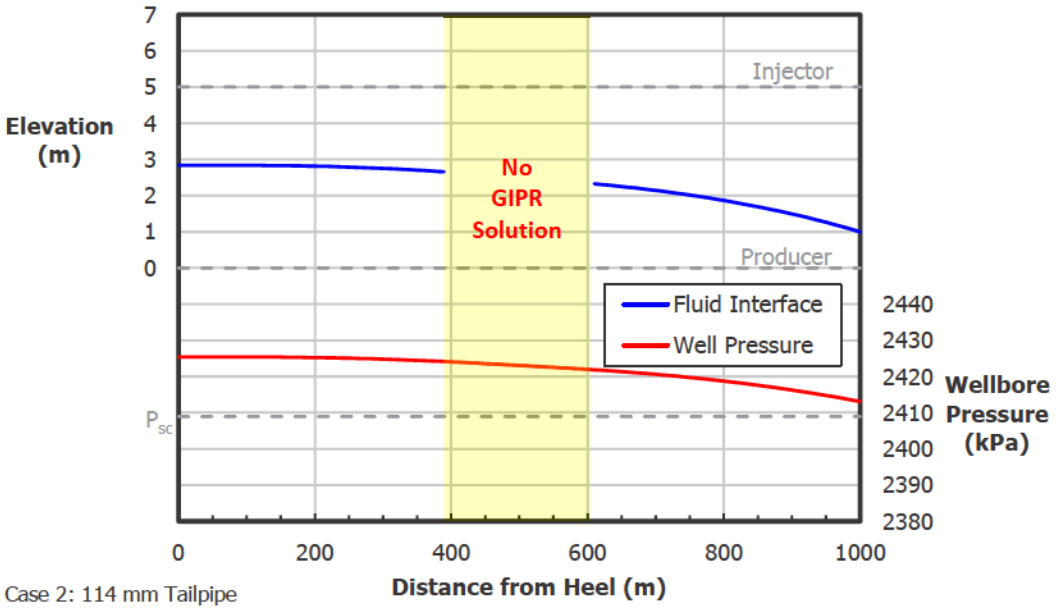

Figure B.1: Liquid level distribution with 114 mm tailpipe in Case Study 2

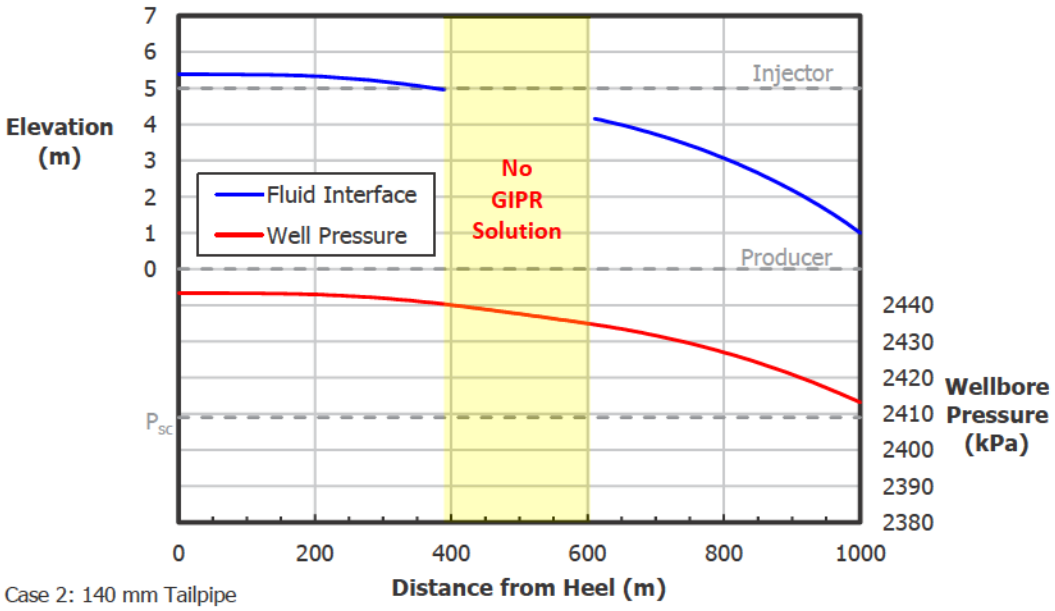

Figure B.2: Liquid level distribution with 140 mm tailpipe in Case Study 2

Appendix C

Reservoir Simulation Grid Design

STARS is a numerical simulator – it discretizes the reservoir into grid blocks to find an approximate solution to the governing equations. STARS results are sensitive to the number and distribution of grid blocks within the domain, and so optimization of the grid design is necessary to manage the discretization error. The grid design is particularly important for verification of the GIPR because the vertical grid block size governs the resolution of the liquid level output (e.g., a vertical grid block size of 1 m gives a resolution of $\pm$ 0.5 m in the liquid level output).

The academic license under which the STARS simulations were conducted limited the number of grid blocks to 10,000 and thus imposed a constraint on the grid design. The desired level of refinement could not be achieved with uniformly sized grid blocks without exceeding the 10,000 grid block limit, and so the domain was divided into two regions: (1) the far-field region, in which larger grid blocks were used to model the advance of the steam chamber, and (2) the near-wellbore region, in which smaller grid blocks were used to resolve the fluid interface. To obtain numerically consistent results, the size of the near-wellbore grid blocks could be reduced by no more than three to five times relative to the far-field grid blocks (Computer Modelling Group

Ltd. 2014), imposing a further constraint on the grid design.

The size of the far-field grid blocks was selected based on published simulation results. Researchers have found that grid blocks no larger than about 1 m horizontally by 1 m vertically are required to accurately model the SAGD process. This finding is supported by early efforts to model pilot wells at the Alberta Oil Sands Technology and Research Authority (AOSTRA) Underground Test Facility (Mukherjee et al. 1995) and subsequent sensitivity analyses (Carlson 2006; Shin et al. 2012). For this project, a far-field grid block size of 1 m horizontally by 0.5 m vertically was selected to reduce the contrast in the vertical grid block size at the boundary between the far-field and near-wellbore regions.

Few simulation results were found in the literature to guide refinement of the near-wellbore grid, and so the sensitivity of the results for Case 1 to the near-wellbore grid block size was assessed (see the case matrix in Section 4.2.3 for a summary of inputs). First, the simulation was run without near-wellbore grid refinement, and then the near-wellbore grid block size was reduced to half and one quarter of the far-field grid block size. Figures C.1 and C.2 show the sensitivity of the inflow rate, liquid level, and inflow temperature to the near-wellbore grid block size. Reducing the vertical grid block size from 0.5 m to 0.25 m has a noticeable effect on the simulation results; however, subsequent refinement to a vertical grid block size of 0.125 m has a much smaller effect. The magnitude of the fluctuations in the inflow rate appears insensitive to the near-wellbore grid block size. On the other hand, grid refinement reveals fluctuations in the liquid level that are masked with the coarsest grid.

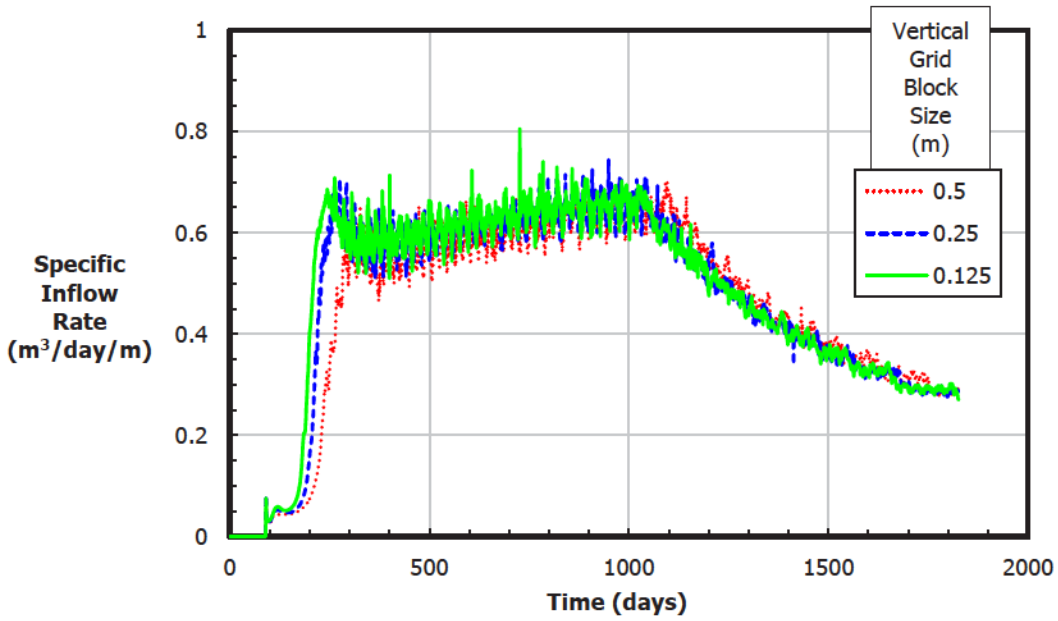

Figure C.1: Effect of near-wellbore grid block size on inflow rate for Case 1

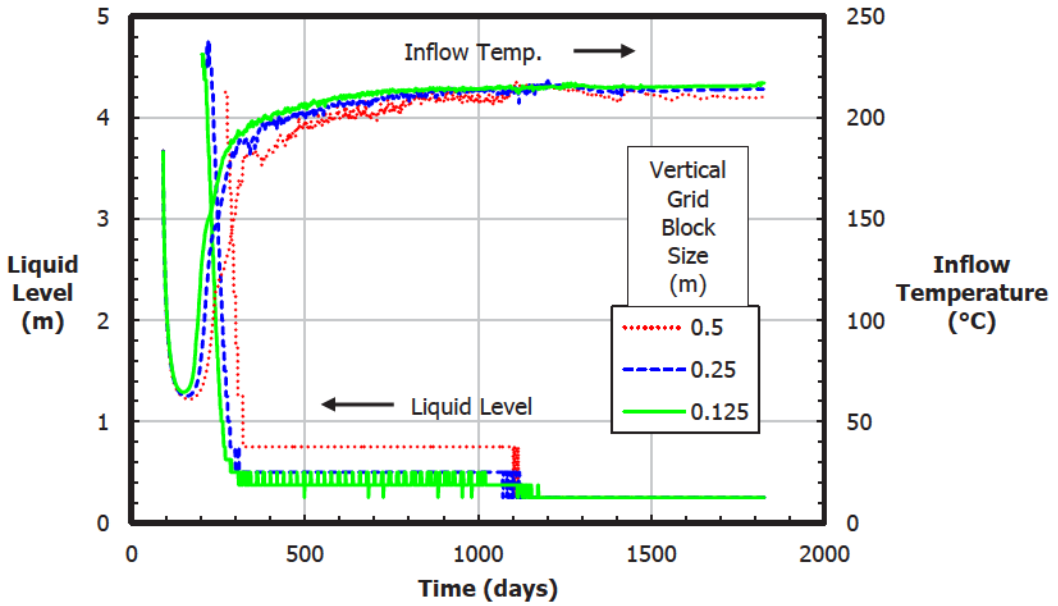

Figure C.2: Effect of grid size on liquid level and inflow temperature for Case 1

To investigate the fluctuations in the liquid level output, the stable operating windows for the three grids were compared at two production well pressures – 2409 kPa, corresponding to the baseline simulation, and 2429 kPa (see Section 4.2.4 for an explanation of how the operating windows are defined). The operating windows are presented in Figure C.3. As the near-wellbore grid is refined, the uncertainty in the stable liquid level becomes dominated by fluctuations in the STARS output rather than the grid resolution. Consequently, vertical refinement of the near-wellbore grid block size beyond 0.125 m would not be expected to significantly reduce the uncertainty in the stable liquid level.

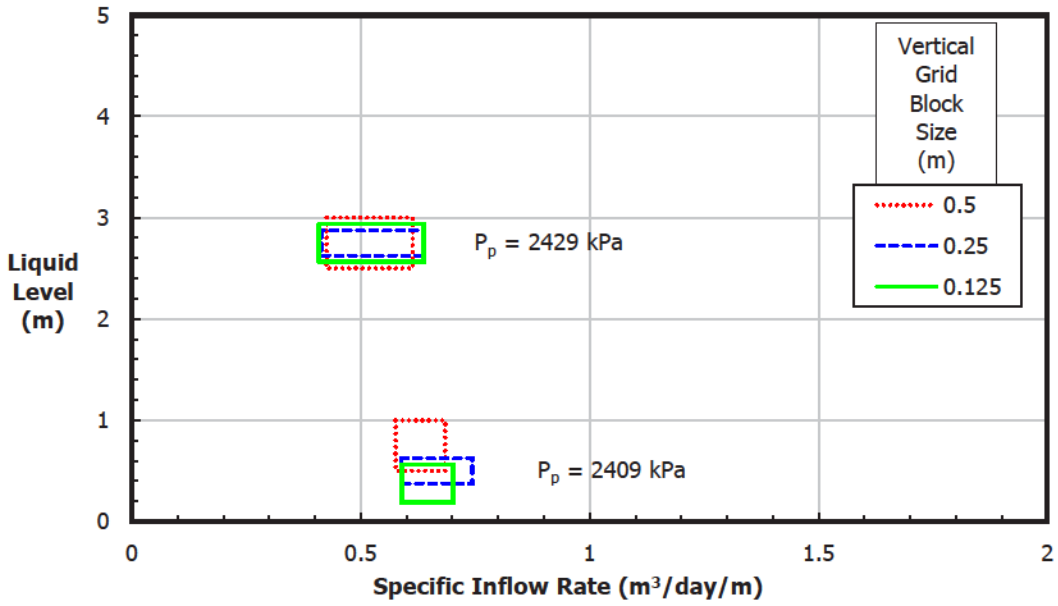

Figure C.3: Effect of near-wellbore grid block size on operating windows for Case 1

Based on the grid sensitivity analysis, a near-wellbore grid block size of 0.25 m horizontally by 0.125 m vertically was selected for this project. Pragmatically, further grid refinement was not feasible within the 10,000 grid block limit.

C.1 Time Step Sensitivity Study

STARS has an automatic time stepping routine, whereby the size of the time steps is governed by maximum allowable changes in the solution variables. To assess whether time discretization contributed to the fluctuations in the STARS output, the maximum allowable changes in the solution variables were reduced to half and one quarter of their default values, and Case 1 was rerun. Figure C.4 reveals that increasing the number of time steps has little effect on the magnitude of the fluctuations in the inflow rate.

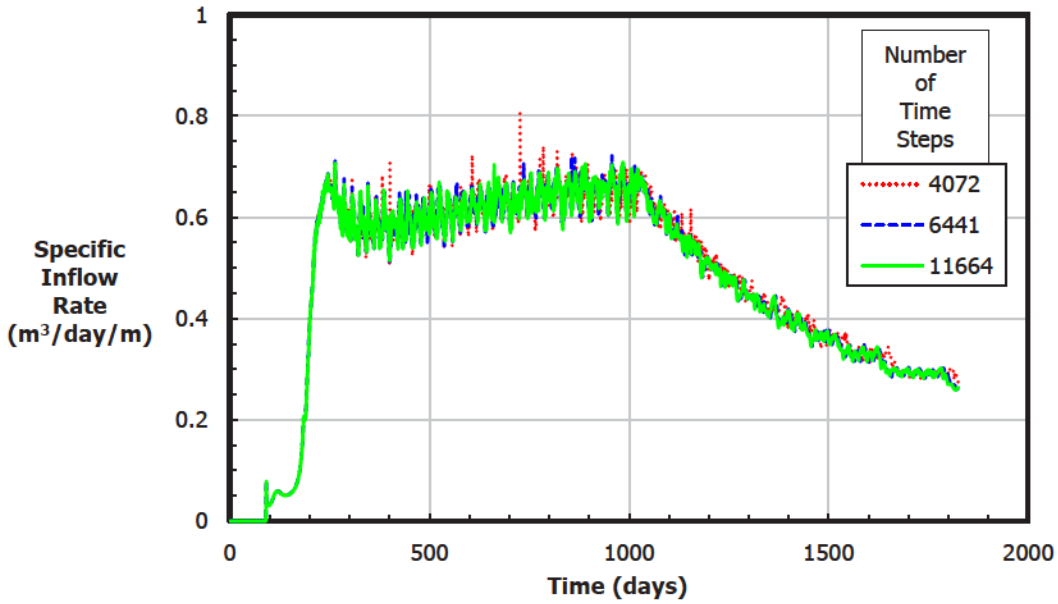

Figure C.4: Effect of time step size on inflow rate for Case 1